Isospin Dynamics and the Isospin Dependent EOS

By

Tianxiao Liu

A DISSERTATION

Submitted to
Michigan State University
in partial fulfillment of the requirements
for the Degree of

DOCTOR OF PHILOSOPHY

Department of Physics and Astronomy

2005

ABSTRACT

Isospin Dynamics and the Isospin Dependent EOS

By

Tianxiao Liu

Isotopic yields for light particles and intermediate mass fragments have been measured for ^{112}Sn+^{112}Sn, ^{112}Sn+^{124}Sn, ^{124}Sn+^{112}Sn and ^{124}Sn+^{124}Sn with the Large Area Silicon Strip Array (LASSA). LASSA consists of nine individual telescopes with each telescope comprised of two Si strip silicon detector layers backed by four CsI(Tl) crystals. LASSA provides high angular, energy and isotopic resolution over a large detection area and energy range. The total solid angle covered by LASSA is about 540msr with polar angle 7°-58° and an angular resolution of ±0.43°. The energy range covered is E/A = 2.4-140 MeV for protons and E/A = 4.8-335 MeV for ^{16}O.

Isotopic yields from central collisions were compared with predictions of stochastic mean field calculations. These calculations predict a sensitivity of the isotopic distributions to the density dependence of the asymmetry term of the nuclear equation of state. However, the secondary decay of the excited fragments modifies significantly the isotopic distributions produced by the stochastic mean field model. The predicted final isotope distributions after decay are narrower and more neutron-rich than the experimental data and the sensitivity of the predicted yields to the density dependence of the asymmetry term is reduced. The distributions calculated using the stiff asymmetry term are more neutron-rich and are closer to the measured values. However the less than satisfactory level of agreement between theory and experiment precludes definitive statements about the density dependence of the asymmetry term of the EOS.

Energy spectra and average energy of light particles and fragments from central collisions were obtained and compared with statistic models calculations. We found that neutron deficient isotopes are significantly more energetic than those of neutron rich isotopes of the same element. This trend is well beyond what can be expected for the bulk multi-fragmentation of an equilibrated system. It can be explained, however, if many of these fragments are evaporated from the surface of the system while it is expanding and cooling.

Measurements of particles and fragments from peripheral collisions were used to study the dynamics in nuclear reactions. Isoscaling analyses imply that the quasi-projectile and quasi-target in these collisions do not achieve isospin equilibrium, permitting an assessment of the isospin transport rates. We find that comparisons between isospin sensitive experimental and theoretical observables, using suitably chosen scaled ratios, permit investigation of the density dependence of the asymmetry term of the nuclear equation of state. This observable appears to be one of those promising ones for providing much needed constraints on the asymmetry at sub-saturation density.

ACKNOWLEDGEMENTS

First and foremost, I would like to express my most sincere thanks to my dissertation advisor, Dr. William G. Lynch. He is a unique combination of great intellects and genuine caring for those persons for whom he has some responsibility. I was very fortunate to be one of these people. To me, he is not only a world class advisor, but also a dear brother and an influential mentor. He is a source of endless inspiration even during the most stressful times. His guidance, support, vision and friendship will be a long-lasting influence in my professional and personal life.

I would also like to thank Dr. Pawel Danielewicz, Dr. Chien-Peng Yuan, Dr. Betty Tsang and Dr. Edward Brown for serving on my guidance committee. Special thanks go to Dr. Betty Tsang for her enthusiasm. She is an inexhaustible source of intellectual and creative energy. Her good sense in finding general physics laws to explain complicated experimental data was an excellent lesson to me. I am extremely impressed by her ability to get an intuitive feel of the most difficult ideas. Special thanks also go to Dr. A. Wagner, Dr. H. S. Xu, Dr. H. F. Xi, Dr. G. Verde and Dr. MJ van Goethem who helped me with software writing, experiment set-up and data analysis.

My work on my dissertation and the research benefited from the successful collaboration of the groups at Michigan State University (MSU), Indiana University (IU) and Washington University (WU). I would like to thank the MSU group of C. K. Gelbke, W. P. Tan, X. D. Liu, W. G. Lynch, M. B. Tsang, A. Vander Molen, G. Verde, A. Wagner, H. F. Xi, and H. S. Xu, the IU group of L. Beaulieu, B. Davin, Y. Larochelle, T. Lefort, R. T. De Souza, R. Yanez and V. E. Viola and the WU group of R. J. Charity and L. G. Sobotka.

A number of people have contributed to the work which culminates in this dissertation. Among them are: Drs. M. Colonna, M. Di toro, M. Zielinska-Pfabe, W. H.

Woolter, W. A. Friedman, S. R. Souza, R. Donangelo, L. J. Shi and P. Danielewicz. I gratefully acknowledge their assistance on model calculations.

This dissertation and research that it describes could not be accomplished had it not been for the excellent support of the staff at the National Superconducting Cyclotron Laboratory of Michigan State University. I owe my deepest thanks to John Yurkon of the detector lab, Len Morris of the design group, Jim Vincent of the electronics group, Andrew Vander Molen and Ron Fox of the computer group, who helped with data acquisition.

CONTENTS

LIST OF TABLES

LIST OF FIGURES

Chapter 1

Introduction

1.1 Background and Motivation

Heavy nucleus-nucleus collisions provide a unique way of exploring several interesting topics, among which are the nuclear liquid-gas phase transition and nuclear equation of state (EOS). The liquid-gas phase transition has been investigated for a long time. It bears some relevance to the phenomenon of multi-fragmentation but its detailed connection to that process is still open to questions.

The nuclear equation of state (EOS) describes the relation between pressure, density, temperature and isospin asymmetry for nuclear matter. Understanding EOS is very crucial in astrophysical contexts. For example, the EOS governs the dynamics of dense matter in supernovae [7]. It also influences strongly the internal structure, radii, maximum masses and moments of inertia of neutron stars [59]. In addition, the EOS influences the time scale for cooling of proto-neutron stars. In particular, the density dependence of the asymmetry term of the EOS can determine whether or not the direct Urca process can occur[57]. Finally, it is relevant to remember that the EOS affects significantly the binding energy and rms radii of neutron-rich nuclei [100] as well as the difference between neutron and proton radii in nuclei [17]. These

parameters may influence the formation of the heavy elements via the r-process.

Significant constraints have already been placed on the symmetric matter EOS at high densities [31]. However, the constraints on isospin-asymmetry term of the EOS, which describes the sensitivity of EOS to the difference between neutron and proton densities, is poor. Better knowledge of this term is essential to understand both the central density of neutron-rich isotopes [105] and the internal structure, radii and moment of inertia for neutron stars [81, 58].

Theoretical studies have shown that the EOS of asymmetric nuclear matter can be approximately expressed as [63]

$$E(\rho,\delta) = E(\rho,\delta=0) + S(\rho)\delta^2 \ , \tag{1.1}$$

where $\rho = \rho_n + \rho_p$ is baryon density, $\delta = (\rho_n - \rho_p)\rho_n + \rho_p)$ is the relative neutron excess, and $E(\rho,\delta=0)$ is the energy per particle in symmetric nuclear matter. The bulk symmetry energy is denoted by $S(\rho)$. Its value at normal density, $S_0 \equiv S(\rho_0)$, is known to be in the range of 27-36 MeV [46]. Different density dependences of $S(\rho)$ have been found, depending on the nuclear forces used in the calculation. One simple parameterization can be written as [85]

$$S(\rho) = (2^{2/3}-1)(\frac{3}{5}E_F^0)[u^{2/3} - F(u)] + S_0F(u) \ , \tag{1.2}$$

where E_F^0 is the Fermi energy and $u \equiv \rho/\rho_0$ is the reduced baryon density, and F(u) denotes the potential energy contribution. To understand the role the density dependence of $F(u)$ has on various quantities, it has been approximated by the following parameterizations:

$$\begin{aligned} F_1(u) &= \frac{2u^2}{1+u}, \\ F_2(u) &= u, \\ F_3(u) &= u^{1/2}, \end{aligned} \tag{1.3}$$

which provide a range of reasonable density dependencies[63].

The symmetry potential for neutrons and protons due to the interaction component of the symmetry energy can be obtained,

$$V_{asy}^{n(p)}(\rho,\delta) = e_a \frac{\partial(\rho F(u)\delta^2)}{\partial \rho_{n(p)}} \ , \tag{1.4}$$

where $e_a \equiv [S_0 - (2^{2/3}-1)(\frac{3}{5}E_F^0)]$ is the contribution of nuclear interactions to the bulk symmetry energy at normal nuclear matter density.

Fig. 1.1 shows the symmetry potential as a function of u, using two forms of $F(u)$, i.e. F_1 and F_3 and $S_0 = 30$MeV. The symmetry potential from F_2, which is not shown, always falls between those for symmetry potentials from F_1 and F_3.

From Fig. 1.1 we can see that the symmetry potential is quite sensitive to the form of $F(u)$, the neutron excess δ and the baryon density ρ. In collisions of neutron-rich nuclei at intermediate energies, both δ and ρ can be appreciable in a large space-time region where the isospin-dependent mean fields, which are opposite in sign for neutrons and protons, are strong. This will affect differently the reaction dynamics of neutrons and protons, leading to possible differences in their yields and energy spectra. This suggested that it is possible to extract information on the asymmetry term of the nuclear EOS in regions under laboratory controlled conditions. Although in heavy-ion collisions at intermediate energies we certainly cannot reach very high-density regions, we should be able to obtain information on the slope of the asymmetry term below the saturation density. Qualitatively different effects arise in central collisions, with bulk fragmentation, and peripheral collisions with neck fragmentation. In this way we hope to put some experimental constraints on the effective interactions used in astrophysical contexts [9].

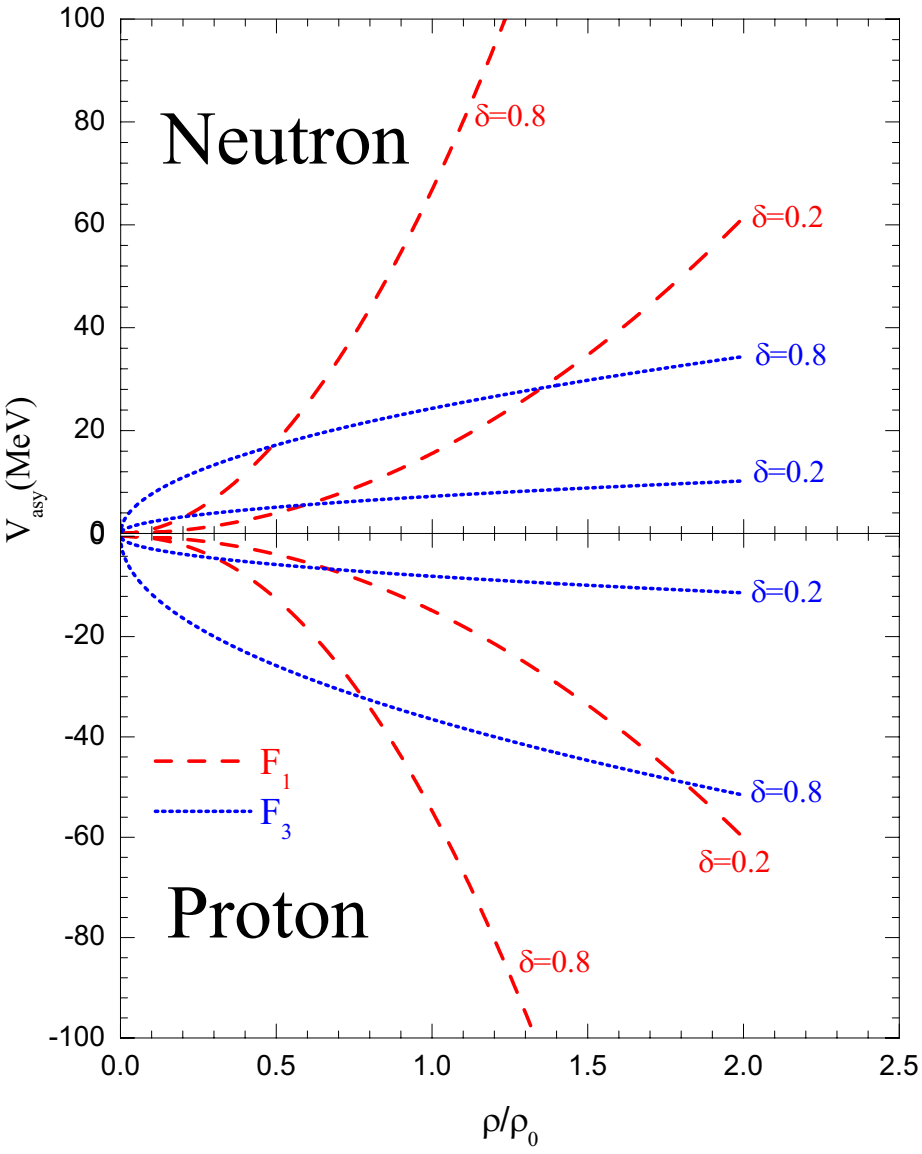

Figure 1.1: The symmetry potential for neutrons and protons corresponding to the two forms of $F(u)$ and $S_0 = 30$MeV with $\delta = 0.2$ and 0.8. Images in this dissertation are presented in color.

1.2 Theoretical Models

The extraction of information about the EOS or the liquid-gas transition of nuclear matter are usually done by comparing experimental data to a theory model calculation. In this dissertation, several models were used. Two of them are the Boltzmann-Uehling-Uhlenbeck (BUU) and Stochastic Mean Field (SMF) models, which make predictions for the reaction dynamics without any assumption about the degree of thermal equilibrium achieved. The other two models, Expanding Emitting Source (EES) and Statistical Multifragmentation Model (SMM), assume some degree of thermalization. In the following, we will discuss and contrast these different approaches.

1.2.1 Boltzmann-Uehling-Uhlenbeck (BUU) Model

The exact theoretical assumption of the collision of two complex nuclei at the incident energies described in the dissertation can be in principle found in the many body Schrödinger equation. This task, however, is fraught with difficulties, both formal and technical, which motivate the introduction of approximate methods that focus on specific aspects of the collisions. Here, we describe an approach formulated to calculate observables that are related to the average dynamics of a collision. The Boltzmann-Uehling-Uhlenbeck (BUU) [113, 74, 51] equation describes time evolution of the single particle phase space distribution function $f_1(\mathbf{p}, \mathbf{r}, t)$ and reads as follows:

$$\frac{\partial f_1}{\partial t} + \frac{\mathbf{p}}{m_1} \cdot \bigtriangledown_{\mathbf{r}} f_1 - \bigtriangledown V \cdot \bigtriangledown_{\mathbf{p}} f_1 = I_{coll} \ , \tag{1.5}$$

where, I_{coll} accounts for collisions and can be written as

$$I_{coll} = -\int \frac{1}{(2\pi)^9} \sigma \mathbf{v}_{12} [f_1 f_2 (1 - f_{1'})(1 - f_{2'}) - f_{1'} f_{2'} (1 - f_1)(1 - f_2)]$$

$$\times (2\pi)^3 \delta^3(\mathbf{p}_1 + \mathbf{p}_2 - \mathbf{p'}_1 - \mathbf{p'}_2) d^3\mathbf{p}_2 d^3\mathbf{p'}_1 d^3\mathbf{p'}_2 \ . \tag{1.6}$$

Here, σ is the differential scattering cross section for a certain change of momentum,

$(\mathbf{p}_1, \mathbf{p}_2) \rightarrow (\mathbf{p'}_1, \mathbf{p'}_2)$, and $\mathbf{v}_{12}$ is the relative velocity for the colliding nucleons. I_{coll} differs from the classical collision by the Pauli-blocking factor $(1 - f_{1(1')})(1 - f_{2(2')})$.

In the BUU equation, V is the mean-field potential, which will be a function of the local density. It can be parameterized as an arbitrary function of density, making it possible to model a variety of equations of state. Typically, it can be written as the sum of three terms:

$$V = V_C + V_n + V_{asy} \ , \tag{1.7}$$

where V_C, V_n and V_{asy} represent the Coulomb potential, the isoscalar nuclear potential and the symmetry energy, respectively.

With the right-hand side set to zero, Eq. 1.5 becomes the Vlasov equation, which describes the evolution of a single-particle distribution under the influence of a self-consistent mean field. Interpreting $f_1(\mathbf{p}, \mathbf{r}, t)$ as the Wigner transform of the quantum mechanical density matrix, the Vlasov equation can be derived from time-dependent Hartree-Fock (TDHF) in the limit of smoothly varying potentials.

To solve BUU equation, given in Eq. 1.5, one often uses the so called *Test Particle* method [5, 30], in which the continuous variables $\mathbf{p}$ and $\mathbf{r}$ are restricted to a set of discrete values, and the phase-space density is represented in terms of a set of δ-functions, or test particles,

$$f(\mathbf{p}, \mathbf{r}, t) = \frac{(2\pi\hbar)^2}{N_{test}} \sum_k \delta(\mathbf{p} - \mathbf{p}_k(t))\delta(\mathbf{r} - \mathbf{r}_k(t)) \ , \tag{1.8}$$

where N_{test} is the number of test-particles per nucleon and δ is the Dirac delta function. In the test particle approach, f solves the BUU equation provided that $\mathbf{r}_k$ and $\mathbf{p}_k$ are themselves the solutions of equations of motion for test particles in a self consistent mean field. The local density can be obtained by integrating f over the momentum.

The changes in the density with time can be predicted by computer simulations, in which the test-particles are required to follow the Hamilton's equations:

$$\begin{aligned} \frac{d\mathbf{r}_k}{dt} &= \frac{\partial H}{\partial \mathbf{p}_k} = \frac{\mathbf{p}_k}{m} \ , \\ \frac{d\mathbf{p}_k}{dt} &= -\frac{\partial H}{\partial \mathbf{r}_k} \ . \end{aligned} \tag{1.9}$$

The spatial gradient in the lower equation can be calculated by taking the difference of the mean field potential between the neighboring points divided by the lattice spacing.

BUU equation can be used to calculate various transport quantities. For the present work, one of the most interesting transport properties is the isospin diffusion coefficient. For the binary fermion system which is composed of neutrons and protons, the isospin current can be shown to depend on the isospin asymmetry and can be written as [93]

$$\mathbf{\Gamma}_\delta = \rho_n \mathbf{v}_n - \rho_p \mathbf{v}_p = -\rho D_\delta \bigtriangledown_{\mathbf{r}} \delta \ , \tag{1.10}$$

where, $\rho_p(\rho_n)$ and $\mathbf{v}_p(\mathbf{v_n})$ are the local nuclear matter density and collective velocity of nucleons, $\delta = (\rho_n - \rho_p)\rho_n + \rho_p)$ is the relative neutron excess and D_δ is the isospin diffusion coefficient.

The diffusion of isospin is driven by isospin concentration, as described by the particle flow equation Eq. 1.10. When self-consistent mean fields produced by the particles depend on the concentration, then this dependence make an important contribution to the diffusion. The diffusion coefficient D_δ therefore depends on the symmetry energy in the equation of state (EOS) and on its density dependence.

In nuclear matter, the isospin asymmetry dependence for both the kinetic and interaction energy per nucleon may be well approximated in the quadratic form of isospin asymmetry, $E_{sym}^{kin(int)} = e_{sym}^{kin(int)}\delta^2$, where e_{sym}^{kin} and e_{sym}^{int} are the kinetic and interaction contributions to the asymmetry coefficient, respectively. In nuclear matter

at normal density, $e^{kin}_{sym0} \approx 12.6$MeV and $e^{int}_{sym0} \approx 19 \pm 6$MeV. The density dependence of the kinetic energy is given by $e^{kin}_{sym}(\rho) = e^{kin}_{sym0}(\rho/\rho_0)^{2/3}$. The density dependence of the interaction symmetry energy, however, is not well constrained experimentally. In light of this uncertainty, one may parameterize this density dependence, calculate experimental observables as a function of this density dependence and identify measurable observables that can be used to constrain it. For example, one can try a power-law dependence on the density, i.e. $e^{int}_{sym}(\rho) = e^{int}_{sym0}(\rho/\rho_0)^{\nu}$.

One can define a mean-field amplification factor $R = D_\delta(e^{int}_{sym})/D_\delta(e^{int}_{sym} = 0)$ for the diffusion coefficient. Predicted values of R from BUU calculations as functions of temperature are shown in the Fig. 1.2, where results for both the linear and quadratic density dependence of $e^{int}_{sym}(\nu = 1$ and $2)$ are shown. The quadratic dependence gives higher amplification factors at $\rho > \rho_0$, than the linear dependence, while the opposite is true at $\rho < \rho_0$. Thus one would expect the stiffer ($\nu = 2$) symmetry energy term to have a large diffusion at high density and the soft ($\nu = 1$) symmetry energy term to have a larger diffusion at lower density as shown by Fig. 1.2. In fact, the diffusion coefficient depends monotonously on the symmetry energy and is large when the symmetry energy is large and small when the symmetry energy is small. At low temperature and moderate to high densities the amplification is very strong suggesting that the measurements sensitive to the diffusion can be used to probe the asymmetry energy. The same calculation also predicts the diffusion coefficient to be reduced by proton-neutron scattering by the residual interaction [93].

1.2.2 Stochastic Mean Field (SMF) model

The BUU equation provides an accurate description of the time dependence of the one body distribution function. Accurate solutions of the BUU equation average away fluctuations in the density that might lead to the formation of fragments in

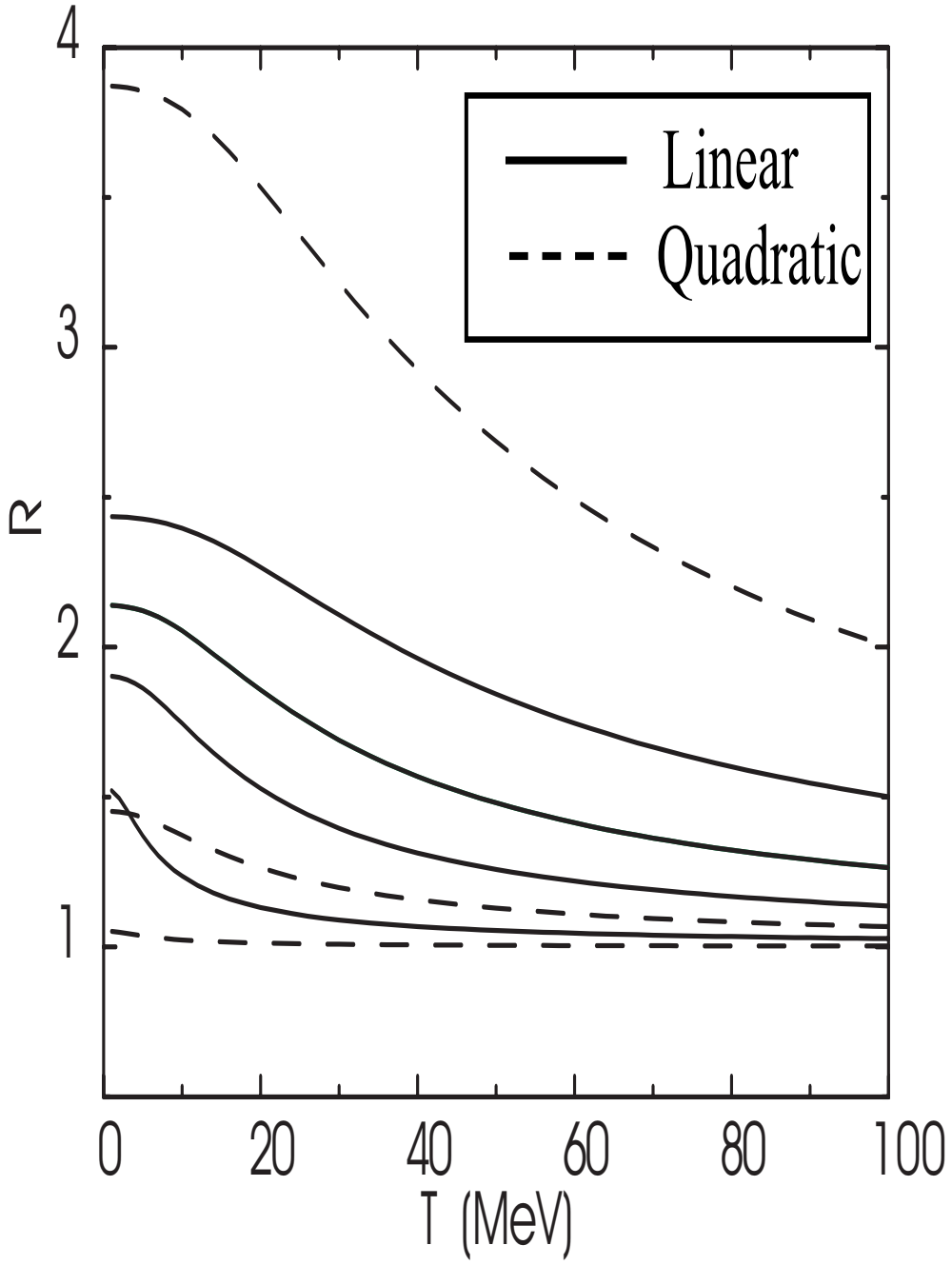

Figure 1.2: Mean-field enhancement factor of the diffusion coefficient in symmetric nuclear matter, $R \equiv D_\delta(e^{int}_{sym})/D_\delta(e^{int}_{sym} = 0)$, at a fixed density n, as a function of temperature T. The solid and dashed lines, respectively, represent the factors for the assumed linear and quadratic dependence of the interaction symmetry energy on density. The lines from top to bottom are for densities $\rho = 2\rho_0$, ρ_0, $0.5\rho_0$, and $0.1\rho_0$, respectively. At normal density the results for the two dependencies coincide. [93]

an individual collision. This is usually achieved by solving the BUU equations with a large number of test particles per nucleon N_{test}. Because the density fluctuations that lead to fragment formation are suppressed in the BUU equation, the calculation of fragment yields directly via the BUU model is not feasible. Therefore, alternative Models, such as Stochastic Mean Field (SMF) model [23] has been developed to address the density fluctuation. SMF, like BUU, describes the time evolution of the collision using a self-consistent mean field. The application of the SMF model to the unstable situations relies on the knowledge of the most important unstable modes, which maybe difficult to identify in cases where the modes are not known apriori.

To account for the stochastic fluctuation in SMF model, two approaches are used. In the first approach, a fluctuating term is added to the standard Boltzmann-Nordeim-Vlasov (BNV) equation to account for the stochastic force, the strength of which is adjusted to reproduce the growth of the most important unstable mode in the system. In practical term, the stochastic force is a type of stochastic noise. The second approach uses this fact by approximating it with numeric noise caused by solving BUU with a small number of test particles (i. e. N_{test}=50) per nucleon.

1.2.3 Statistical Multifragmentation Model (SMM) Model and Macrocanonical Approach

Statistical models assume the existence of statistical (equilibrated) distributions of states during the fragmentation. Equilibrium statistical theories provide one approach to calculate the properties of such fragments. Such models can provide precise predictions. The accuracy of such prediction is directly related to the accuracy of the equilibrium approximation itself.

The copious production of intermediate mass fragments (IMFs), with mass intermediate between that characteristic of light particle evaporation and fission, is a

distinguishing feature of intermediate-energy heavy-ion reactions [73]. The emission of IMFs at low emission rate is a prediction of statistical evaporation theories [37, 69]. The observation of very high IMF multiplicities, however, lies outside of the realm of prediction of evaporation theories [15, 37]. Such an observation suggests a different mode of decay via a bulk disintegration [10, 37, 42].

Microcanonical Statistical Multifragmentation Model (SMM) uses a Monte Carlo method to calculate physics observables in approximate microcanonical equilibrium approach [102]. If one assumes that equilibrium is achieved for a source with excitation energy E_0^*, volume V, mass A_0 and charge Z_0 specified. Possible decay modes are weighted by the entropy of that decay mode within this volume. All decay modes that conserve the total mass, total charge and total energy are constructed.

The entropy of each decay mode is assumed to be additive and is obtained from the entropy of the individual fragments. Both energies and entropies for individual fragments can be calculated from the free energy of the individual fragments [14]

$$\begin{aligned} F_{AZ}(T) = (-W_0 - \frac{T^2}{\epsilon_0})A + 18(\frac{T_c^2 - T^2}{T_c^2 + T^2})^{5/4}A^{2/3} \\ +25\frac{(A-2Z)^2}{A} + \frac{3}{5}\frac{Z^2e^2}{R_{AZ}}[1-(1-\kappa)^{-1/3}] \\ - T\ln\left[g_{AZ}\kappa V_0(\frac{m_n AT}{2\pi\hbar^2})^{3/2}\right] + T\frac{\ln(N_{AZ}!)}{N_{AZ}} \ , \end{aligned} \tag{1.11}$$

where, $W_0 = 16$MeV is the binding energy of nuclear matter; ϵ_0 is the inverse nuclear level density ($\epsilon_0 \approx 16$MeV for the Fermi gas model); $T_c = 16$MeV is the critical temperature; $R_{AZ} = 1.17A^{1/3}fm$ is the radius of a fragment corresponding to normal nuclear matter density ρ_0; m_N is the nucleon mass; g_{AZ} is the spin degeneracy factory; κ is a model parameter, which is introduced since the individual fragments are assumed to move freely in a volume of κV_0; V_0 is the volume of the system corresponding to normal nuclear matter density ρ_0.

The first two terms in the r.h.s. are the contributions from volume and surface;

the third term is from symmetry energy; the fourth term is from Coulomb interaction and the last two terms are from the translational motion. In this approximate microcanonical approach the internal degree of freedom of the fragments act somewhat as a heat reservoir. The temperature T of the fragments are then determined by the equation for overall energy conservation.

The equilibrium can also be more approximately studied within macrocanonical frame work, which provides some insightful approximate expressions. Under the Macrocanonical approach, the fragment yield for i^{th} fragment in its k^{th} state can be written as [1]

$$Y_{i,k}(A,Z) = V\frac{A_i^{3/2}}{\lambda^3}(2J_{i,k}+1)e^{\frac{N\mu_n+Z\mu_p}{T}}e^{\frac{B(N,Z)}{T}}e^{\frac{-E_i^*}{T}} \quad , \qquad (1.12)$$

where, $Y_{i,k}(A,Z)$ is the yield of a given fragment with mass A and charge Z; $B(A,Z)$ is the binding energy of this fragment; and $J_{i,k}$ is the ground state spin of a nucleus with charge Z and mass A; μ_p and μ_n are the proton and neutron chemical potentials; $\lambda = \sqrt{2\pi\hbar^2/m}$; V is the free(unoccupied) volume of the system and T is the temperature.

Eq. 1.12 describes the primary fragment yields. The fragment yields from experiment are the yields after secondary decay. To minimize the effects of the secondary decay, in some cases, one can construct observables that are approximately insensitive to the secondary decay. One can construct the ratio of the fragment yields for the same isotope from two different reactions under similar conditions. By taking this ratio in the macrocanonical approximation Eq. 1.12, one finds that the volume and binding energy factor cancel out. If the feeding from the decay of particles of stable or unstable states are similar in the two reactions, it may cancel approximately as well. In this case, if we define R_{21} as the ratio of isotope yields from two different reactions

1 and 2, $R_{21} = Y_2(N,Z)/Y_1(N,Z)$, the following isoscaling relationship [110] is found to be quite robust in nuclear reactions

$$R_{21} \propto e^{\alpha N + \beta Z} \ , \tag{1.13}$$

where, $\alpha = (\triangle\mu_n/T) = (\mu_{n2} - \mu_{n1})/T$ and $\beta = (\triangle\mu_p/T) = (\mu_{p2} - \mu_{p1})/T$. Fig. 1.3 illustrates the isoscaling property observed with the fragments produced in the mid-rapidity region of ^{124}Sn + ^{124}Sn and ^{112}Sn + ^{112}Sn reactions [123]. Here, ^{124}Sn + ^{124}Sn is the reaction 2 and ^{112}Sn + ^{112}Sn is the reaction 1.

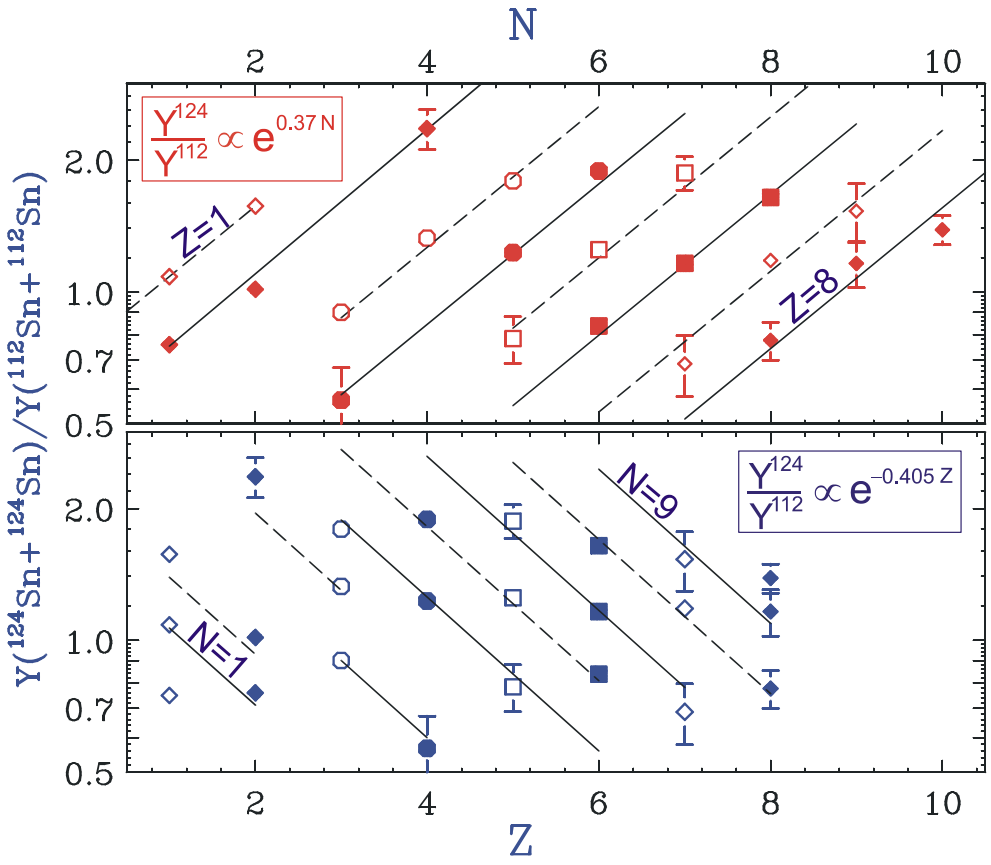

Figure 1.3: Experimental isoscaling behavior exhibited by the central ^{124}Sn + ^{124}Sn and ^{112}Sn + ^{112}Sn collisions. The data are the nuclide yield ratios, $R_{21}(N,Z)$ from the two reactions plotted as function of N (top panel) and Z (bottom panel)

α and β can be shown to directly relate to the neutron excess δ, i. e. $\alpha \propto (\delta_2 - \delta_1)(1 - (\delta_1 + \delta_2)/2)$ [111]. We are going to use α as an observable to study the density dependence of the asymmetry term and explore the isospin diffusion in this dissertation.

1.2.4 Expanding Emitting Source (EES) Model

The achievement of equilibrium assumed in Sec. 1.2.3 can be achieved and maintained only if the emission of particles and their absorption by collisions with other particles are in detailed balance. Statistical surface emission provides a way to calculate the rates and to describe how an excited system might proceed towards equilibrium or away from it. In this section, we discuss the Expanding Emitting Source (EES) [37, 38] model which calculates the binary decay of excited nuclei via emission rate equations within a statistical frame work. This formalism, which allows the description of time dependent phenomena, integrates the contributions for each type of particle as a function of time over the de-excitation process. The formulae that describe the surface emission mechanism are similar to those developed by Weisskopf's seminal paper on compound nuclear decay [119]. They are also conceptually similar to the ideas of Richardson's thermionic emission.

Let us consider the decay of a compound system labeled C into a daughter B, capable of further decay, and a particle labeled b,

$$C \qquad \longrightarrow \qquad B + b \qquad .$$

Let N_b be the number of emitted particles of type b. Then $\frac{d^2 N_b}{dt dE}$ expresses the rate of emission (at kinetic energy E in to a given interval dE) of that type of particle.

The energy spectra can be obtained from the double differential quantity

$$\frac{dN_b}{dE} = \int_0^\infty \frac{d^2 N_b}{dE dt} dt \ . \tag{1.14}$$

The emission rate is obtained by an energy integeration

$$\frac{dN_b}{dt} = \int_0^\infty \frac{d^2N_b}{dEdt} dE \ , \tag{1.15}$$

and the multiplicity by a further time integeration

$$N_b = \int_0^\infty \frac{dN_b}{dt} dt \ . \tag{1.16}$$

The rate of emission using the approach of Weisskopf [119] can be written as

$$\frac{dN}{dEdt} = (\frac{2s+1}{\pi^2\hbar^3}) EM\sigma_{b+B\to C}[\omega_B(E_B^*)/\omega_C(E_C^*)] \ , \tag{1.17}$$

where M, E, and s refer to the mass, kinetic energy and spin of the emitted particle b; and $\omega_B(E_B^*)$ is the density of states for the daughter system B at excitation energy, E_B^*, which remains after particle b is emitted with kinetic energy E from the compound system C, originally having excitation energy E_C^*. The quantity $\sigma_{b+B\to C}$ is the cross section for the formation of system C which we take to be geometrical.

For the basic EES calculation, initial temperature and excitation energy need to be specified for the EES calculation. The evaporation is complicated by other factors, i.e. the isospin of the excited system, the recoil momentum of the target, the reduction of the Coulomb barrier which accompanies charge emission as well as the range of temperatures traversed. A discussion can be found in [37]. The EES model allows expansion of the nucleus subject to its internal pressure and predicts a rapid emission of fragments once the density of the residue decreases below about $0.4\rho_0$. This suggests that the multifragmentation principally occurs after the system expands to subnuclear density.

1.3 Studies Prior to This Dissertation

The isospin-dependent Boltzmann-Uehling-Uhlenbeck (BUU) transport model has successfully explained several isospin-dependent phenomena in heavy-ion collisions at intermediate energies [61]. In isospin-dependent Boltzmann-Uehling-Uhlenbeck (BUU) transport model, the isospin dependence was included in the dynamics through nucleon-nucleon collisions by using isospin-dependent cross sections and Pauli blocking factors, the symmetry potential $V_{asy}^{n(p)}(\rho,\delta)$ and the Coulomb potential. The isospin-dependent BUU model was used to calculate the ratio of yield of neutron and protons in pre-equilibrium emission [63]. It is found that if one drops the Coulomb and asymmetry term $V_{asy}^{n(p)}(\rho,\delta)$ in the BUU model, the ratio of pre-equilibrium neutrons to protons is almost a constant as a function of nucleon kinetic energy. However, when one includes the Coulomb and the asymmetric term of the EOS, the ratio of pre-equilibrium neutrons to protons changes monotonously as a function of nucleon kinetic energy. Fig. 1.4 has shown this calculation. One can then study the effects of the symmetry energy $S(\rho)$ since the Coulomb potential is well understood. Since the symmetry potential $V_{asy}^{n(p)}(\rho,\delta)$ tends to make more unbound neutrons than unbound protons, one expects that a stronger symmetry potential leads to a larger ratio of free neutrons to protons. One can see from the figure that the effects of symmetry potential show up at higher energy for central collisions and at lower energy for peripheral collisions.

A naive picture of nuclear reactions at intermediate energies undergoes three important stages: compression and expansion stage when the preequilibrium light particles are emitted, after which a prefragmetation source is formed; the disassembly stage (evaporation) after the prefragmetation source reaches equilibrium; a secondary decay process of various emitted fragments. While the dynamic model such as BUU and SMF give a good description of preequilibrium emission during the compres-

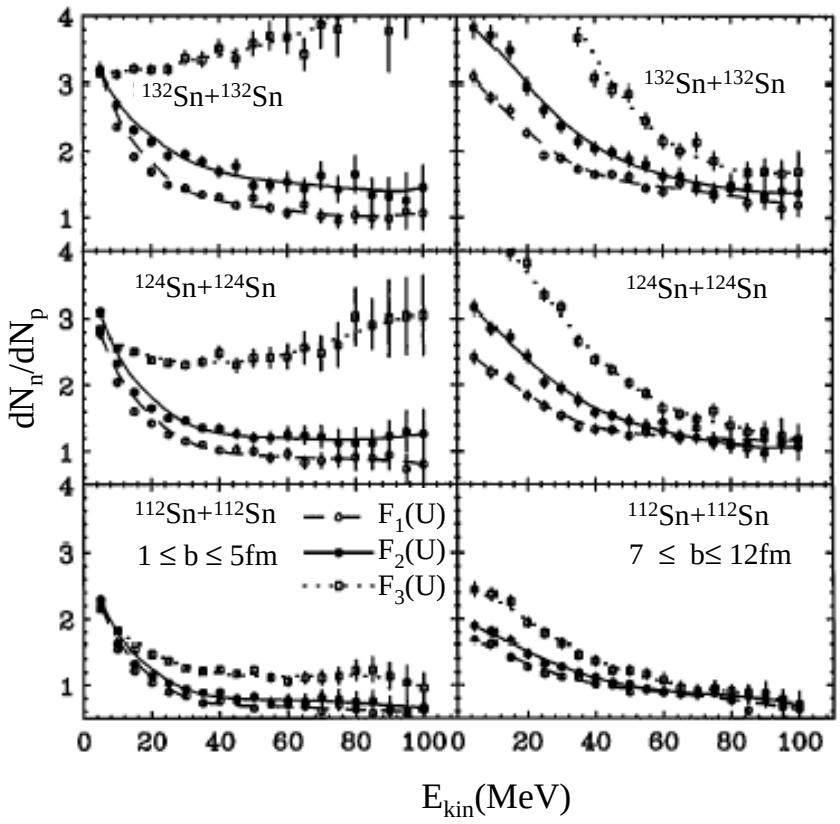

Figure 1.4: The ratio of pre-equilibrium neutrons to protons as a function of nucleon kinetic energy for central (Left Panel) and peripheral (Right Panel) calculated from the isospin-dependent BUU model with both the Coulomb and symmetry potentials [63].

sion and expansion stages, the statistical models give a better description of the later stages as equilibrium is approximately achieved. At the end as hot fragments decay to their ground states, nuclear structure data such as level densities and binding energies are needed to describe the secondary decay process. It may be that the combination of different models to describe the different stages of the reaction can give a better description of the experiment data than can any of them individually. Hybrid models in which the internal dynamics is described by a dynamic model and the later stage by a statistical model have been attempted and used to test the asymmetry term of EOS. Fig. 1.5 shows one of such calculations for the data obtained from central Sn+Sn collisions. The data and calculations shown are based on the Eq. 1.13 and uses ^{112}Sn+^{112}Sn as reaction 1. In this figure, $\hat{\rho}_n$ and $\hat{\rho}_p$ are plotted as functions of N_{tot}/Z_{tot}. Where, $\hat{\rho}_n$ and $\hat{\rho}_p$ are just the e^{α} and e^{β} defined in Eq. 1.13, respectively; N_{tot} and Z_{tot} are the total numbers of neutrons and protons involved in reaction 2. The experimental data are shown as solid circles and squares while the open and cross-hatched rectangles show corresponding hybrid calculations of R_{21} obtained with the asy-stiff (left panel) and asy-soft (right panel) EOS's respectively [101]. We can see from this figure the final yields with the asy-stiff EOS (left) panel overlap the data. In comparison, the calculations using the asy-soft EOS (right panel) show a significantly weaker dependence on N_{tot}/Z_{tot} than do the data. In this dissertation, we will use a different type of hybrid model to study the density dependence of the asymmetry term in EOS.

1.4 Thesis Organization

In this dissertation, Chapter 2 describes the experimental setup, i.e. the devices involved in the experiment of this dissertation: The Large Area Silicon-Strip/CsI detector Array (LASSA), The Ring Counter and Miniball/Miniwall array. Chapter 3

describes the data analysis, i.e. the energy calibration for the detectors and extraction of PID function. Chapter 4 provides the experiment results and various comparisons with model calculations. Chapter 5 summarizes the thesis and provides the conclusions.

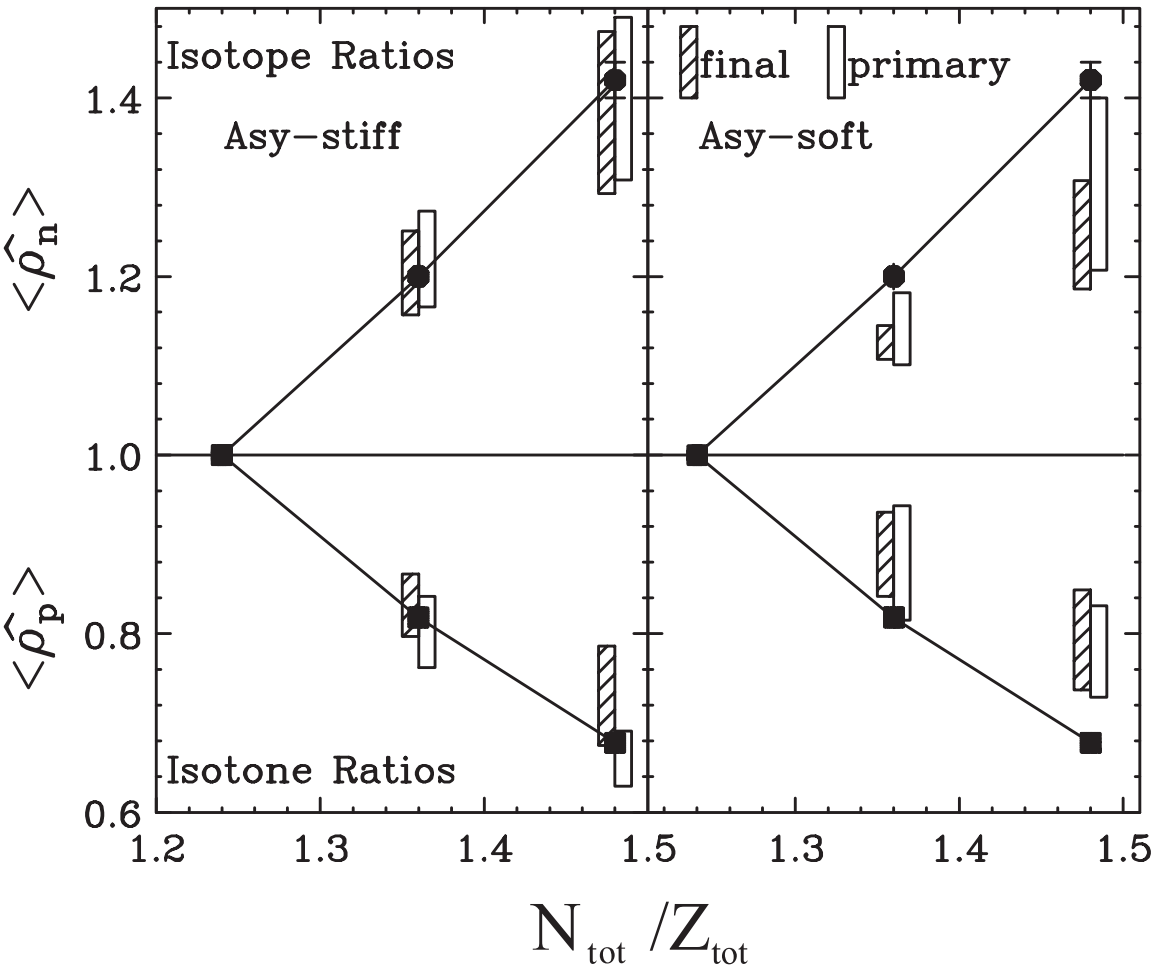

Figure 1.5: Both Panels: The solid circles and solid squares show values for $\hat{\rho}_p$ and $\hat{\rho}_n$, respectively; measured in central ^{112}Sn+^{112}Sn, ^{112}Sn+^{124}Sn, and ^{124}Sn+^{124}Sn collisions at E/A =50MeV. Left panel: The open and cross-hatched rectangles show corresponding hybrid calculations for R_{21} calculated from the primary and final fragment yields, respectively, predicted by the hybrid calculations using the asy-stiff EOS. Right panel: The open and cross-hatched rectangles show corresponding hybrid calculations for R_{21} calculated from the primary and final fragment yields, respectively, predicted by the hybrid calculations using the asy-soft EOS.

Chapter 2

Experimental Setup

2.1 Experimental Layout

The thesis experiment was performed at the National Superconducting Cyclotron Laboratory at Michigan State University with beams from the K1200 accelerator. ^{112}Sn+^{112}Sn, ^{124}Sn+^{112}Sn, ^{112}Sn+^{124}Sn, ^{124}Sn+^{124}Sn collisions were measured by using 50MeV per nucleon ^{112}Sn and ^{124}Sn beams and 5 mg/cm^2 ^{112}Sn and ^{124}Sn targets. Three major devices were used in the experiment:

(1) Nine telescopes of the Large Area Silicon Strip Array (LASSA)

(2) The Miniball/Miniwall phoswich detector array.

(3) The annular silicon strip forward array (the Ring Counter)

Fig. 2.1 shows a photograph of these detectors used in this experiment. This photograph is taken towards the downstream direction of the beam. In this picture, one can see six of the nine LASSA telescopes. These are the large square telescopes mounted above the beam axis. One can also see the Ring Counter, which appears as a ring around the beam exit hole, just under the LASSA telescopes. The other detectors in the picture are various elements of the Miniball array.

The LASSA detector Array is a large area, highly segmented silicon-strip/CsI de-

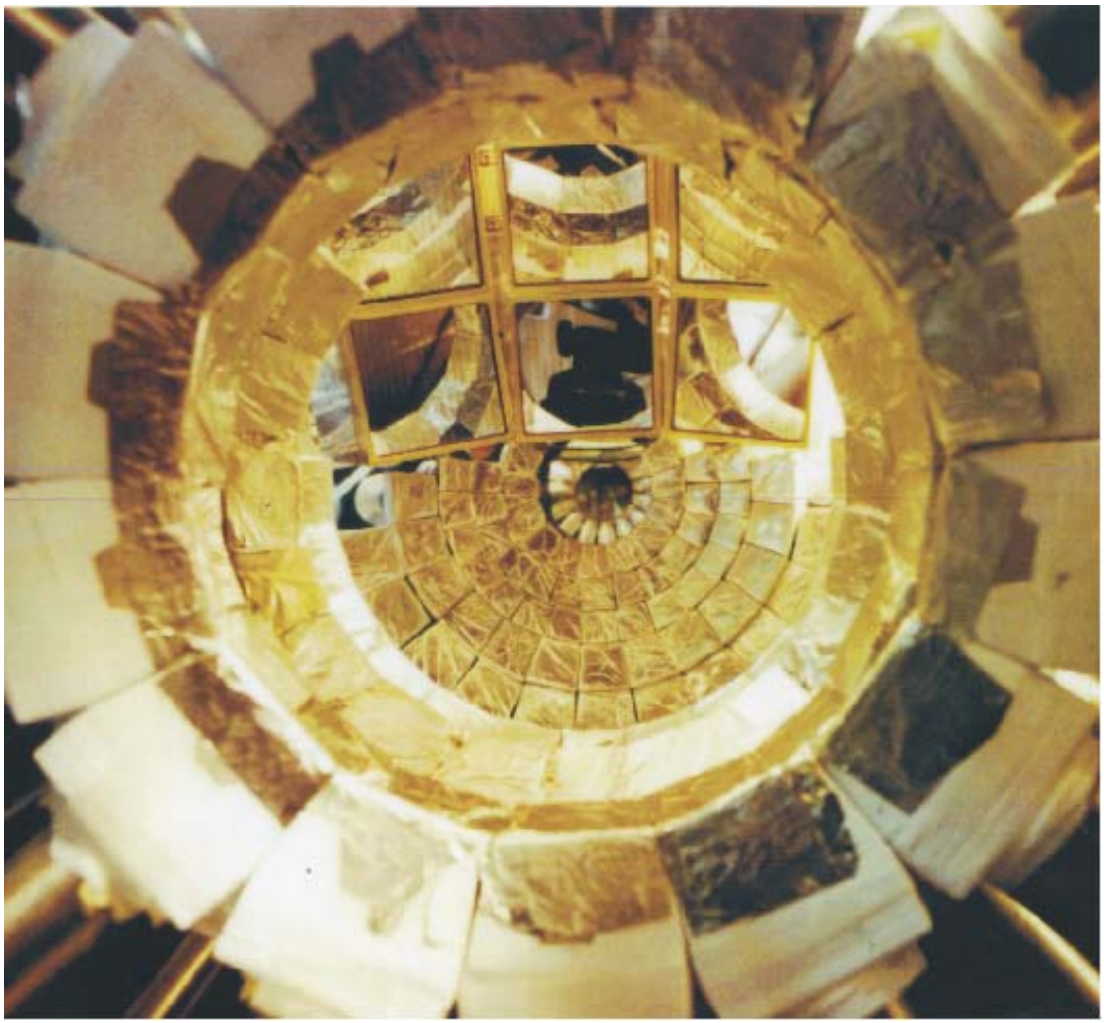

Figure 2.1: Major detectors used in the experiment, viewing in the downstream direction of the beam

tector array. It provides excellent energy, angular and isotopic resolution for isotopes with $Z \leq 8$. In this experiment, LASSA is used to measure the fragments produced from central collisions as well as the fragments from the projectile-like source. The Miniwall/Miniball multi-detector array is a moderate resolution detector array for detecting charged particles. The Miniball detectors can identify elements with $Z \leq 18$ and isotopes for $Z \leq 2$. This array was employed to select impact parameters in this experiment. The impact parameters were selected by gating on the multiplicity of identified charged particles.

The Ring Counter forward array is also a highly segmented silicon-strip/CsI detector array. It provides atomic-element resolution for fragments with $3 \leq Z \leq 55$ (Z is atomic number) as well as excellent angular position information. The Ring Counter was used to detect projectile-like fragments (PLFs).

The LASSA detector array was constructed specifically for this experiment, while Miniwall/Miniball multi-detector array and the Ring Counter forward array are existing devices available for use in this experiment. Details of the detectors are discussed in the following sections.

Fig. 2.2 is a schematic drawing of the mechanical layout of this experiment. LASSA, which was centered at 32.5°, subtended polar angles from 7° to 58°. The Miniwall/Miniwall detector array covered polar angles from 6.95° to 150°. The geometric acceptance of Miniball/Miniwall is about 76% of the 4π solid angle. The Ring Counter, which is an annular shaped detector, was put at the most forward angle. It was centered about the beam line and covered polar angles from 2.2° to 4.5°. The relative placement of the LASSA and the Ring Counter can be viewed in the Fig. 2.2 and Fig. 2.3.

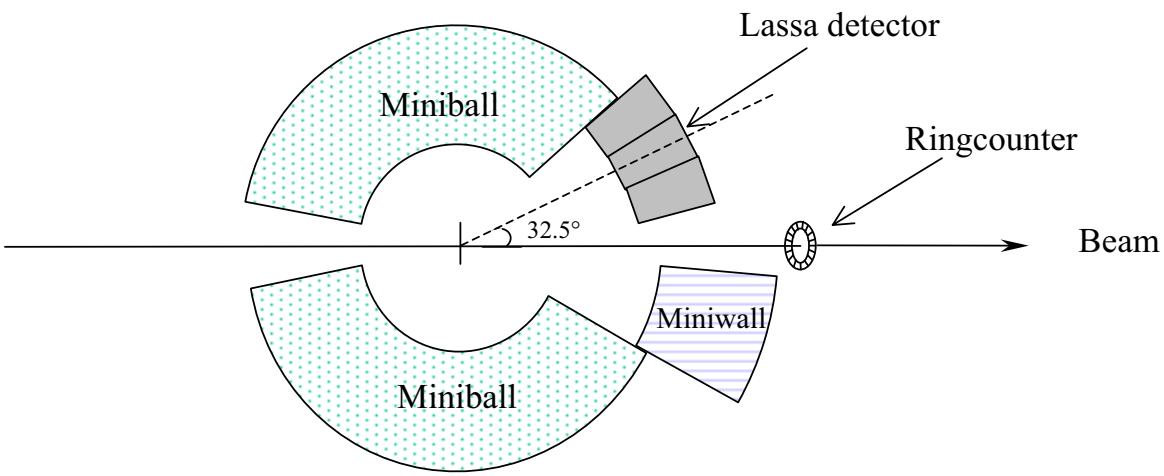

Figure 2.2: Mechanical Layout of the experiment, viewed from the side

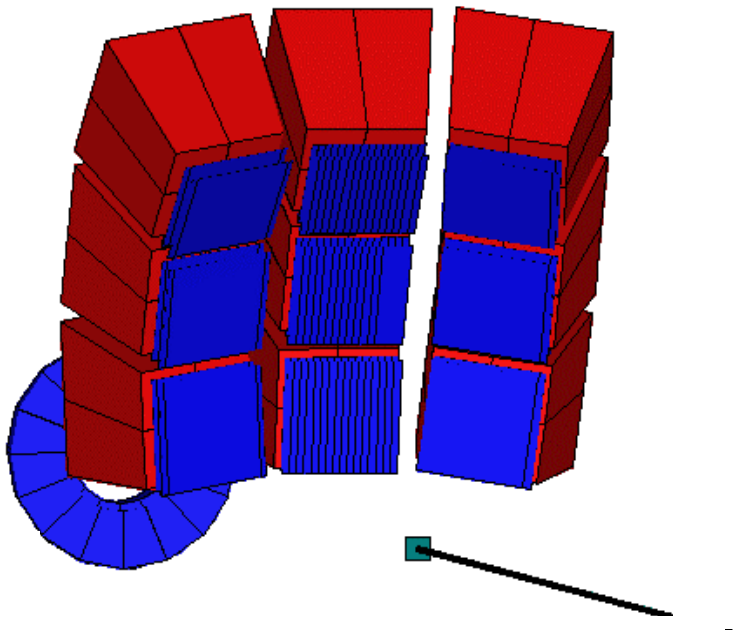

Figure 2.3: The relative position of LASSA and the Ring Counter

2.2 LASSA Telescopes

The Large Area Silicon-Strip/CsI detector Array, LASSA [32], consists of nine individual telescopes, instrumented with strip silicon detectors. It provides high angular, energy and wide-range isotopic resolution, a large detection area and a reasonable energy range for the detected particles.

Structure of LASSA Detector

A photo of a single telescope is shown in Fig. 2.4. A schematic of a single telescope is also shown in Fig. 2.5. There are three layers of detectors in each telescope. The first two layers are highly segmented strip silicon detectors. These strip detectors are backed by four CsI(Tl) detectors, which constitutes the third layer of detectors. The first silicon detector, which we called the "DE" detector, is a 65 μm thick silicon detector with 16 strips on one side of the detector; the total area of the detector is 50×50 mm^2 with each strip 50mm in length and 3mm in width. The second silicon detector, called "EF/EB", is a double-sided, 500μm thick silicon detector with 16 strips on each side, the direction of the strips on the front side are perpendicular to the strips on the back side; the area of the EF/EB detector is also 50x50mm^2 with the strips on each side being 3mm in width. For both the first and the second silicon detectors, the gap between the strips is about 0.1mm. The third layer of detectors consists of four CsI crystals. Each of these has an active area of 2.5×2.5 mm^2 and each is 60mm in thickness. The crystals are tapered such that front and back surfaces subtend the same solid angle with respect to the target.

Principle of Operation

Each telescope in LASSA functions as an energy loss telescope. An energy loss telescopes identifies the charge, mass, and energy of charged particles in the following

Figure 2.4: Photo of a single LASSA telescope. The Silicon detectors are not mounted and one of the side covers is removed to show the CsI detectors.

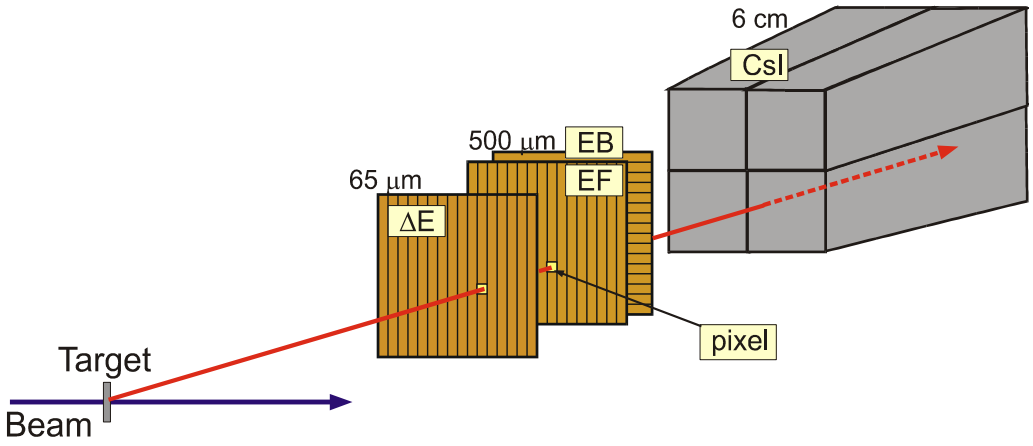

Figure 2.5: A schematic drawing of the LASSA detector

way. For particles passing through a detector, the loss energy is proportional to the stopping power. The energy loss can be approximated by Bethe formula:

$$\triangle E \approx \frac{kAZ^2}{E} dx \ , \tag{2.1}$$

where dx is the detector thickness, k is a proportionality constant, A is the mass number of the particle, and Z is the atomic number of the particle. One can easily see that for a given dx, a plot of E verses $\triangle E$ will yield a family of a contours with $\triangle E \propto 1/E$. Each line corresponds to an integer value of Z, and an integer values of A.

If the various detectors generate signals proportional to the energy deposited by the charged particle, then digitized signals can be used to identify the particles using this energy loss relation. It is true for the detectors making up the LASSA telescope. When a charged particle passes through a silicon detector in LASSA, for example, it generates a signal that has a linear dependence of the energy it deposited. When a charged particle stops in the CsI(Tl), it generates a measurable light output which is roughly proportional to the energy deposited by the particle in the CsI. Thus when we plot energy loss in silicon vs. light output from CsI, we can expect to see the

contours of $\triangle E \propto 1/E$, offset for each isotope according to the integer values of the atomic number Z and mass number A. One can deduce the relationship between E, $\triangle E$ and Z, A, $E_{tot} = \triangle E + E$ empirically or analytically. In either case, we can construct a PID function or PID value which uniquely identifies the Z and A of the charged particle from the measured values of $\triangle E$ and E. In this thesis, we determine the PID empirically.

The data for the LASSA telescope are analyzed as follows: If a charged-particle passes through the first silicon and stops in the second silicon, then the signals from the first and the second silicons are used to yield the angle, energy and PID information. If the charged particle passes both silicons and stops in the CsI, then the all the signals from the silicon detectors and the CsI crystal are used to give out angle, energy and PID (i.e. Z and A) information. By detecting the charged particle this way, we can take advantage of the high angle and energy resolution of silicon detector as well as large energy detecting range of the CsI(Tl) detector. Fig. 2.6 plots the measured energy loss in the DE detector verses measured energy loss in the EF detector. In Fig. 2.7, we plot the measured energy loss from the silicon detectors(with DE and EF signals added together) verses that of the CsI crystals. Note that roughly hyperbolic lines we see in both figures correspond to the various isotopes. In addition, on the Fig.2.6, we see the isotope lines turn over at the lower right side and then continue toward lower values of DE and EF. The particles corresponding to these lines "punch-through" both of the silicon detectors, and stop in the CsI crystal. The energy of the charged particle was obtained from the calibrated signals from the silicons and CsI(Tl). The position information was given mainly by the signals from the EF and EB strips of the second silicon detector.

LASSA provided isotopic identification for fragments with $Z \leq 8$ and the energies of these fragments to better than 3% accuracy. For the energy calibration and

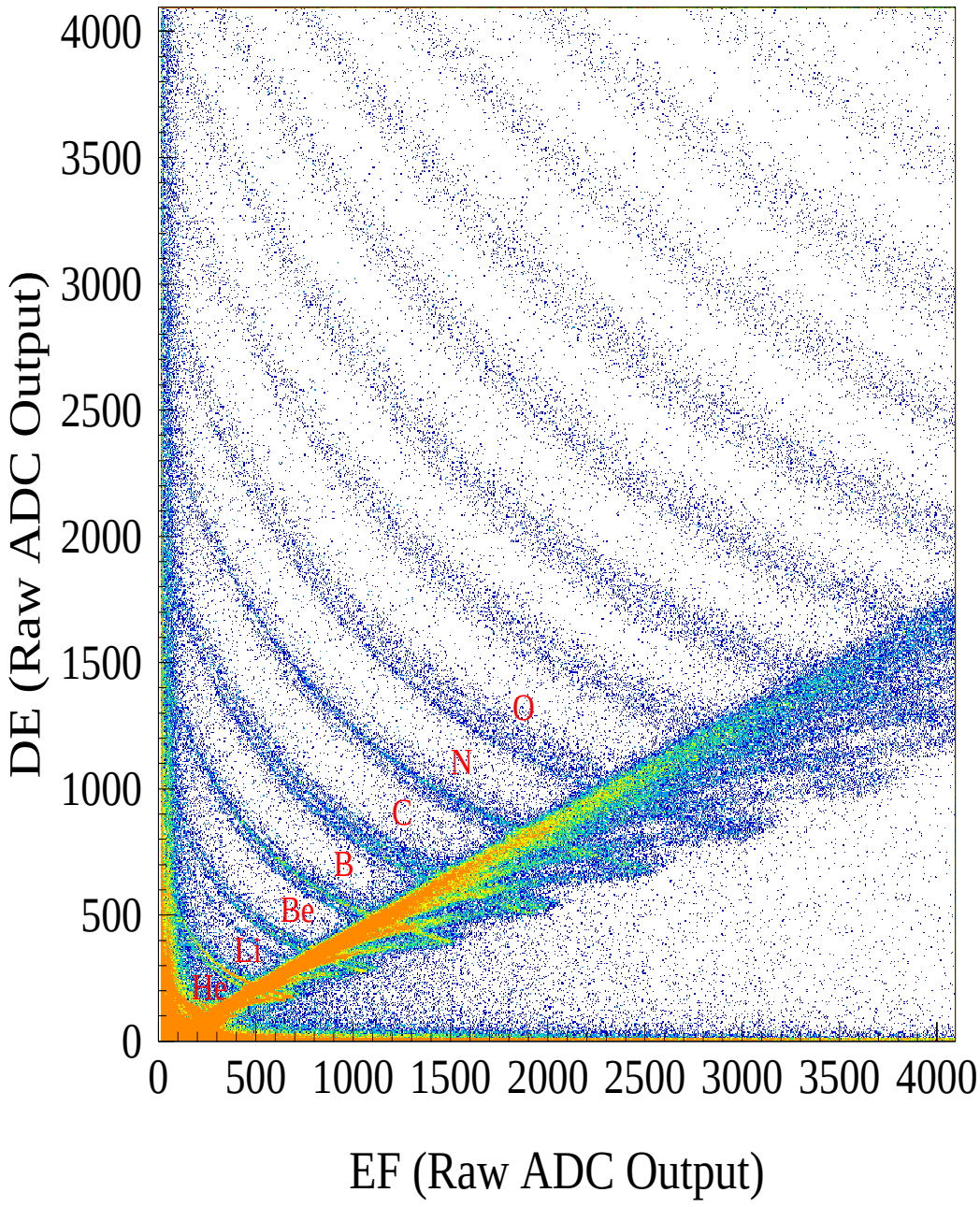

Figure 2.6: A two dimensional histogram of the raw signal outputs of DE (first silicon) vs. EF (second silicon). In the figure, below the element labels, one can see the hyperbolic lines for various isotopes of the elements.

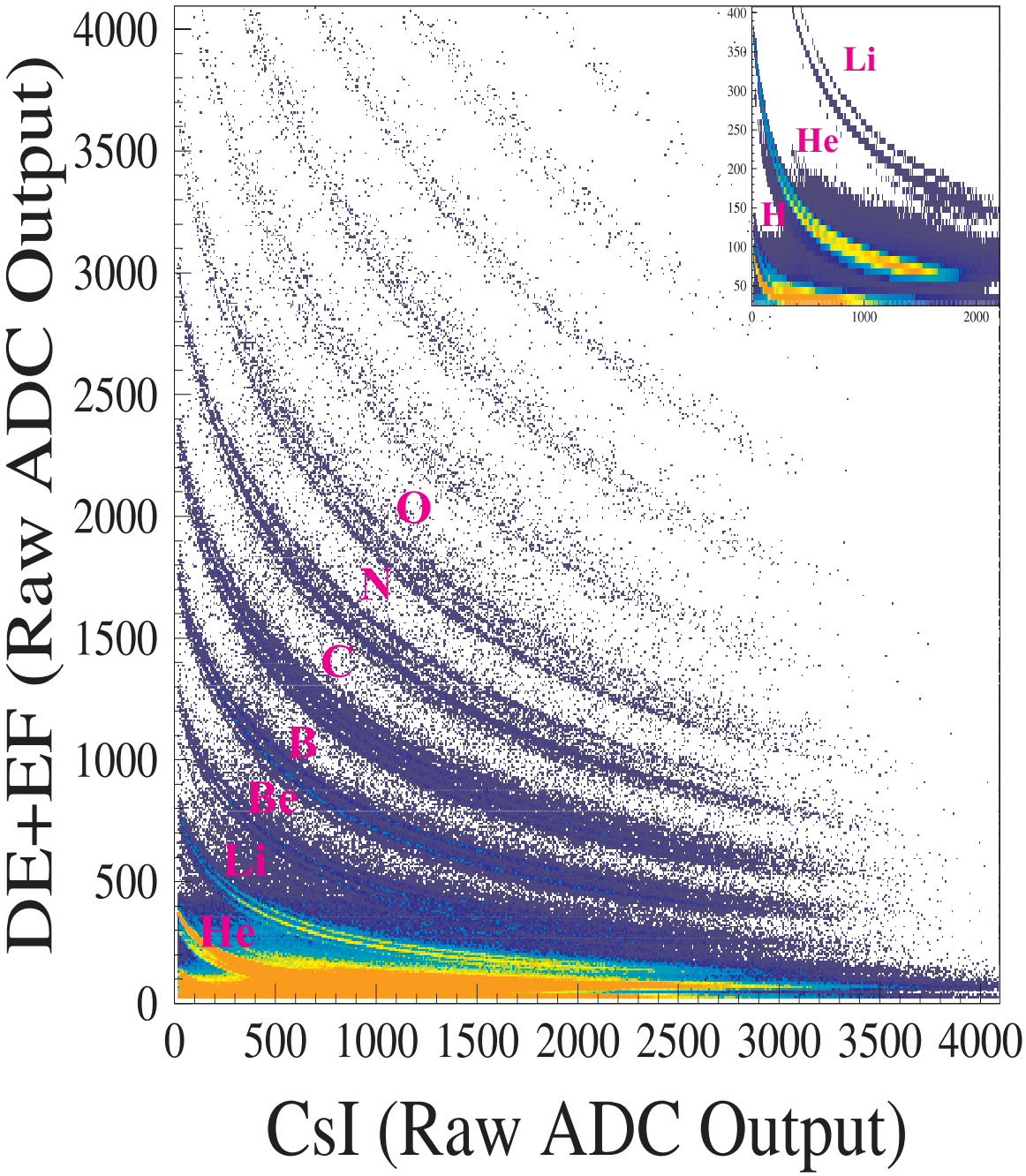

Figure 2.7: A two dimensional histogram of the raw output signals of DE+EF (silicon) vs. E (CsI). In the figure, below the element labels, one can see the hyperbolic lines for various isotopes of the elements.

multiple hit decoding of LASSA, details can be found in the next chapter.

Solid Angle Coverage

The LASSA telescope array was put at 20cm from the target and centered at a forward angle of 32.5°. The 3mm width for the strips of the silicon detectors at a distance of 20mm corresponds to a width in angle of 0.86°. The position of the center of each "pixel" (e.g. the intersection of the strips with perpendicular directions, EF and EB) can be seen in Fig. 2.8. At the upper left corner, the relative placement of the 9 telescopes is shown. The given number corresponds to the labeling scheme for the telescopes during the experiments. The whole array covers azimuthal angles ranging from approximately 50° to approximately 150°, and polar angles from approximately 7° to approximately 58°.

Electronics of LASSA

High quality pre-amplifiers (PA) were used for LASSA to achieve high-energy resolution. Given the number of channels involved and the space constraints, all pre-amplifiers were constructed using surface mount technology, with the exception of the input field effect transistor (FET) and the load resistor. The pre-amplifiers of CsI, which amplified the signal of the photodiodes of the CsI crystals, were installed inside the LASSA telescope; the silicon preamplifiers were mounted in separate boxes adjacent to the LASSA array.

There are 432 Silicon channels in LASSA. A total of thirty 16-channel Analog-to-digital Converter (ADCs) and nine Fast Encoding and Readout ADCs (FERAs) modules (for the timing signals) were required to read out all the silicon signals from LASSA. The large number of channels in LASSA required development of an integrated shaper/discriminator module that would allow easy computer control of the

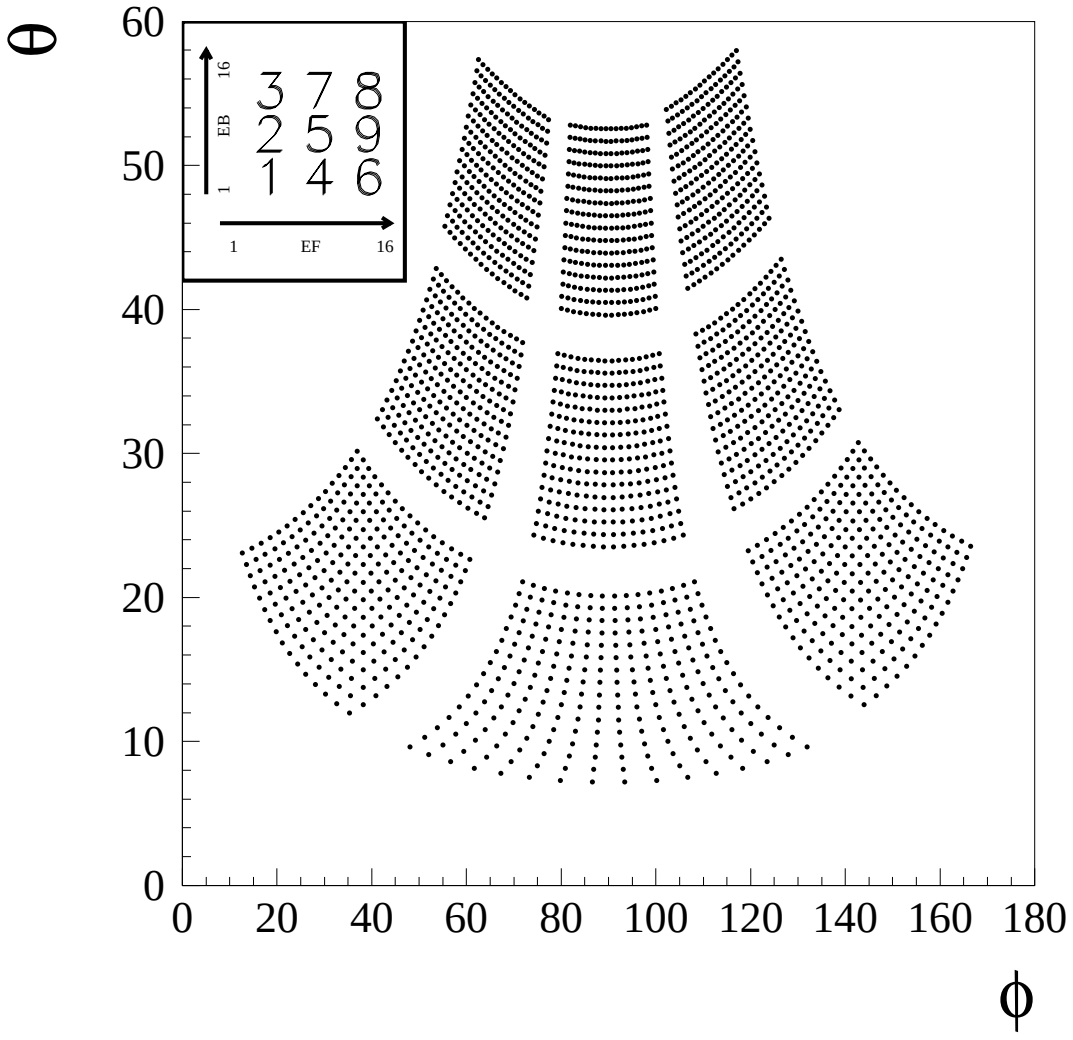

Figure 2.8: A two dimensional graph of the solid angle coverage of LASSA in polar angle θ and azimuthal angle ϕ

LASSA electronics, including the gain of the energy signals and discriminator thresholds. These special double-width Computer Automated Measurement and Control (CAMAC) modules were developed by Washington University. Each module consists of a slow shaper, a timing filter amplifier, a leading edge (LE) discriminator, and a time-to-charge converter (TFC) for each of the 16 independent channels. These special modules can be controlled by computer via a GPIB CAMAC interface. In the experiment, a precision pulser (IU pulser) was used to track changes in electronic gain. This pulser is stable to within 0.1% and can be controlled by a computer via an RS-232 serial interface. A schematic of the LASSA electronics can be seen in Fig. 2.9 [32].

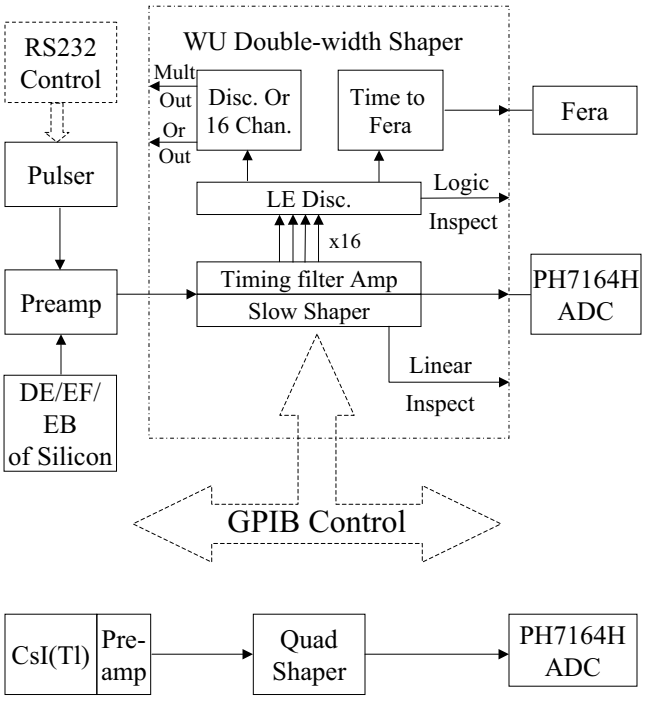

Figure 2.9: A schematic of the elctronics for the LASSA telescope

2.3 The Miniball/Miniwall Array

Structure of Miniball/Miniwall

The Miniball detector array [96] is a 4π detector array. It consists of 11 independent coaxial rings centered about the beam axis, with each ring at a specific polar angle. A total of 188 fast-plastic CsI(Tl) phoswich can be mounted on these rings. Each phoswich detector consists of a 8mg/cm^2 (80μm) thick plastic scintillator foil and a 2 cm thick CsI(Tl) crystal. The shape of the front face of the crystals are the same within each ring but differ among rings, forming a spherical surface facing the target. The front face of the phoswich assembly is covered by an aluminized mylar foil (0.15mg/cm^2 mylar and 0.02mg/cm^2 aluminum). The crystal is coupled by a light-guide to the photo-multiplier (PM) tube. The photomultiplier tube and the cylindrical light guide are surrounded by a cylindrical μ-metal shield. Fig. 2.10 shows a schematic drawing (the cylindrical μ-metal shield is not shown).

Since the angular distribution of emitted particles in heavy-ion collisions is strongly forward peaked [53], an additional Miniwall detector array [121] was constructed by Washington University to cover the forward angle $\theta \leq 25^\circ$. The Miniwall detector array was constructed as an azimuthal group of the phoswich detectors similar to the Miniball array. It consists of 6 rings, with a total of 128 detectors. Each of the Miniwall detectors was made with 3cm thick CsI(Tl) scintillator crystals and 8mg/cm^2 thick scintillator foils.

Principle of Operation

The Miniball/Miniwall detector is based on the plastic-CsI(Tl) phoswich technique, and detects charged particles in the following way: When charged particles pass through the fast-plastic scintillator or the Tl-doped CsI crystal, visible light is generated. This light is collected and converted to amplified electric signals by the pho-

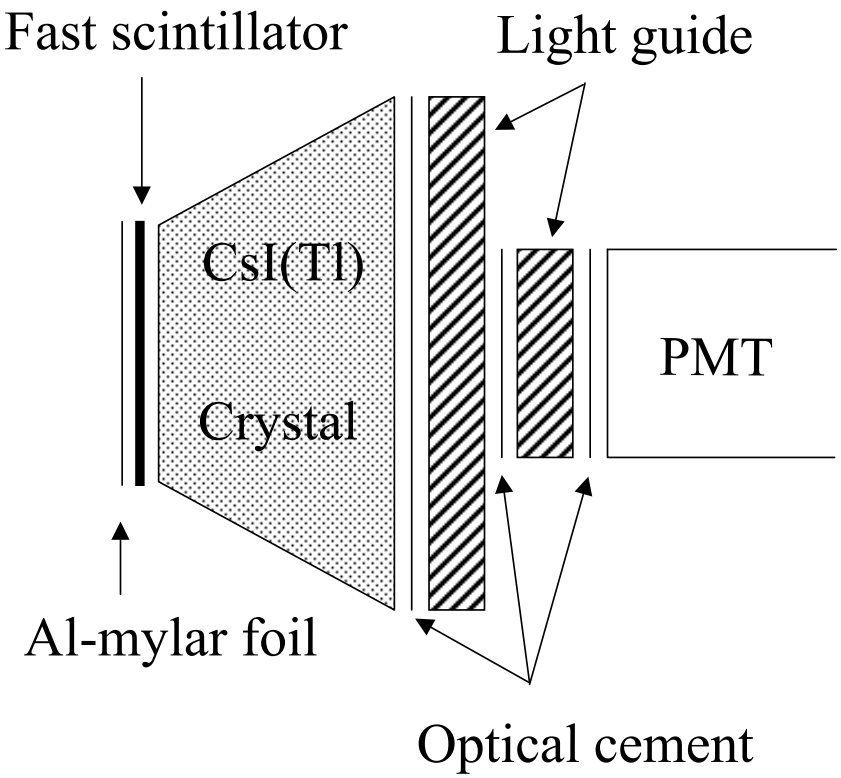

Figure 2.10: Schematic of phoswich assembly of individual detector elements.

tomultiplier. Because the light emitted by the scintillator materials have a variety of decay time constants, it is useful to analyze respectively three different components in the output signal of the photomultiplier, which we labeled: Fast, Slow and Tail. The anode signal output from the photomultiplier tube and the three integrated regions are shown in Fig. 2.11. These regions are integrated with FERA charge integrating QDCs within alternative applied gates that were triggered by the phoswich light output signals of the detectors. The Fast component corresponds to the first 33ns of the phoswich light output, which mainly originates in the thin fast-plastic scintillator. Integrating the Fast component will yield a quantity roughly proportional to energy loss δE deposited in the fast-plastic scintillator by the charged particle. The CsI(Tl) produces light that decays with a time dependence that is energy, charge and mass dependent. We obtained energy and PID information from the Slow and Tail components, corresponding to 150ns-540ns and 1.5μs-3μs after the beginning of the signal. Integrating the Slow signal gives a quantity roughly proportional to the energy E of the particle. Integrating the Tail component will yield a quantity which depends strongly on the Z and A of the particle. The integrated Fast signal and integrated Slow signal are combined to determine the charge of the detected particles with $Z \leq 18$. The integrated Slow signal and integrated Tail signal are combined to give isotopic identification for the detected particles with $Z \leq 4$. The thresholds to particle identifications are about $E_{th}/A = 2$ MeV for $Z = 3$, $E_{th}/A = 3$ MeV for $Z = 10$, and $E_{th}/A = 4$ MeV for $Z = 18$ fragments. However, these thresholds are not important to this dissertation since the Miniball/Miniwall were only used here for providing the multiplicities of light particles and IMFs.

The particle identification resolution of one of Miniball detectors, located at the polar angle of 90°, is shown in 2.12. To obtain the PID for isotopes from the Slow and Tail signals, a special transformation was done to separate the PID lines even more,

resulting a new "transformed signal", PDT [121]. A plot of counts versus Slow and Fast signals is shown in the top panel and the corresponding plot of counts versus the PDT and Slow signals is shown in the bottom panel.

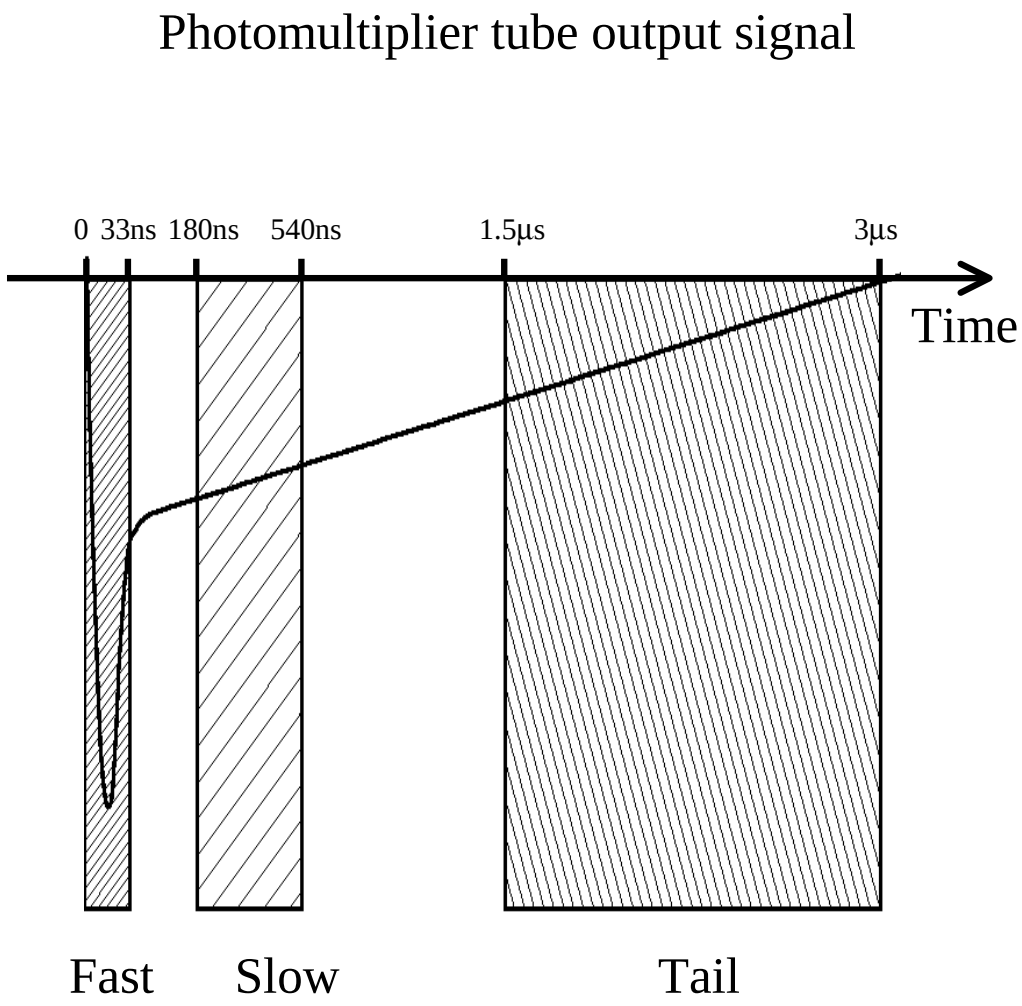

Figure 2.11: The signal from the anode of phoswich detectors. The starting and stoping times for the integrations of the three parts of the signal are shown.

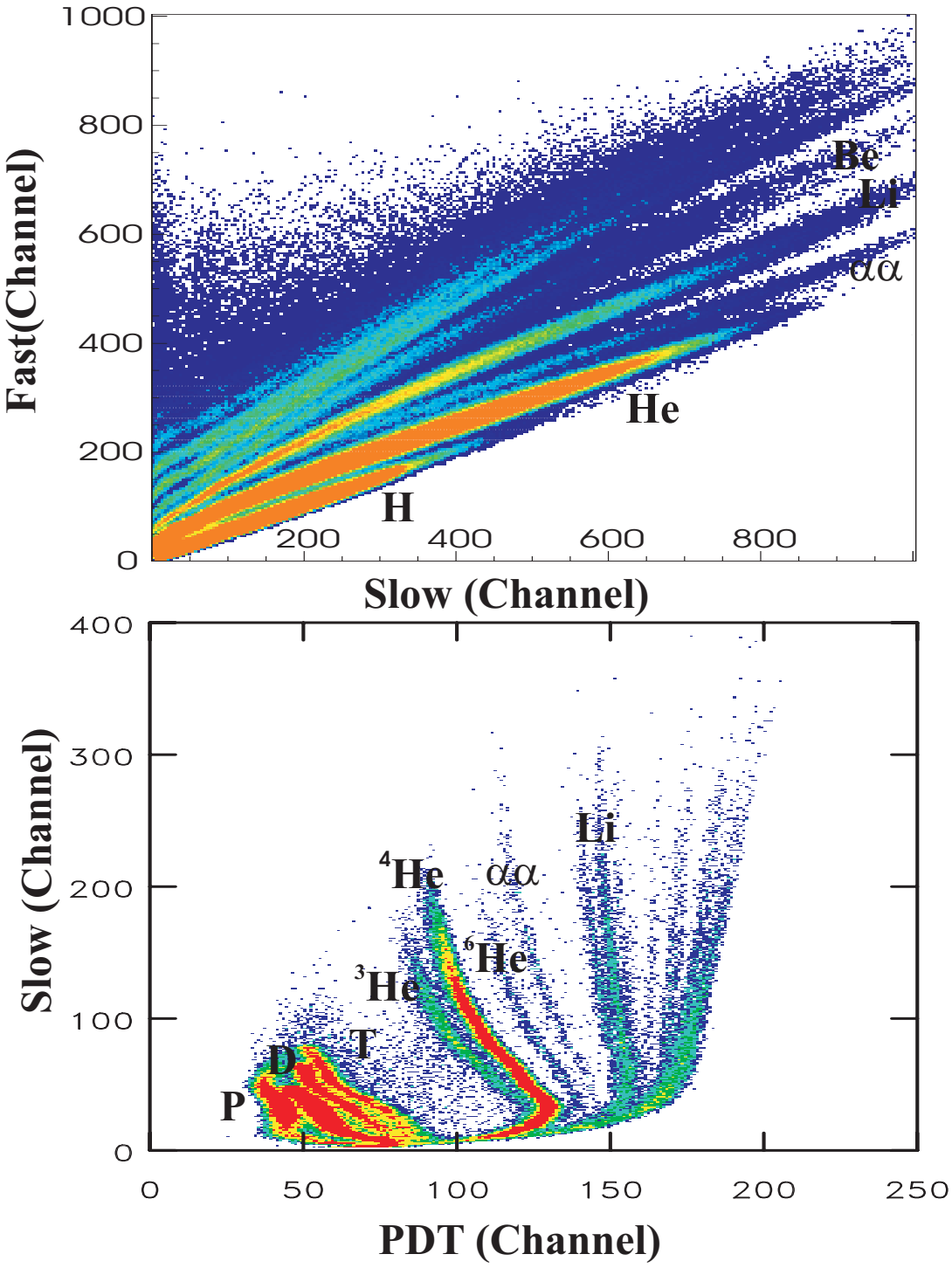

Figure 2.12: A two dimensional histograms of the raw signal from Slow vs. Fast and PDT vs. SLOW

Solid Angle Coverage

In this experiment, the Miniball/Miniwall Array is used only for impact parameter selection. A third of the Miniball/Miniwall detectors were taken out to allow insertion of in LASSA telescopes. The ring involved and the corresponding solid angle covered are list in Table 2.1. The Miniball/Miniwall detection array covered a solid angle corresponding to about 76% of 4π.

Ring	Number of Detectors	$\theta(^\circ)$	$\triangle\Omega$ (msr)	$\triangle\Omega$ of Ring (msr)
2(W)	11	6.95	2.57	28.27
3(W)	12	10	2.59	31.08
4(W)	14	13	2.85	39.9
5(W)	12	16.625	5.56	66.72
6(W)	10	21.875	10.64	106.4
3'	13	28	11.02	143.26
4	9	35.5	22.9	206.1
5	16	45	30.8	492.8
6	13	57.5	64.8	842.4
7	18	72.5	74	1332
8	16	90	113.3	1812.8
9	14	110	135.1	1891.4
10	12	130	128.3	1539.6
11	8	150	125.7	1005.6
Total	178			9538.33

Table 2.1: Table of the Miniball/Miniwall detectors used for the impact parameter selection, their corresponding polar angles and solid angle coverage.

Electronics of Miniball/Miniwall

The electronics used to read out the detectors of Miniball and Miniwall are quite similar. The electronics are divided into groups called banks. Each bank processes the outputs of 16 detectors. There are four Fast Encoding and Readout ADCs (FERAs) in each bank which processes the Fast, Slow, Tail and Time signals.

The signals from the anode of the Photomultiplier are first split by a passive splitter into four signals. One signal is used for the logic circuit and the other three

signals are the Fast, Slow and Tail parts of the photomultiplier signals to be integrated within FERAs. The four signals have relative amplitudes $I_{Fast} : I_{Slow} : I_{Tail} : I_{Trig} \approx 0.82 : 0.04 : 0.04 : 0.1$. The trigger signal is amplified and sent to a leading edge discriminator which produces an Emitter Coupled Logics (ECL) logic signal. The typical signal output from the detector and various integrating gates are shown in Fig. 2.11. Individual gates are produced by the discriminator for gating the linear gates which select the Fast region of the photomultiplier signals; while the gates for integrating the Fast, Slow and Tail regions within the FERAs are produced by gate generators that are triggered by the master trigger for each event. Since it takes some time for the logic part of the electronics to generate the logic gates, Fast signal is delayed by 150ns before the linear gate. The output of each of the linear gate is then sent directly to its FERAs.

Since there are nearly two hundred Miniball/Miniwall detectors, it would take a long time to read out the ADCs for every detector via CAMAC. Therefore, we need the FERA Fast readout scheme, which read the data through the FERA bus, with zero suppression to achieve a faster readout. The readout details can be found in the Data Acquisition Electronics section.

Fig. 2.13 shows the electronics block diagram for the Miniball array. In the figure, LP denotes Light Pulser system. It was triggered at a rate of 1 Hz to generate visible light that was injected by optical fiber into the light guide of the CsI(Tl) detectors to monitor the stability of the gain during the experiment.

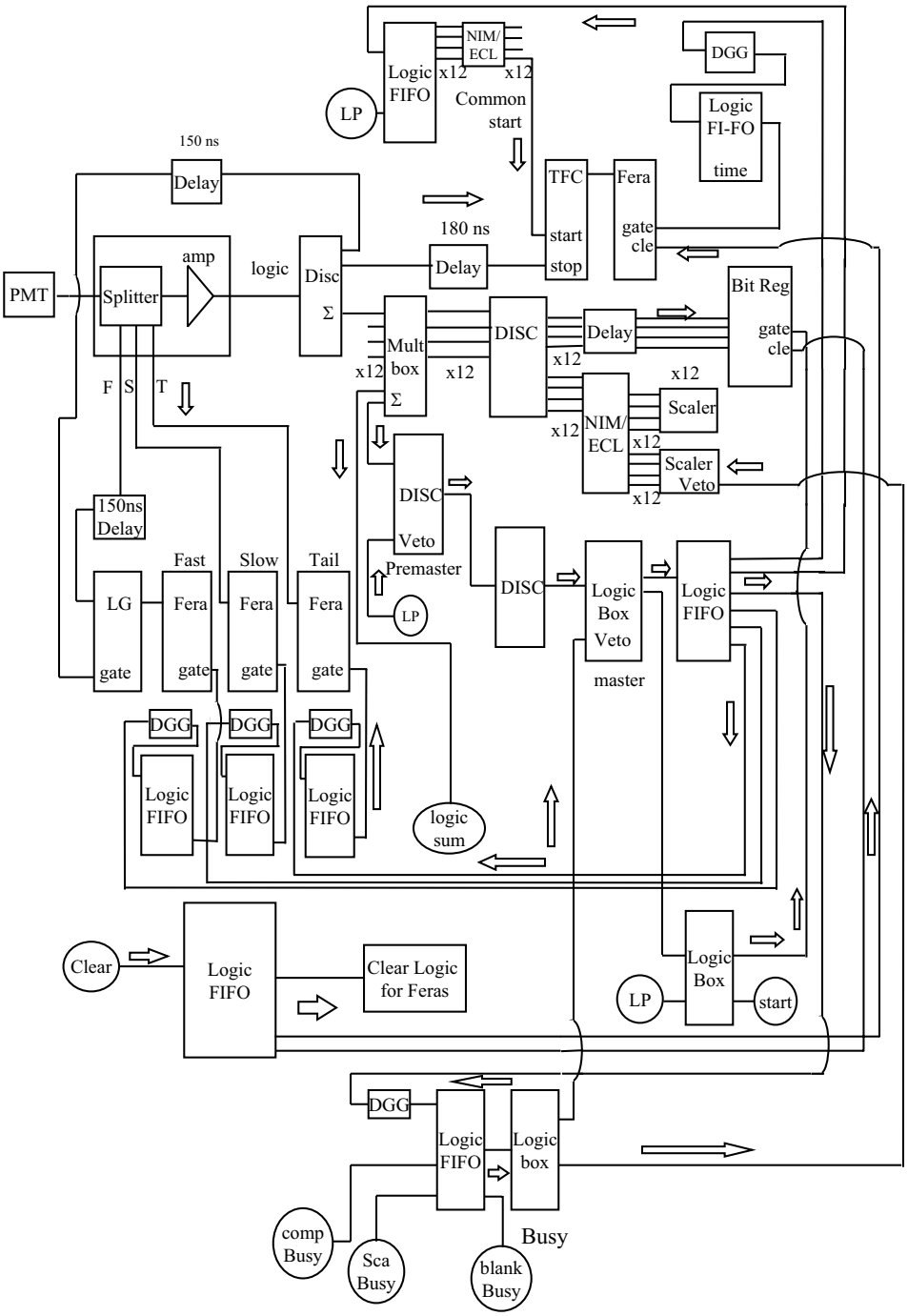

Figure 2.13: Schematic diagram of the electronics of the Miniball/Miniwall

2.4 The Ring Counter Foward Array

Structure of the Ring Counter

The Ring Counter Forward Array is an array of Silicon-CsI(Tl) telescopes. The silicon $\triangle$E detector elements are segments of a large annular strip silicon detector, the CsI(Tl) E detectors are elements of an annular array of 16 CsI(Tl) detectors. The active area of the Ring Counter is defined by the ring-shaped 280 μm(67.05 mg/cm^2) thick silicon detector which forms the first element [34]. The inner diameter of the detector is 47.88mm, while the outer diameter is 96.10mm. The front side, called the Strip side, of the silicon detector is divided into four quadrants, and each of these quadrant is subdivided into 16 strips, each at a constant polar angle. So there are total 4$\times$16 2.8mm-wide strips. The back side, called Pie side, of the Ring Counter is segmented into 16 azimuthal pie slices. The silicon detector is mounted directly on a copper plate, which serves as a cooling bar for the silicon detector. Following the silicon, there are 16, 2-cm thick, CsI(Tl) scintillators closely packed inside of a plastic ring. The 16 CsI(Tl) crystals are aligned so that each CsI crystal is directly behind one of the pie slices. Finally, a thin 5.0 mg/cm^2 Sn-Pb (60% Sn, 40% Pb) foil was placed in front of the array to absorb electrons and x-rays emitted from the target. Fig. 2.14 is a schematics drawing showing the various components of Ring Counter. Fig. 2.15 gives a side view of the Ring Counter.

Principle of Operation

The Ring Counter Foward Array identifies the charged particles using the same principles as LASSA. It uses the signal from the silicon as $\triangle$E, the signal from the CsI(crystals) as E. Ordinarily, the signal from the pie side of the silicon detector is used for $\triangle$E, and the signals from the Strip side gives the polar angle and those from the Pie side gives the anzimuthal angle. Fig. 2.16 shows the correlation between the

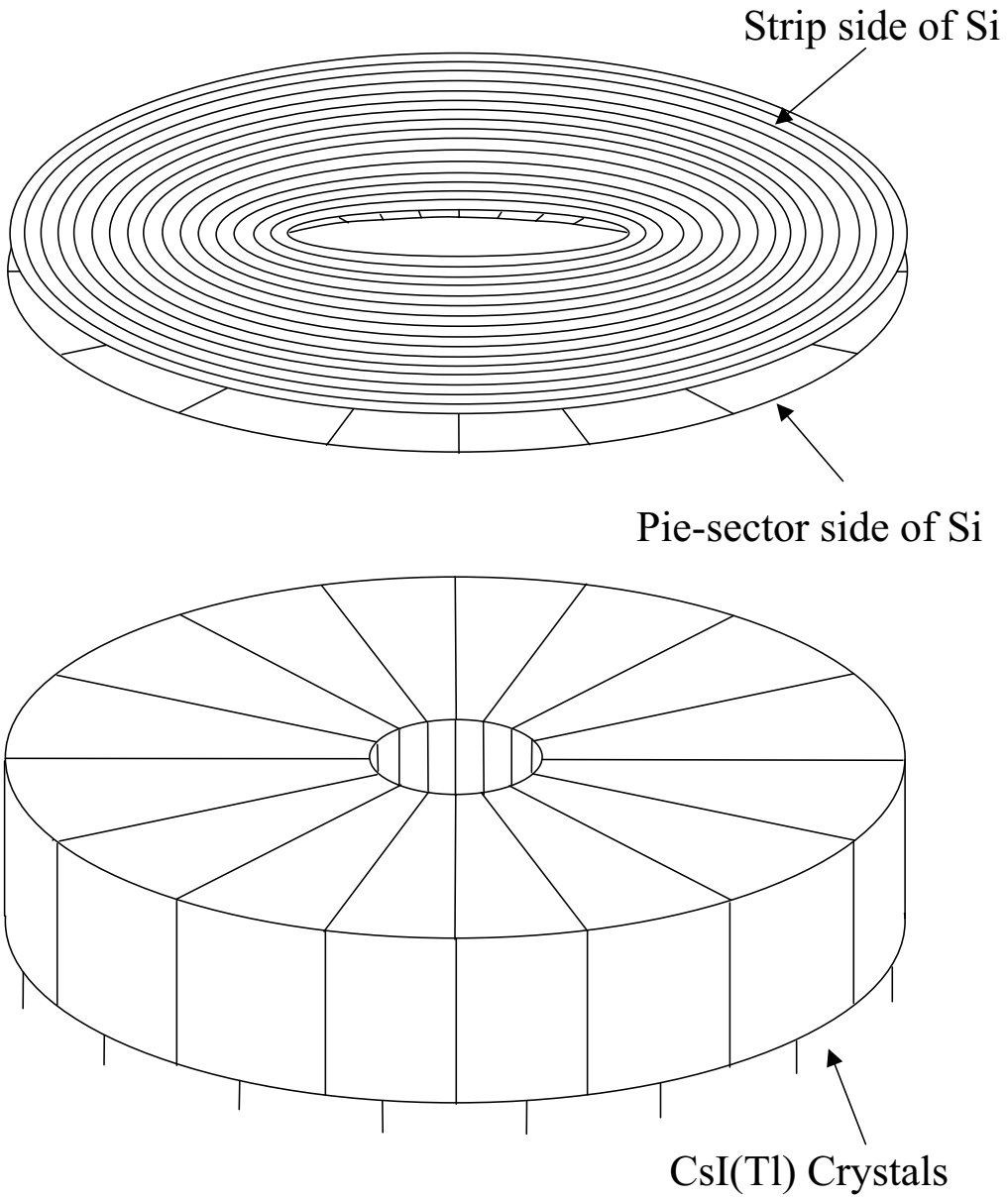

Figure 2.14: A schematic drawing of the Ring Counter

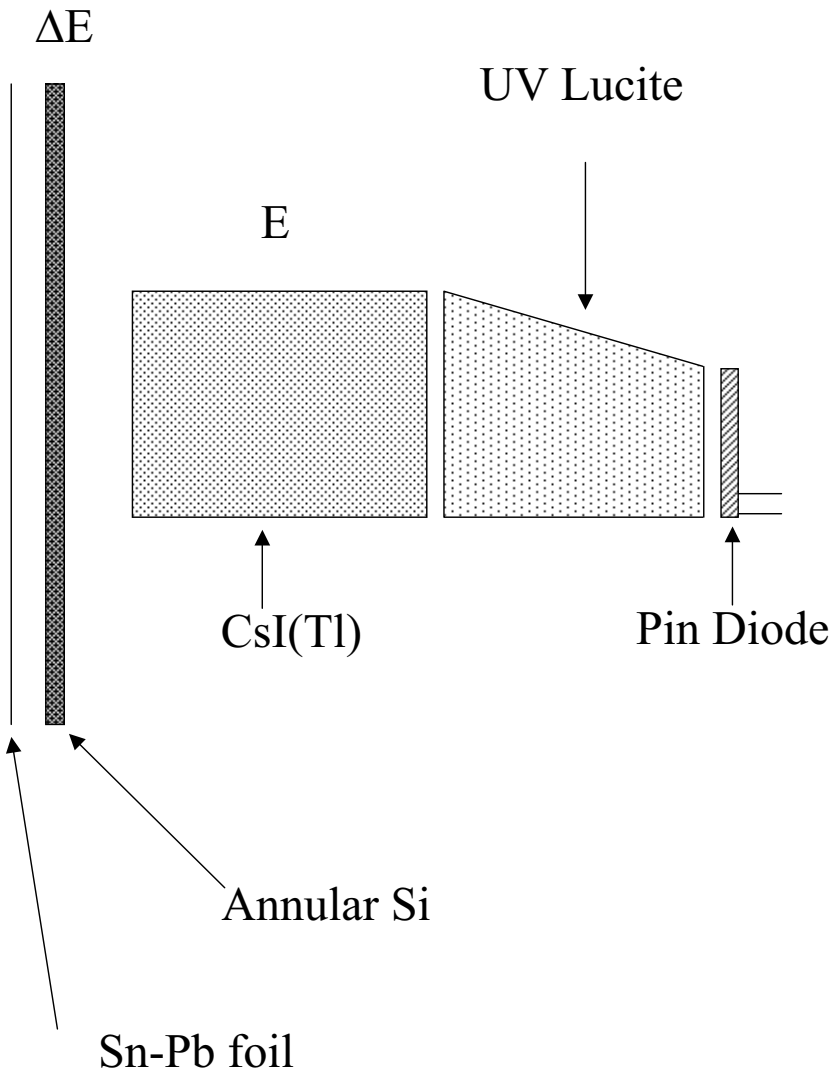

Figure 2.15: A schematic figure of the side view of Ring Counter

energy loss signals measured in the pie side of the silicon detector verses the light output signals measured in the corresponding CsI(Tl) detector.

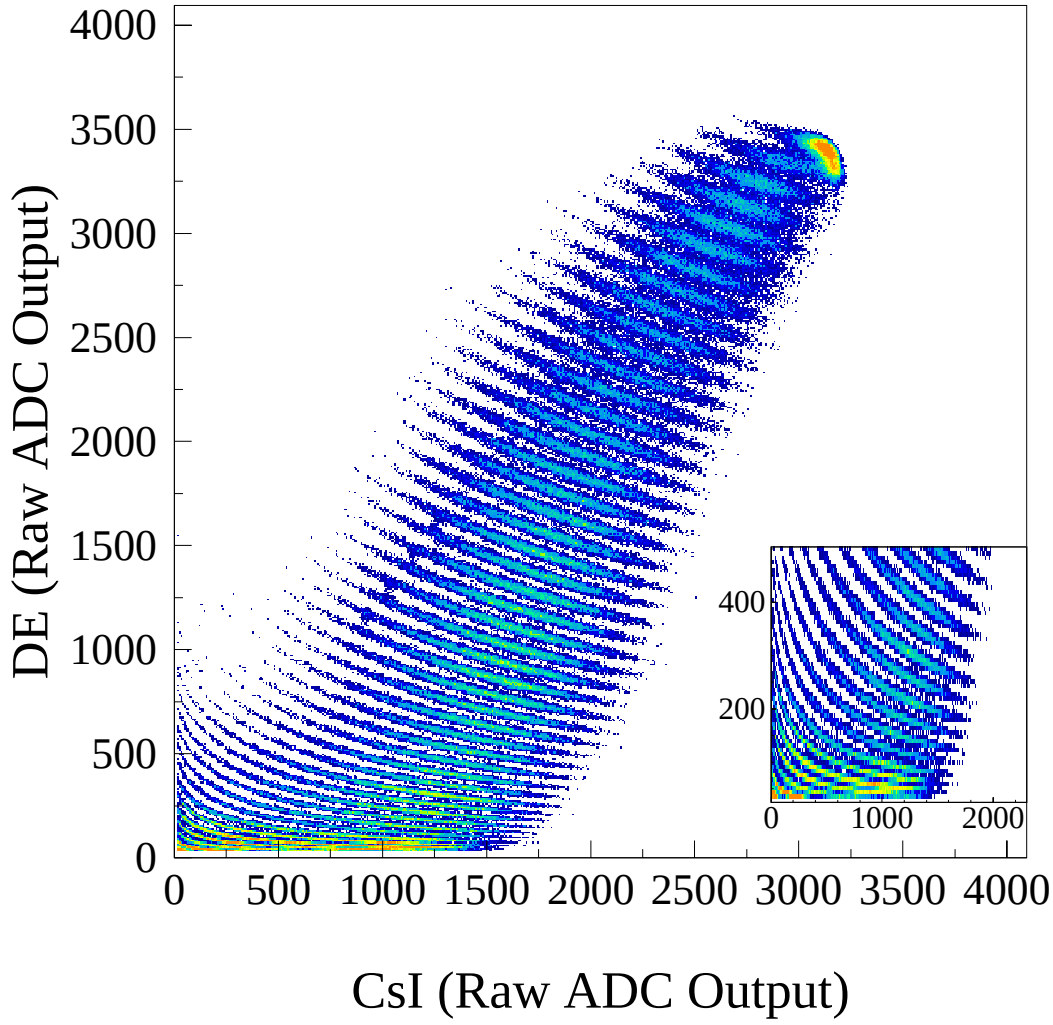

Figure 2.16: A two dimensional histogram of the raw signal from Pie side and CsI

Electronics of Ring Counter

The pie side is the p-type side and the strip side is the n-type side. The diode detector is reversely biased. Each strip or pie slice is read out independently. Similar electronics were used to process the signals from the Ring Counter Forward Array as

for the LASSA telescopes. Lower gain LBL preamplifiers were used for Ring Counter silicon signals, however, because the energy loss of the projectile-like fragments is very large.

A schematic of the electronics is found in Fig. 2.17. The electronics used to read out the 16 channels of the azimuthal pie-slice segments and the 64 channels of the polar-angle strips are similar, the only differences are the polarity of the signals and the additional requirement that the pie sector provides the timing information. Although the preamplifiers of the signals from the 16 azimuthal pie sectors generate both a Fast and a Slow outputs, we injected the Slow output into a Washington University (WU) shaper-discriminator module, which contains a second stage slow-shaping amplifier and a fast timing-filter amplifier. The fast timing-filter amplifier output was used as the trigger to the experiment. The outputs of the fast amplifiers of the 64 polar-arc segments and the 16 CsI were amplified in a second stage slow-shaping amplifier in a single-width WU shaper. All the outputs from the slow-shaping amplifiers for the strips, Pie's and CsI's were sent to the Phillips 7164H 4096 channel peak-sensing ADCs. Only those signals above the low-threshold of the peak-sensing ADC were digitized and read by the DAQ.

2.5 Data Acquisition Electronics

The Data Acquisition (DAQ) for this experiment was a big challenge. Strip-silicon detectors usually require a lot of electronics. In this experiment, there are 9×16 DE signals, 9×16 EF signals, 9×16 EB signals, 64 Strip signals, 16 Pie signals, for a total of 512 energy signals from the strip detectors. In addition, there were 36 energy signals from the CsI(Tl) detectors as well as 144 timing signals from the EB strips. We also need to incorporate Fast, Slow, Tail and Time signals from the roughly 200 Miniball/Miniwall phoswich detectors, which corresponds to 800 electron channels.

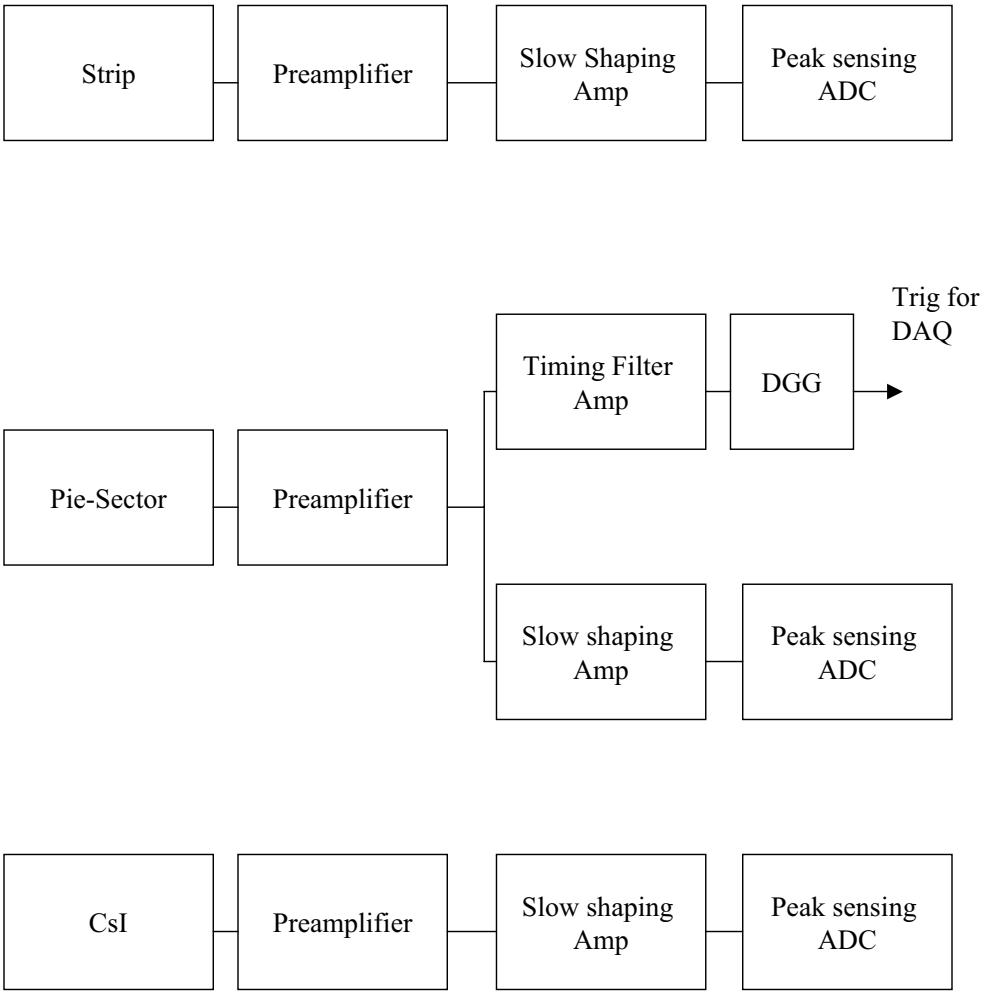

Figure 2.17: A block chart of the electronics of the Ring Counter

To reduce the dead time and incorporate LASSA and the Ring Counter electronics as well as Miniball/Miniwall electronics, all channels were read out via the FERA ECL readout scheme. The Miniball/Miniwall electronics used FERA 4300 ADCs which could be read out more quickly via the ECL (Emitter Coupled Logic) port. This is a double-bus readout scheme, with one bus for command and another for ECL port data. A rate of up to 100nsec/word can be reached, comparing with the typical CAMAC hardware cycle of 1 μs. To make use of the ECL port readout, there are some problems needed to be solved: First, Phillips ADC does not have an ECL readout port like FERA. To solve this, an auxiliary CAMAC module, called SS32 is used. This CAMAC module is designed by J. Toke of University of Rochester. SS32 works as a inter-media between Phillips ADC and Lecroy FERA Driver 4301. It acts like a very fast CAMAC controller to the Phillips ADC, and outputs the data via the ECL port like a standard Lecroy 4300 FERA. All the data from the FERAs and SS32 were sent via the ECL port to a FERA Driver 4301.

In more detail, the SS32 collects the data from Phillips ADC, handshakes with FERA driver 4301, then puts the data to the data bus. Every converter executed a hit-pattern-based sparse readout of up to 24 Phillips model 7164 ADCs via the standard CAMAC protocol. This non-standard readout effectively moves the data and control cords from the back plane of the CAMAC crate, to the front, ECL ports of the SS32. The non-standard readout, which required no hardware modifications to the 7164H ADCs, or the CAMAC crates, resulted in a 7.5-fold reduction in the readout time of the LASSA electronics as compared to a standard CAMAC readout.

The old Miniball electronic design is tree-structured; one problem that needed to be solved is that FERAs were not side by side as needed for a bus-structured readout. Special cables and connectors are made to solve this problem. A schematic drawing of the topology of the electronicsis shown in Fig. 2.18. The readout for the Miniwall

was analogous to the Miniball and the readout for the Ring Counter was analogous to the LASSA, so the readout for the Miniwall and the Ring Counter were not shown in this figure. In Fig. 2.18, the readout has a two-level scheme. The lower level is the FERA modules and SS32 modules which are controlled by FERA drivers; the FERA drivers, in turn, are controlled by a VME module Fera Faucet Maier (FFM).

In Fig. 2.18, those rectangles with thick black box lines are the CAMAC crates. Those lines connecting the modules in the CAMAC crates denote the bus lines for control signals and data. The signals from the Miniball detectors come from the upper-right corner and go directly to the splitter. The trigger signals from the splitter go through the discriminator and the multi-box to the main trigger control module OCF 8000. The outputs from OCF 8000 are sent to FFM, different ADC and TFC modules. The multi-box is used to determine the coincidence multiplicity of Miniball trigger, which we set to 3 in this experiment. The Fast, Slow and Tail signals from the splitter are sent directly to the corresponding FERAs in the CAMAC crates. The signals from the LASSA are from the left side of Fig. 2.18. They first go to a double-width WU shaper and discriminator/TFC module. The outputs of WU shaper are sent to the Phillips ADCs while the outputs of TFCs are sent to FERAs for timing signals. The data in those Phillips ADCs are collected and sent to FERA drivers by SS32.

The principle of ECL port readout can be understood from Fig. 2.19. For the same reason as Fig. 2.18, only the parts for LASSA and the Miniball are shown. Fig. 2.19, one sees a microprocessor, the "transputer", developed by Inmos company, was used as the front-end computer. CES High Speed Memory (HSM) 8170 is a standard VME memory module. FFM integrates the CES 8170, FERA drivers and ECL readout modules. The usual trigger used for this experiment was the observation of a multiplicity in the Miniball/Miniwall > 3 or with the Ring Counter trigger,

downscaled by a factor of 25. Zero compression is used for all ADCs to suppress all data words which are consistent with the experimental pedestal in the individual ADC channels.

In upper part of Fig. 2.19, one can see that the electronics for the Miniball array are basically the same as what is shown in Sec. 2.3. The main difference is in the lower part, where one sees that the output signals from delay gate generator (DGG) are sent to the gate input (GAI) of FERA driver, instead of the gate input of FERA. The LASSA elctronics, as described in Sec. 2.2 are incorporated with the Miniball electronics. Also, the busy outputs from CES 8170 and FFM are added to the busy logic boxes.

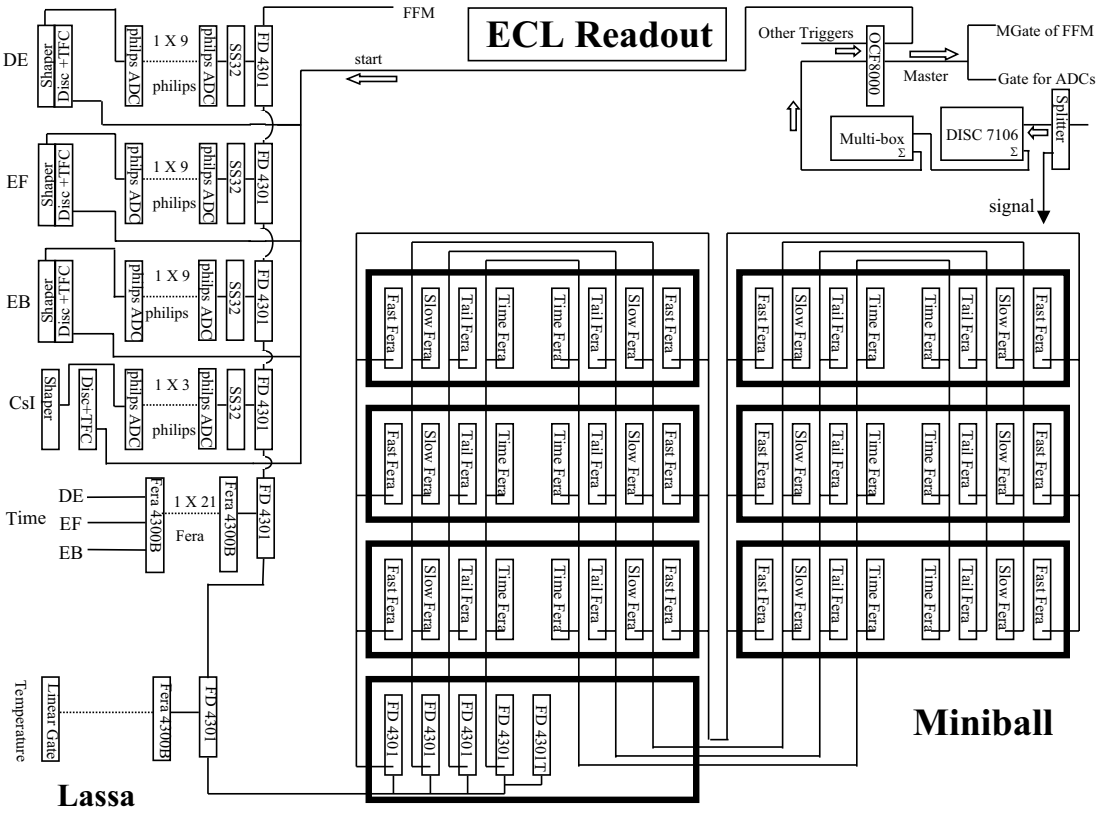

Figure 2.18: Layout of the data acquisition (FD means FERA Driver)

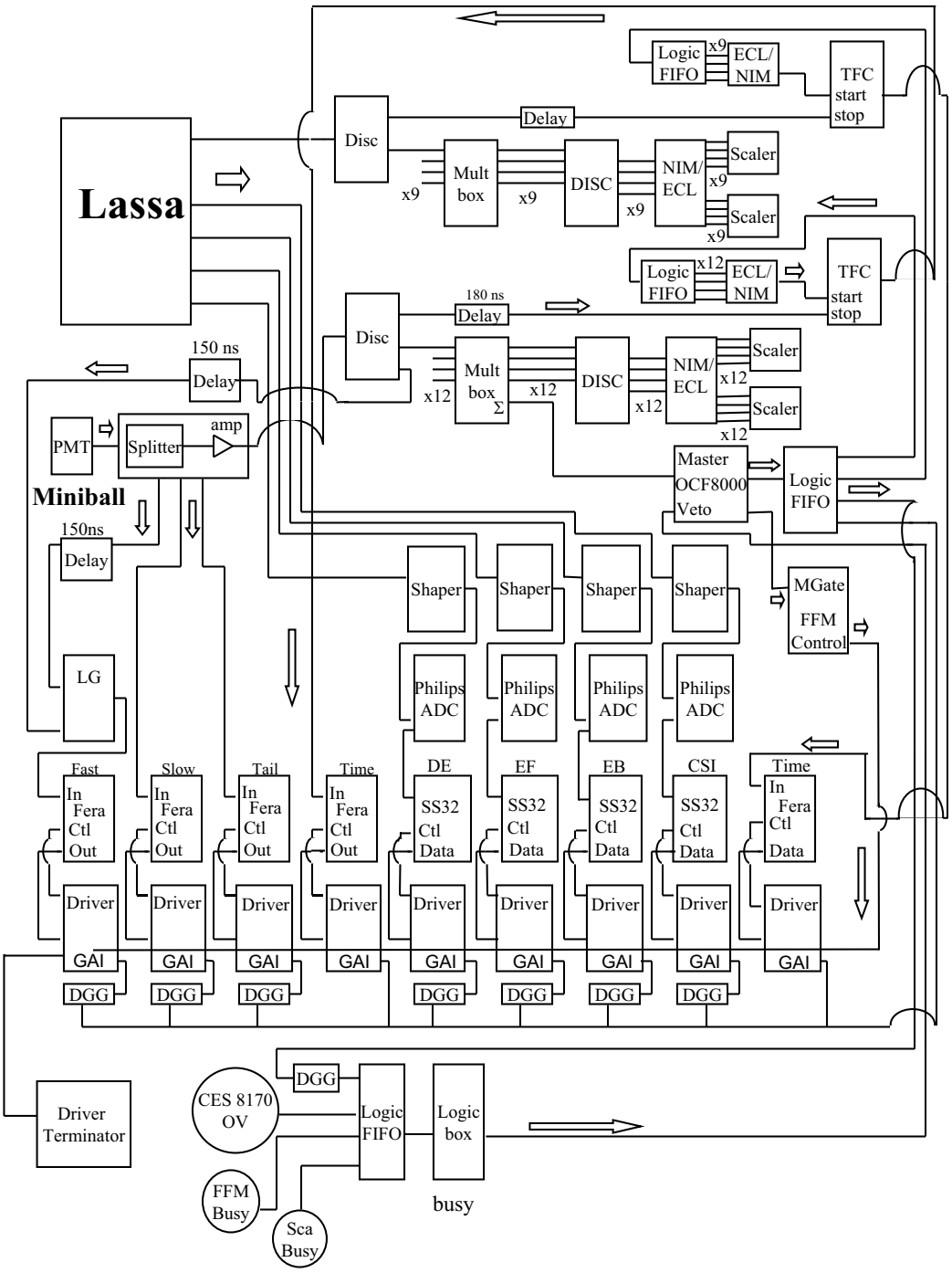

Figure 2.19: Schematic drawing of the principle of the ECL readouts

Chapter 3

Data Analysis

3.1 Data Reduction Algorithms

As discussed in the last chapter, three types of devices were involved in the experiment: LASSA, Ring Counter and Miniball/Miniwall detectors. Miniball/Miniwall detectors are only used for impact parameter selection, so the energy calibration was not done for Miniball/Miniwall detectors. However, a rough PID function was generated to separate LPs (light charged-particles with $Z < 3$) and IMFs (heavier fragments with $Z \geq 3$). For LASSA, the calibration was done for isotopically resolved particles. For the Ring Counter, the calibration was done for atomically resolved particles.

Since both LASSA and Ring Counter are composed of silicon-strip/CsI telescopes array, the data analysis for these two devices are quite similar. This data analysis is basically divided into two parts. One consists of the analysis of the signals in the Silicon detectors while the other one is the corresponding analysis for the signals in the CsI detector. For the Silicon detector part, the most difficult issue is the multiple hit correction. In multiple hit events, two or more particles hit the same telescope at the same time. When a multiple hit happens, there will be more than one way to pair up the signals from the vertical and the horizontal strips, the task is to determine the

correct pairing. For the CsI detector part, the main issue is the energy calibration. Since the lightput out of CsI(Tl) depends on the mass number A, atomic number Z and energy of the charged particles, different calibrations must be done for each isotope (LASSA) or each element (Ring Counter). We will talk about details of the data analysis of LASSA and the Ring Counter in the following sections.

3.2 Data Analysis of LASSA

3.2.1 Overview

The energy calibration and the generation of the PID function were the first two steps of analysis for the data analysis of the LASSA telescopes.

The LASSA array was calibrated in three stages. The first stage involved calibration of the device in the running configuration with a precision pulser and a charge terminator. In the second stage, a series of fragmentation beams was used and each detector was repositioned to allow the beam to be put directly into the telescope. Beams of 20 MeV/u ^{16}O and 40 MeV/u ^{36}Ar were accelerated by the K1200 cyclotron at Michigan State University and used to bombard a production target at the exit of the cyclotron. Reaction products from projectile fragmentation were subsequently selected according to magnetic rigidity by the A1200 magnetic channel. These low intensity secondary beams ($\sim$1300 p/s) were then used to directly scan the detector face. The beams used are listed in Sec. 3.2.5. These beams were useful in assessing the thickness non-uniformity of the 65 μm Si detector, as well as in calibrating both of the Si detectors and the CsI(Tl) detector. Finally, proton recoils used for proton calibration was measured by bombarding a Polyethylene target (CH_2) with a ^{112}Sn beam.

Two sets of PID functions were generated for LASSA: A Si-Si PID function is

generated for particles stopping in the second silicon detector, a Si-CsI PID function is generated for particles stopping in the CsI. To generate added 2D PID histograms without losing resolution, one needs to do the correction for the thickness non-uniformity of silicon detectors as well as the gain-matching of the CsI detectors. The thickness non-uniformity correction is done for each "pixel" defined by the intersection of a given front and back strip in the 500μm detector. In order to properly assign particles to their respective pixel, a multiple-hit decoding routine is needed to determine which pixel the charged-particle hit. This routine will also give the positions and energies for each particle when more than one particle hit the same detector at the same time.

After the energy calibration is done and the PID functions are generated, the full information for each charged particles detected by LASSA telescopes can be obtained and written to a "physics tape". This information includes: the Particle ID, the total kinetic energy and the emission angle.

In order to obtain the final yields and energy spectra, background from noise and random coincidence should be subtracted. The LASSA array also has a limited solid angle coverage. Thus, the detection efficiency should be calculated and corrections for the efficiency should be made. The final yields are then obtained by applying various cuts to these efficiency corrected data.

Fig. 3.1 gives an overview of the scheme of data reduction of LASSA. It also shows the sequence following which the analysis is done. We will discuss the data analysis details according to this sequence.

3.2.2 Energy Calibration of Si

For the range of charged particles we analyze here, the signal generated depends linearly on the energy deposited by the charged particle, independent of the type of

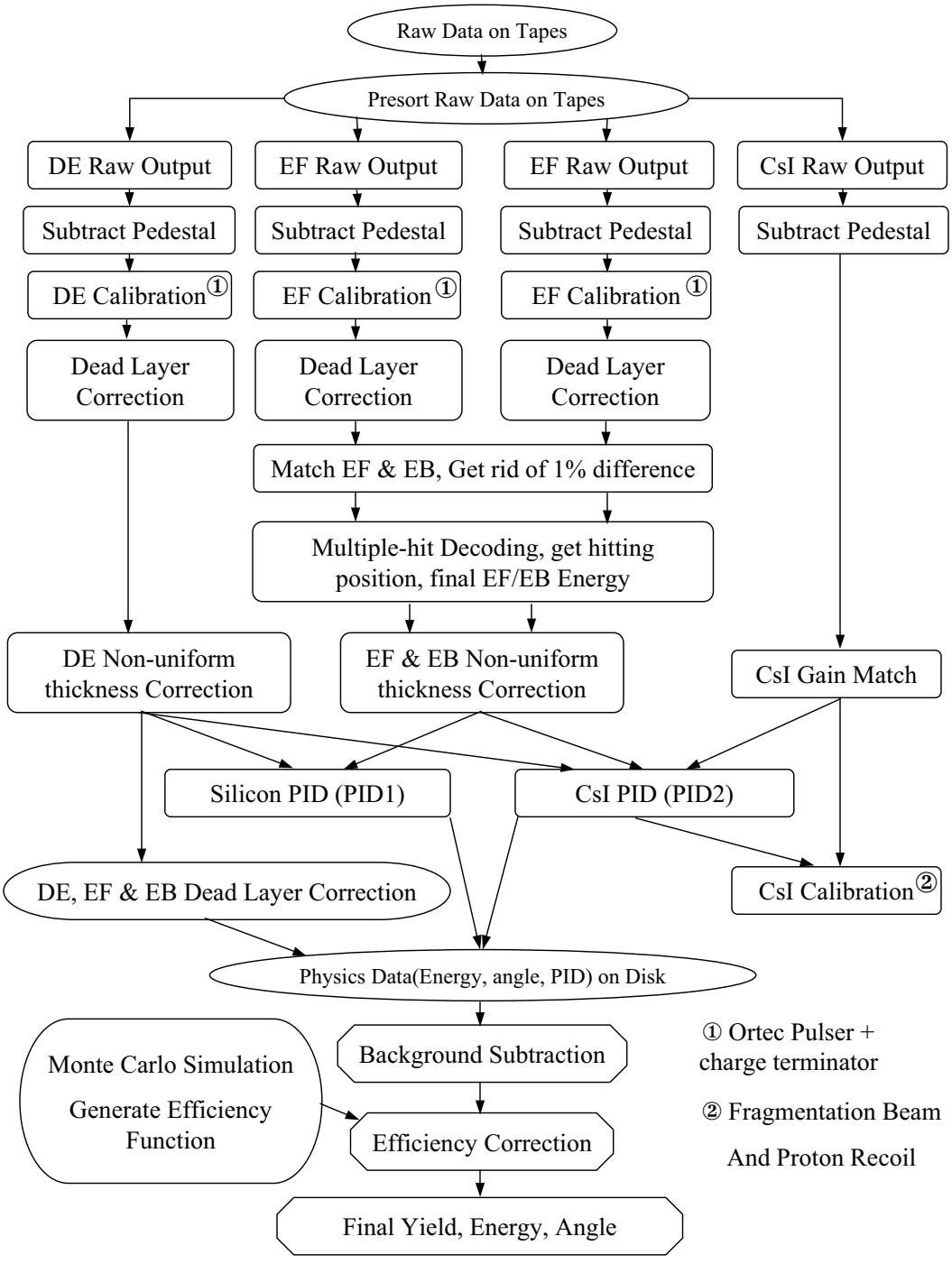

Figure 3.1: Major detectors used in the experiment, viewing in the downstream direction of the beam

the charged particle detected. Indeed, we expect an electron-hole pair to be collected from the detector for each 3.1 eV of energy deposited. Based on these facts, we can simply calibrate the energies of particles detected in the silicon. Specifically, we cross-calibrate a pulser system by α source detected in the silicon detector at low energy. Then we extrapolate the calibration to the whole energy range of Silicon with a linear pulser system. This pulser system consists of two parts: an Ortec precision pulser generator and a precision capacitor that is placed between the pulser and the cable that connects the detector to is preamplifier. The Ortec precision pulser generates precise pulser signals, with amplitude that is linearly dependent on its dial setting. As the input to the preamp is a "virtual ground", the capacitor value sets the scale of the injected charge.

In our experiment, we used the following:

1) A PC based data acquisition system was used to calibrate pulser system relative to known energies of ^{228}Th and ^{241}Am α sources. Fig. 3.2 is a schematic drawing of this PC-DAQ set. The energy of the α particles from these α sources are relatively

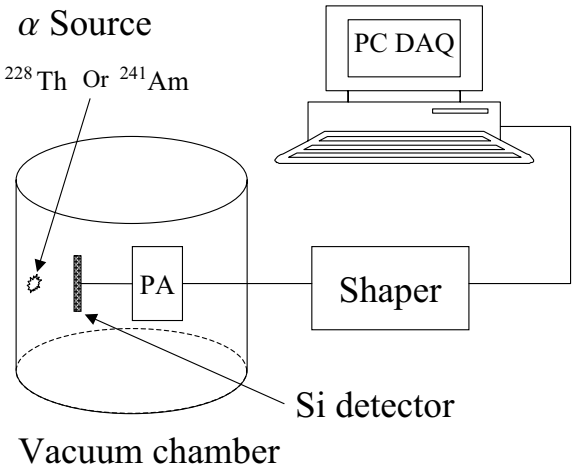

Figure 3.2: The PC-DAQ system used for the silicon calibration

low, comparing with the energy range of particles detected in the experiment. To

calibrate the pulser dial setting, we set the amplifier gain to put 8.784 MeV into Channel 2220 of a 4k channel ADC. Then, we measured the pulse height spectrum for the pulser for a variety of dial settings on the pulser.

2) This relation between the ADC spectrum and the pulser dial setting can be expressed as:

$$ADC\ readout = a \times (Dial + b_1) + b_0 \tag{3.1}$$

where, a is a pulser attenuation factor, b_0 is the channel number corresponding to zero pulser height from the pulser, b_1 is a constant describes how the zero may change with pulser setting.

3) Using 1) and 2) and several attenuation and dial settings we obtained the relationship: Energy vs. Dial. Since the gain settings for DE, EF and EB are different, calibration using different attenuation factors were needed when the dynamic energy ranges for various detectors differ. Three different dynamic ranges for the pulser calibration, 140MeV, 200MeV and 500MeV, were used to calibrate the DE, EB and EF signals. Fig. 3.3 shows the relationship between the Dial and the Energy for the DE, EF and EB pulser calibrations.

4) At the end of the experiment, we coupled the pulser capacitor to the cable between the Silicon and Preamplifier by using a T-connector. Everything including detectors and DAQ were maintained under the same conditions as during the experiment.

5) Then we changed the dial of the pulser, to get a relationship: Energy vs. the channel in the ADC, used in experiment, until the full response over the full energy range of the detector is obtained. This full energy range depends on the gain settings of preamplifier and shaper. Normally, the linearity is good for energies in the middle of the energy range, but gets worse at low energies, when the ADC output is close to zero channel or at high energies where the amplifier become non-linear. To address

this effect, more calibration points are done for ADC output below 100 and above 2500 channel in the 4095 channel Phillips ADC. Then we fitted the calibration with a linear function for ADC output channels 0∼100, a second linear function for ADC output channels of 100∼2500, and a polynomial of order 4 for ADC output channels of 2500∼4095. Between those fitting functions, a spline interpolation is used to make a smooth connection. Fig. 3.4 shows the calibration line for a typical Silicon strip.

Step 4) and 5) of this procedure was repeated for all 432 strips of ΔE, EF and EB one by one. After the calibration is done, the calibration is checked by plotting the energy of EF vs. EB. If the energy calibration is correct, with no noise, the energy from EF and EB should be exactly the same for each particle. However, we had about a 1% difference in the energy between EF and EB after our calibration. The reason for this is not clear. Possible reasons are: a difference in the efficiency of charge collection between EF and EB or an systematic error in the attenuation setting of the Ortec pulser. To correct for the discrepancy, we forced the energy from

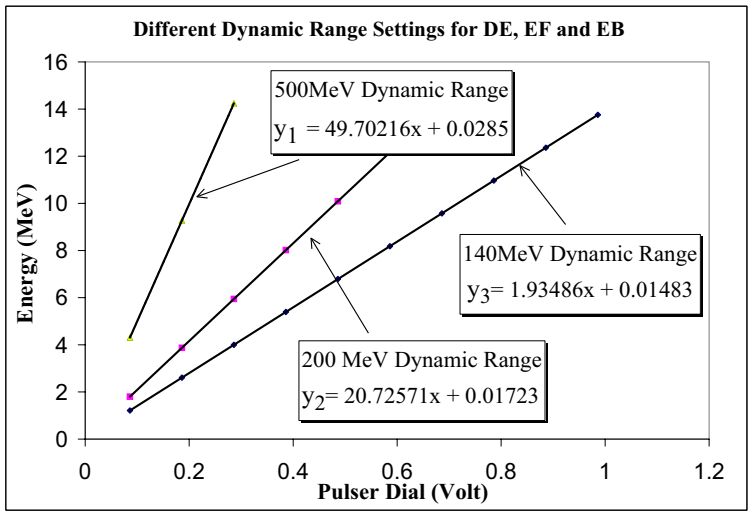

Figure 3.3: Calibration lines of energy(MeV) vs. Dial value(Volt)

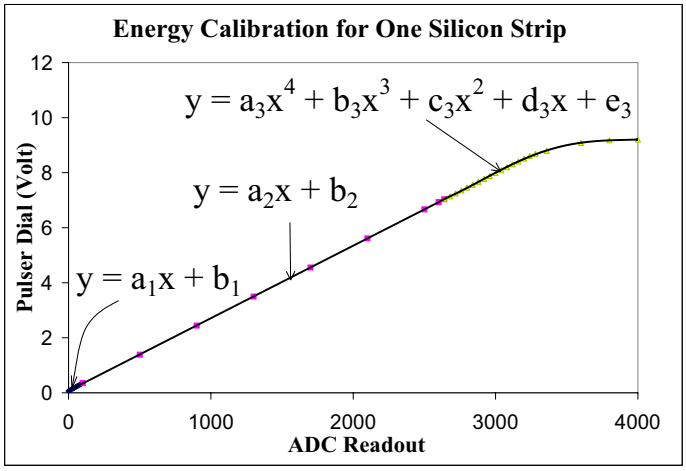

Figure 3.4: ADC output vs. precise pulser dial value(Volt)

the EF channels to be equal to the energy from EB channels, which we took to be more accurately matched to the α calibration points.

3.2.3 Multiple-hit pattern Decoding

Before one can get the PID function, some preparations need to be done. Most important preparations are the Pixelation (Multiple-hit Decoding) and Non-uniform Thickness Correction. In LASSA, strips of EF and strips of EB are perpendicular to each other. The scattering angle of particle is determined from the X, Y coordinates where the particle hits the telescope. Here, X and Y are basically determined by which EF and EB strip is fired. (We use X to denote position information obtained from EF and Y to denote position information obtained from EB.)

When only one particle hit the telescope, one can easily tell X and Y values from the energies detected in the strips. However, when two or more particles hit the telescope at the same time, several EF and EB strips will have data. For example, when two particles hit one telescope at the same time, there will usually be four

signals X_1, X_2, Y_1, Y_2. Sometimes, there would be fewer if one of the strips in the detector is not working properly or the two particles happen to hit the same strip. If four signals are observed, one need to know whether the two particles hit (X_1, Y_1) and (X_2, Y_2), or in coordinates (X_1, Y_2) and (X_2, Y_1) instead. One needs also to know the amplitude of the signals (corresponding to energy loss) induced by these two particles. Most of the times, the position and energy information can be retrieved by requiring the signals from EF and EB to be equal. But sometimes, this comparison does not yield a unique answer. For example, if the signals (energy loss) induced by the two particles happen to be the same then both parings (X_1, Y_1) and (X_2, Y_2), or (X_1, Y_2) and (X_2, Y_1) are equally favored. However, when the signals from $\triangle$E and CsI are included in the paring, it is often possible to determine which paring is the correct one. Thus in practice, various hitting patterns must be tested to find the most probable one.

Occasionally, more than two particles hit the telescope at one time. We have not found a reliable algorithm to analyze such events. Instead we reject them and count them as lost.

When there are bad strips in a telescope and particles hit these strips, the reconstruction fails and the information from that particle can not be retrieved. When either position or energy information for a particle are irretrievable in a strip detector, this particle is also lost. Other losses occur: when two or more particle go into the same CsI crystal, then, the energy information is lost because the signals induced by multiple particles superimpose on each other in the CsI and cannot be separated. Also, particles are lost when they hit at the gaps between the CsI, and no valid signals for CsI can be constructed.

Another output of the Multiple-hit decoding program is a record of the fraction of particles which are lost. This information is then used to constrain the efficiency

correction. More details about efficiency correction can be found in Sec. 3.2.7.

3.2.4 Construction of PID function and Non-uniform Thickness Correction

When constructing the PID function, it is desirable to make it applicable to all two dimensional (2D) $\triangle$E vs. E histograms. However, when one does this, the isotopic resolution of the 2D spectra becomes rather poor. This occurs, because the measured values for $\triangle$E and E depends on the position where the particle hits the telescope. Part of this position dependence comes from the thickness variation of the silicon detector across its surface. For $\triangle$E, the thickness variation is of the order of 10 μm, causing a position dependent variation in the energy loss of the particles and smearing the relationship between $\triangle$E and E values. Only if the thickness variation is of the order of 1%, can one calculate the PID without addressing this position dependence. Second, when the 2D PID histogram is constructed by using silicon as $\triangle$E vs. CsI, it is easiest to use the uncalibrated output of the CsI detector. However, the uncalibrated output from the CsI depends on the gain setting of the electronics, so this signal will be crystal related.

To obtain a PID function that is applicable to all telescopes without losing resolution, we should correct for these effects. For the silicon detector, we assumed that the energy loss a particle experiences in passing through the detector is proportional to the detector thickness, which is good for relatively small energy losses. Then we determined the relative thickness of different $\triangle$E by using particles of fixed energy and measuring the energy losses in the silicon. This can be done if you have a beam of defined energy or if you measure particles that stop in the second silicon. In the latter case, you can gate on the total energy deposited in the silicon. Such gates applied to α particles were quite important for establishing the variation of $\triangle$E thickness with

position.

In general, the thickness correction is done for each "pixel", defined by the intersection of a given front and back strip in the 500 μm detector. In this fashion, we obtained thickness corrections for both the 65μm silicon detector and the 500μm silicon detectors. (Note, the non-uniformity is less crucial for the 500μm silicon detector, which is of the order of 1%). After the non-uniform thickness correction, we define an effective "energy" so that particles with a given energy have the same "effective" energy loss in the silicon detector regardless where it hits. Then we applied the PID function to all telescopes.

The effect of making this non-uniform thickness correction is shown in Fig. 3.5. On the Left panel of Fig. 3.5, the PID of Lithium and Carbon isotopes are obtained without making the thickness correction. One can see that the resolution is bad. On the right hand panel, the thickness correction is performed. A much better resolution is achieved. A comparison of the left panel and right panel of Fig. 3.5 illustrates the crucial importance of correcting for the thickness variation in the 65 μm detector in achieving optimal particle identification. Details of the construction of the 1D PID function will be discussed later in this section.

For the CsI detector, the gain match is done by matching 36 CsI crystals of LASSA to one selected crystal, using Helium and Carbon calibration points from a beam calibration run.

After the silicon detector calibrations, the non-uniform thickness correction for the silicon detector and the gain matching of the CsI crystals. 2D $\triangle$E vs. E PID histograms were constructed. These PID histograms are now independent of the position where the particles hit the detectors. In practice, different measured quantities were used for $\triangle$E and E in order to construct the more accurate PID functions. For example, the DE detector is used as $\triangle$E and the value of EF is used as E for particles

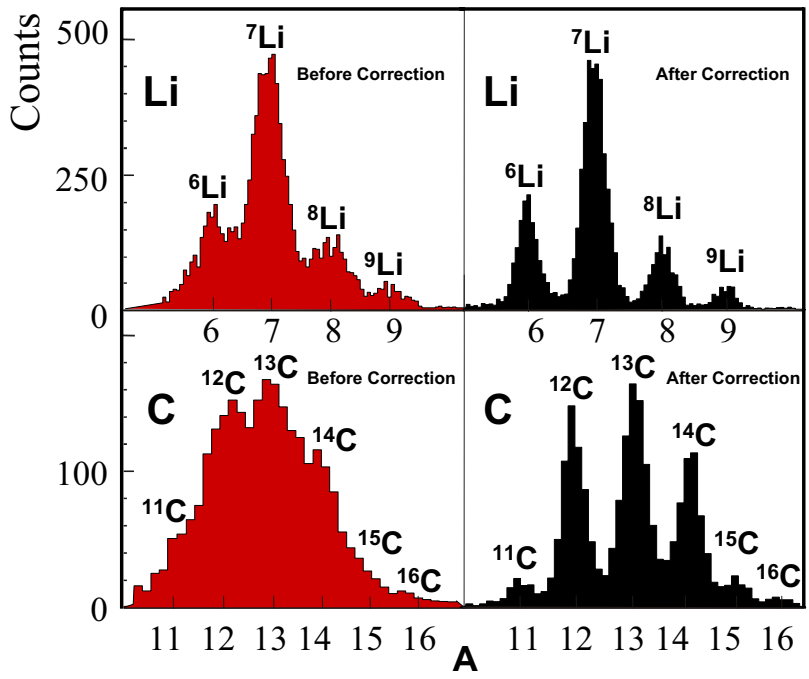

Figure 3.5: Comparison of isotope resolution before and after thickness correction

that stopped in the second silicon. The low EF gain allowed higher Z fragments to be properly identified. For p, d, t, ^{3}He, ^{4}He and ^{6}He that stopped in the CsI crystals, EB is used as $\triangle$E and the matched raw output from CsI is used as E. The EB signals, which used higher gain shaping amplifiers, improved the identification of the isotopes of Hydrogen and Helium at the expense of dynamic range. The identification of higher Z fragments required the use of the lower gain EF signal. For isotopes with $Z > 3$ that stopped in the CsI crystals, DE+EF is used as $\triangle$E and the matched raw output from CsI is used as E. A typical DE-EF two-dimensional spectrum for a telescope is shown in Fig. 3.6. In this figure, the measured energies in DE and EF detectors are matched first, which we call them nominal energies, and then are used to construct the 2D histogram. PID gates are drawn from this histogram. Compared with the raw energy spectra shown in Fig. 2.6 in the previous chapter, CsI signals

are used to veto the punch through lines. A typical DE+EF-E(CsI) two-dimensional spectrum for a telescope is shown in Fig. 3.7. The isotopes of oxygen can be clearly distinguished in this figure. PID gates are drawn from this histogram too.

The 2D PID histogram is not convenient. To make various gates for different isotopes as well as to estimate the background level, it is desirable to work on a 1D histogram. One cannot simply project the 2D histogram to either X or Y since the PID lines are curved in the 2D histogram. However, one can straighten the 2D PID histogram by drawing curved line along each isotope and projecting the 2D histogram according to these lines. Because the real isotope yields are not symmetric about these lines, this projection can cause some problems in the normalization, making it difficult to fit the curve of isotopic yield.

Fig. 3.8 show the 1D PID histogram for particles stopped in the second silicon detector. Fig. 3.9 show the 1D PID histogram for particles stopped in the CsI crystals.

3.2.5 CsI calibration

The energy calibration of the CsI crystal is more difficult than that of Si detectors, because the light output of CsI(Tl) crystals depend on the charge, mass and energy of the detected particle. That is why one must construct the PID function before one performs the energy calibration of a CsI crystal. The light output for a particle with a certain charge and mass is a non-linear function of the energy loss for heavy ions and low energies. To address this, a non-linear energy-to-light relation was established. That depended both on the charge Z and mass A of the particle.

Many different empirical functions have been employed to construct energy calibrations of CsI(Tl) [47, 22, 72]. These parameterization typical are approximately linear at high energies but become very non-linear for low energies. Some of these

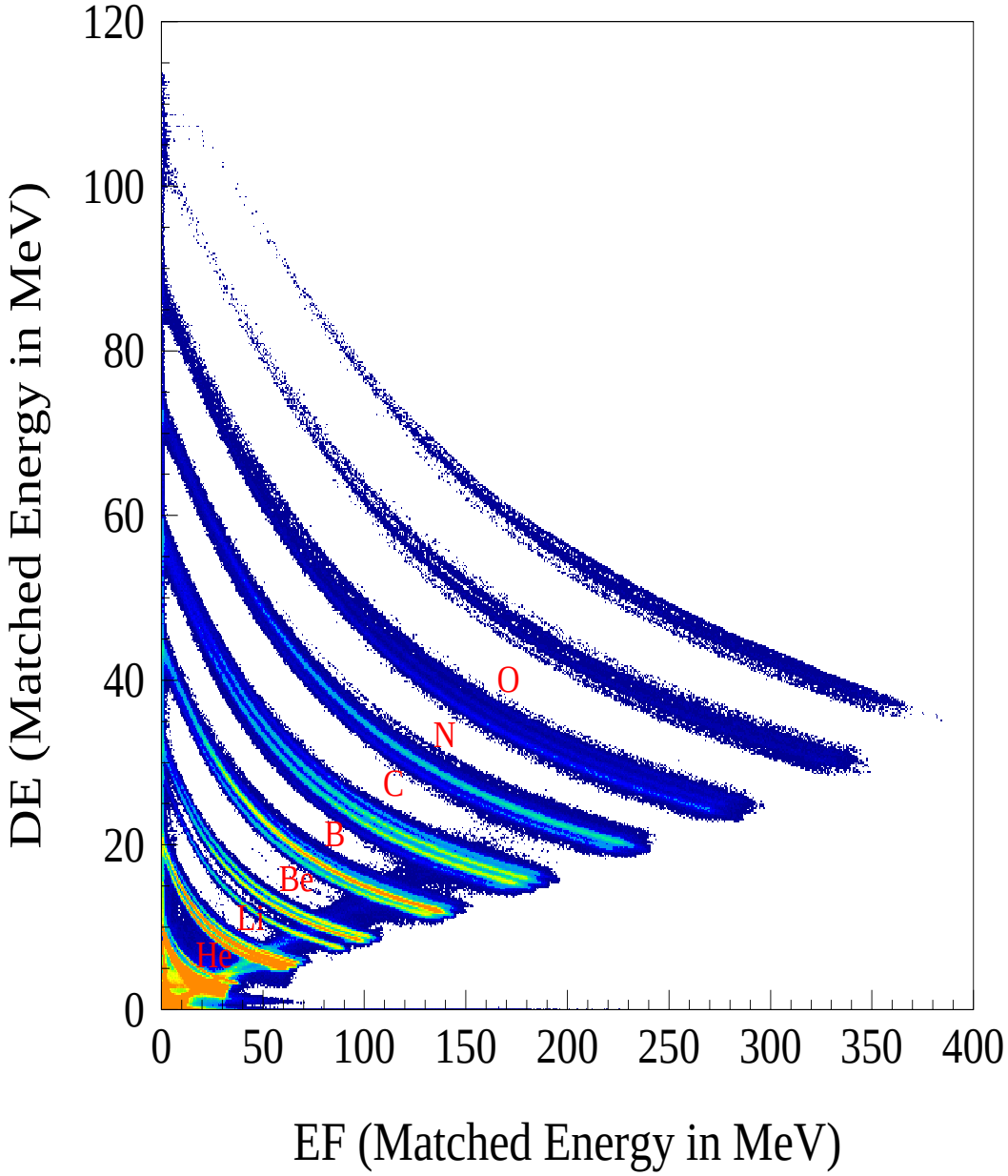

Figure 3.6: A histogram of counts vs. nominal DE energy and nominal EF energy

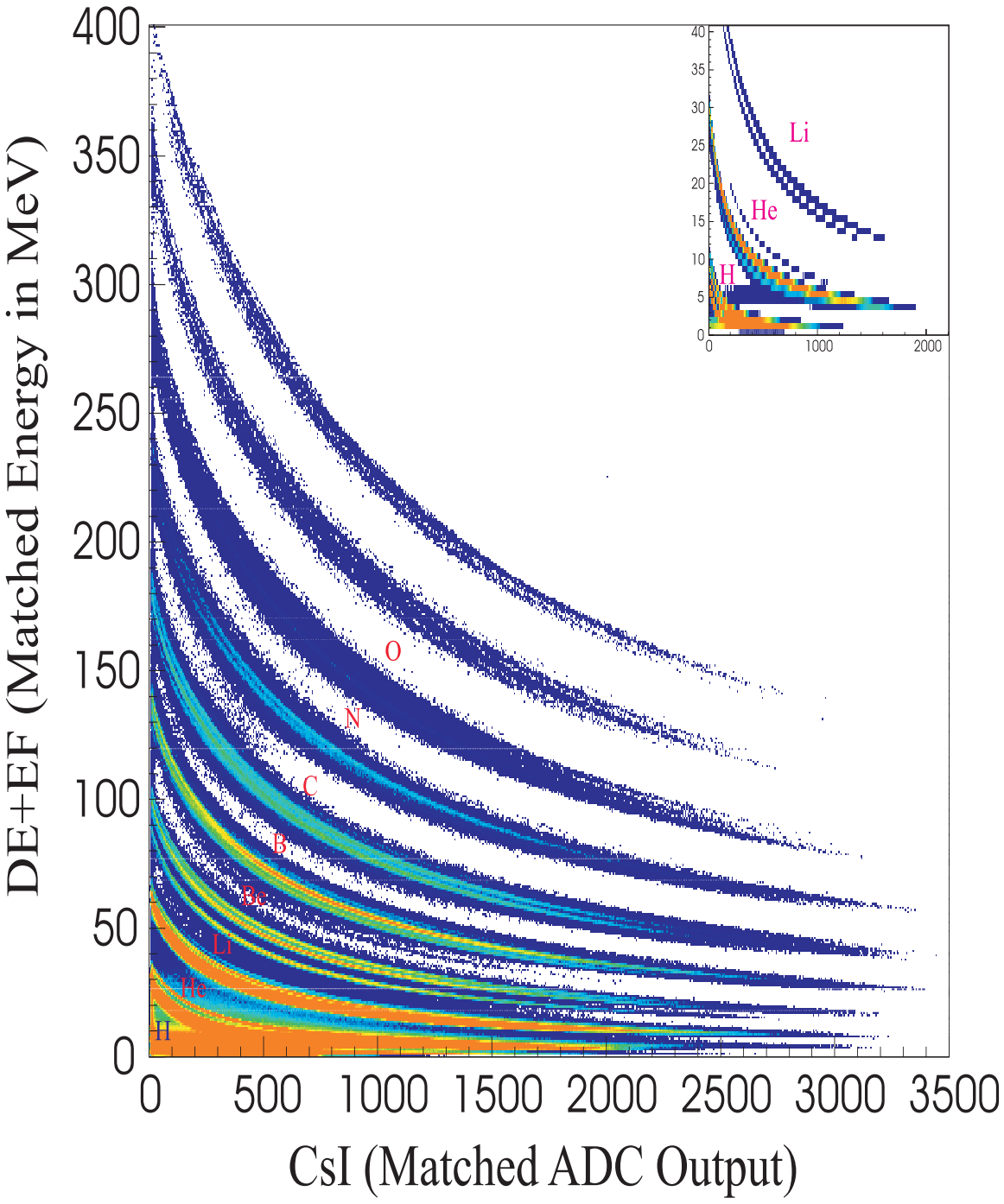

Figure 3.7: A histogram of nominal counts vs. nominal DE+EF energy and matched CsI light output. The isotopes of selected elements are indicated by labels that are immediately above the corresponding data.

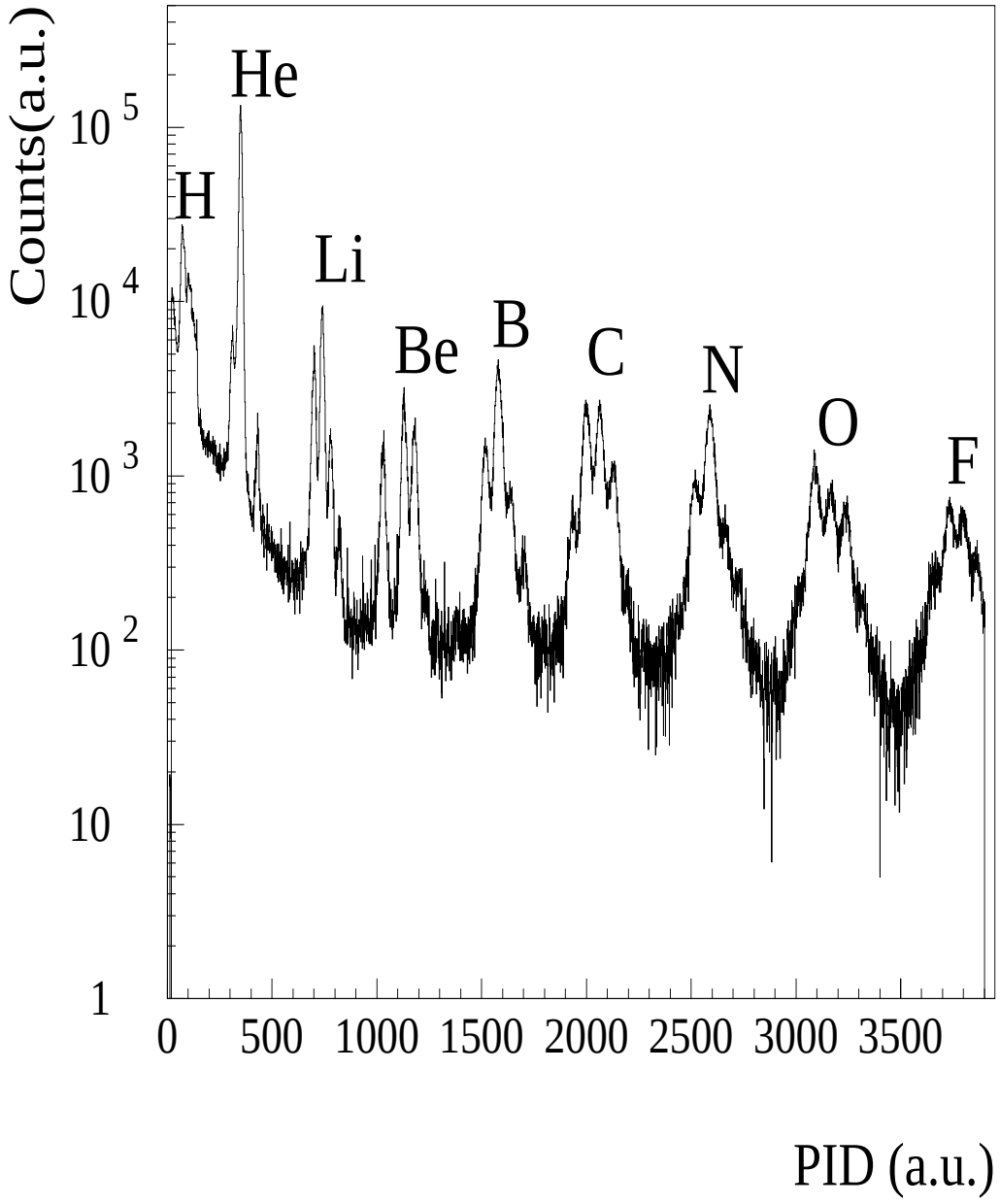

Figure 3.8: 1D PID histogram for particles stops in the second silicon detector

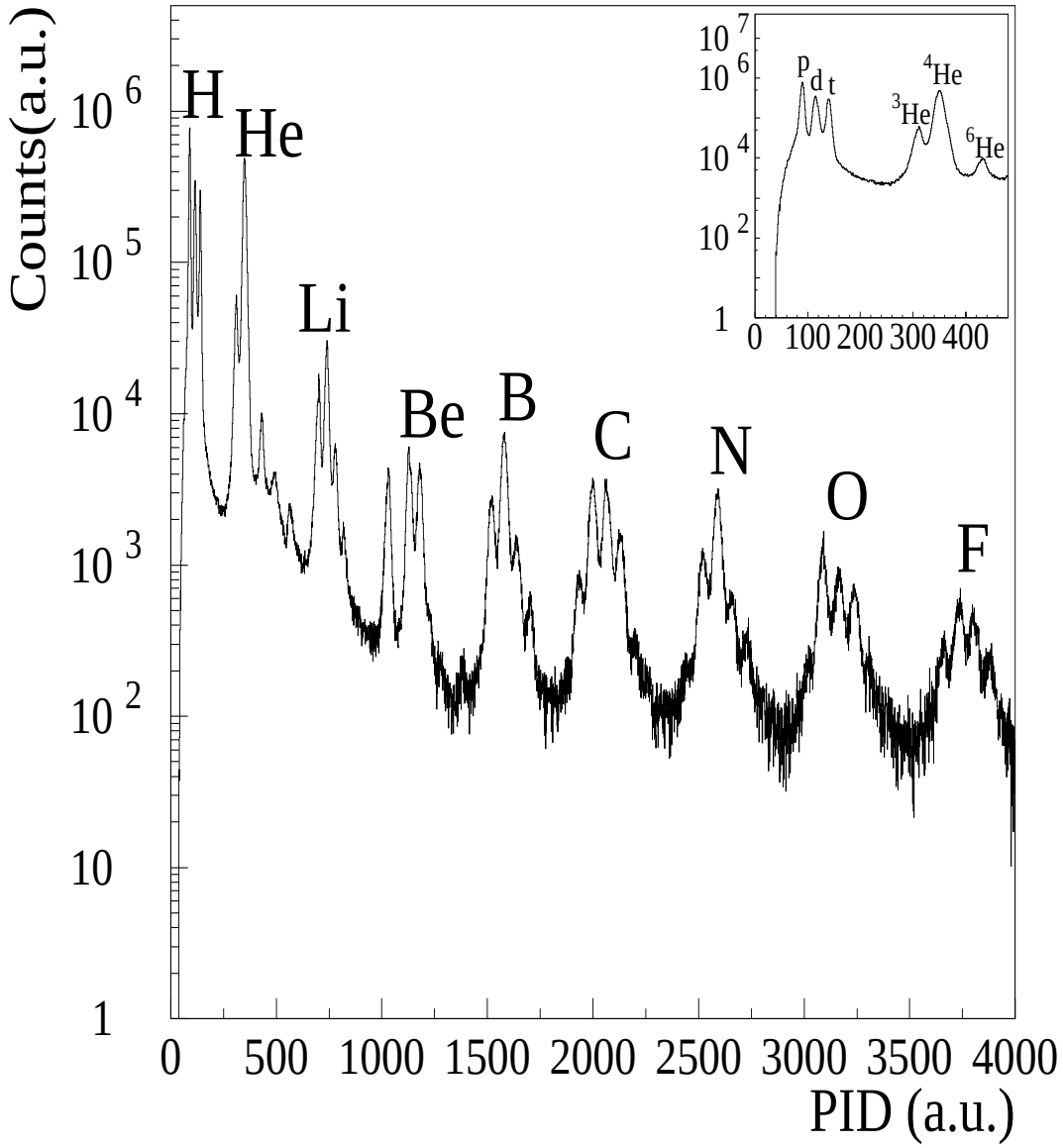

Figure 3.9: 1D PID histogram for particles stops in the CsI crystals

parameterizations have both a charge and a mass dependence while others are simply charge dependent. The best choice of calibration function depends on the Tl doping of the crystals.

For the crystals used in LASSA in this experiment, four calibration functions were used depending on the particle type [118]. These functions are similar to that proposed by Y. Larochelle *et al.* [56]. Larochelle's calibration function has the attractive feature that the deposited energy E is expressed as an analytical function of the light output, which is good for calibration purposes. It has an explicit mass dependence, necessary for the calibration of heavy ions. We discuss the other details in the following.

Following Larochelle, we parameterized the incident particle energy E for heavy ions of Z>3 as a function of the light output L, the charge Z, and the mass A of the particle, as follows:

$$E(L, A, Z) = aAZ^2L + b(1 + cAZ^2)L^{1-d\sqrt{A}Z} \ . \tag{3.2}$$

This expression has a linear part, that dominates at high energies and an exponential part that dominates at low energies. In Eq. 3.2.5 a, b, c, d are the fitting parameters which can be determined by fitting experimental points. The parameters a, b, c depend on the electronic gain and scintillation efficiency. The parameter a (affecting the linear part) is important for small Z and high energies. The parameters b and c (weighting the exponential part) describe the non-linearity at low energies and higher Z's. All parameters in Eq. 3.2.5 are positive. The parameter d is responsible for the transition from non-linearity to linearity in the energy response. Larochelle identifies L with the slow component (7 μs time constant) of the light output. In our parameterization, L is the total light output instead.

In Fig. 3.10 the fitting curves as well as the calibration points are shown for Carbon. In Fig. 3.10, the solid and dot-dashed lines represent the best fit of Eq. 3.2.5

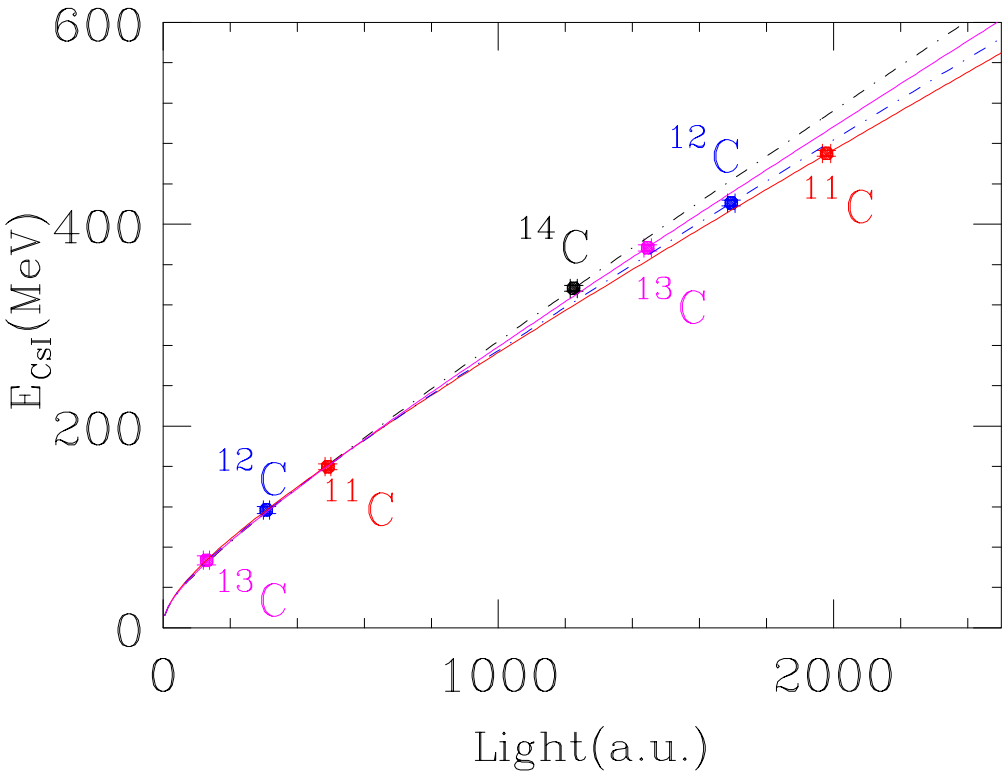

Figure 3.10: Calibration curves of Carbon for LASSA CsI(Tl)

to the experimental energy calibration data corresponding to different carbon isotopes (A=11-14). The need for a mass dependence can be demonstrated by examining the light output of the higher energy carbon isotopes. At high energy, the light response is expected to be linear. Both the ^{11}C points should lie in the linear domain. However, a straight line joining the two ^{11}C isotopes does not pass through the high-energy ^{12}C, ^{13}C, and ^{14}C isotopes. A curve going through all points for the $^{11-14}$C would lead to a very large and unreasonable curvature compared to calibration procedures adopted elsewhere in the literature. This mass-dependent calibration curve appears to be a

more reasonable solution. Since several fragmentation beams would be required to have the full calibration curve for each isotope, we adopt the mass-dependent ansatz (closely related to the quenching effect) of Larochelle [56].

For light-charged particles with Z≤3, the parameterization described in Eq. 3.2.5 did not accurately describe the detected energies. Compared to the observation of Larochelle *et al.* [56], a less pronounced isotopic effect was observed for light ions. This may be the result of the increased concentration of the activator element, Tl, in the CsI-crystals used in the present study compared to those studied in Ref. [56]. We find the mass dependence to be overestimated by the AZ^2 factor in Eq. 3.2.5, and employ a modified function of Eq. 3.2.5 with a weaker dependence on A to fit $Z \leq 3$ particles. This will give us the following three modified calibration functions for light particles:

For lithium ($Z = 3$) particles, we changed the first term of Eq. and used the follows:

$$E(L, A, Z) = a\sqrt{AZ^2}L + b(1 + cAZ^2)L^{1-d\sqrt{A}Z} \ . \tag{3.3}$$

For helium ($Z = 2$) isotopes, the following calibration equation was used:

$$E(L, A, Z) = aL + bA^c(1 - e^{dL}) \ . \tag{3.4}$$

The variables a, b, c, and d in Eq. 3.2.5, 3.3 and 3.4 are fit parameters. There are sufficient data to reproduce with good accuracy the light-output response for all the isotopes of the same element using Eq. 3.2.5 - 3.4.

As we have only two calibration points for each isotope, p, d and t, we adopt the simple linear function for $Z = 1$ particles.

$$E = aL + b \ , \tag{3.5}$$

where a, and b are fitting parameters. A linear CsI(Tl) response is consistent with that observed for hydrogen isotopes by Handzy [45].

Table 3.1 show the fitting parameters for all the isotopes.

Z	A	a	b	c	d
1	1	0.2010	-0.9587		
1	2	0.1916	-1.214		
1	3	0.1784	0.8212		
2		0.1696	4.575	0.3380	-0.05772
3		0.01783	0.2456	0.09743	0.06358
4		0.0006680	0.4493	0.01015	0.02616
5		0.0006354	2.944	0.002940	0.03713
6		0.0004102	2.362	0.003566	0.02869
7		0.0003101	4.834	0.002213	0.02734
8		0.0002289	4.701	0.002042	0.02301

Table 3.1: Table of the fitting parameter used in the energy calibration functions of LASSA CsI(Tl) crystals

The calibration functions used above have been used to calibrate 36 CsI (Tl) crystals of LASSA. To provide the calibration points, fragmentation products ranging from hydrogen to oxygen isotopes produced in fragmentation beams and direct α and proton beam particles were used. The detectors were directly exposed to low-intensity (1000 particles/s) beams of different isotopes and energies. These ions were obtained by fragmenting 2160 MeV ^{36}Ar and 960 MeV ^{16}O primary beams from the NSCL K1200 cyclotron in the A1200 fragment separator [90]. The main advantage of this method is the availability of a large number of particles that could be detected simultaneously (up to 52 isotopes were identified in the case of the ^{36}Ar fragmentation). Since particles are selected only by their magnetic rigidity ($B\rho$=1.841 Tm for the ^{36}Ar beam and $B\rho$=1.295 Tm for the ^{16}O beam) one obtains a broad range of different isotopes and energies. The FWHM of the momentum widths for these particles were selected to be 0.5%. The atomic and mass numbers as well as energies of the particles used to calibrate the CsI crystals in the present work are listed in Table 3.2. Hydrogen and helium isotopes were also calibrated by elastic scattering of E/A=30 MeV p-^{4}He molecular beams on a Au target and by 240 MeV direct ^{4}He

beam particles.

^{16}O fragmentation products	E(MeV)	^{36}Ar fragmentation products	E(MeV)
p	77.17		
d	39.78	d	79.57
t	26.72	t	53.75
^{3}He	105.00	^{3}He	210.00
^{4}He	79.99	^{4}He	160.00
^{6}He	53.64	^{6}He	107.90
^{6}Li	119.90	^{6}Li	240.00
^{7}Li	103.10	^{7}Li	206.80
^{8}Li	90.40	^{8}Li	181.60
^{7}Be	182.20	^{7}Be	363.40
^{9}Be	142.50	^{9}Be	285.60
^{10}Be	128.40	^{10}Be	257.90
^{10}B	199.90	^{10}B	400.00
^{11}B	182.10	^{11}B	364.90
		^{12}B	335.40
^{11}C	261.20	^{11}C	521.60
^{12}C	239.90	^{12}C	480.00
^{13}C	221.80	^{13}C	444.40
		^{14}C	413.70
^{14}N	279.90	^{14}N	560.00
		^{15}N	524.00
		^{16}N	492.40
^{15}O	340.80	^{15}O	680.70
		^{16}O	640.00
		^{17}O	603.70
		^{18}O	571.30

Table 3.2: Table of fragmentation products used in the energy calibration of LASSA CsI(Tl) crystals

Our fitting procedure resulted in a precision of the energy calibration better than 2% for isotopes from ^{4}He to ^{20}O.

3.2.6 Background Subtraction

The spectrum shown in Fig. 3.6 is for all particles that do not have a CsI (Tl) signal; i. e. particles that either stop in the 500μm Si or "punch-through" 500μm Si but

somehow escape the detection by the CsI(Tl) crystals behind the silicon detector. The low intensity background haze visible in Fig. 3.6 between the element groups is due to particles passing through inactive regions (edges, inter-strips, etc.) of the telescope, resulting in inconsistent DE-EF combinations. Also visible in Fig. 3.6 is a faint band of particles with a positive slope at the high energy event of the isotope lines between He and C. Particles in this band "punch-through" the 500μm Si detector but are not rejected because no signal is observed in the CsI. These particles are present due to a slight misalignment of the Si detectors relative to the CsI(Tl) crystals, or due to the dead area between adjacent CsI(Tl) crystals (due to wrapping for the purpose of optical isolation). One is able to eliminate this contribution, at the expense of geometric efficiency, by gating selectively on the position in the Si detectors.

The background haze visible in Fig. 3.7 has the following origins. First, particles passing through the inactive regions of the telescope give rise to spurious EF-E(CsI) values. Also, coincidence summing of two or more particles detected within a sigle CsI(Tl) crystal is particularly evident in the low EF region. One source of these double hits may be that high energy light particles in combination with a second particle in a single CsI(Tl) crystal distort the E(CsI) signal. A second source of coincidence summing occurs when neutrons hit the CsI at the same time as a charged particle. This produces signals which superimpose on the signals of the charged particles and shift the PID lines. Higher order coincidence summing as well as noise from either the detector or the electronics can shift the PID lines as well.

It is very hard to make correction for the signals causing the background, i.e. to separate the noise from the real signals. A more practical way is to make an estimation of the background level and correct for the background accordingly. There are two types of corrections. One is the subtraction of background under the PID curve of each isotope and the other is the correct for losses due to coincidence sum-

ming that remove particles from a given PID line and move them elsewhere. We will discuss the background subtraction first. We studied the background and observed that the background level depend on three factors. First, the coincidence summing probabilities are detector related: charged particles have different coincident summing probabilities when they stop in the Silicon detector than when they stop in the CsI crystals. Second, the background level is energy related: charged particles with different energies have different background levels. Finally, the background level is also isotope related: the background level is somewhat different for different isotopes. For most of the isotopes, we estimated the background as follows. For central collisions (the event selection will be discussed in the next chapter), we generated 1D PID histograms for different detectors and in ten different energy bins, then background levels were estimated for each elements. For peripheral collisions, since the statistics is not high, we generated 1D PID histograms for different detectors, then background levels were estimated for each elements. We treated ^{7}Be, ^{3}He, ^{11}C, ^{15}O separately, because their background levels are not the same as other isotopes of the same charge number. For example, ^{7}Be has no neighboring isotopes, so the background level of ^{7}Be was estimated separately. For ^{3}He, ^{11}C, ^{15}O, there were significant leakages into these PID lines because their yields are weak compared with their neighboring ^{4}He, ^{12}C and ^{16}O isotopes. Fig. 3.11 show the contamination of ^{3}He by ^{4}He. To obtain the yields of ^{3}He, ^{11}C, ^{15}O, we only used the halves of the PID lines which are located at the far sides of their neighboring isotopes, which are believed to be free of contamination. Fig. 3.11 also shows that the PID line of ^{3}He is asymmetric. The reasons for that are: a) The PID algorithm does not requires isotope yields to be strictly symmetric about the middles of PID lines. b) There is a contamination of ^{3}He by ^{4}He. Fig. 3.12 shows that the background levels for IMFs as estimated by those fitted straight lines in the figure.

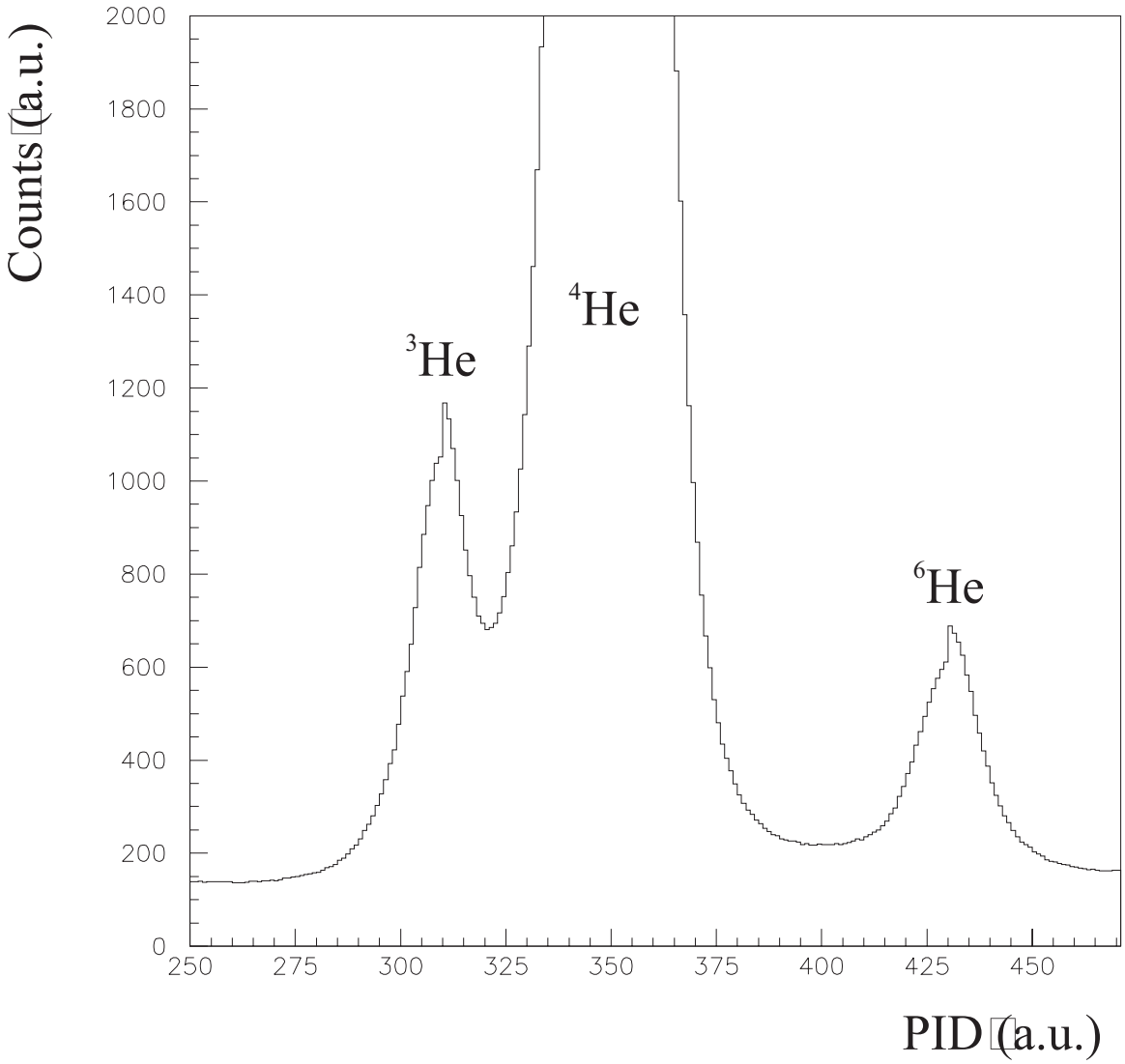

Figure 3.11: PID line of ^{3}He shows the contamination of ^{4}He. It also shows that the PID line of ^{3}He is asymmetric.

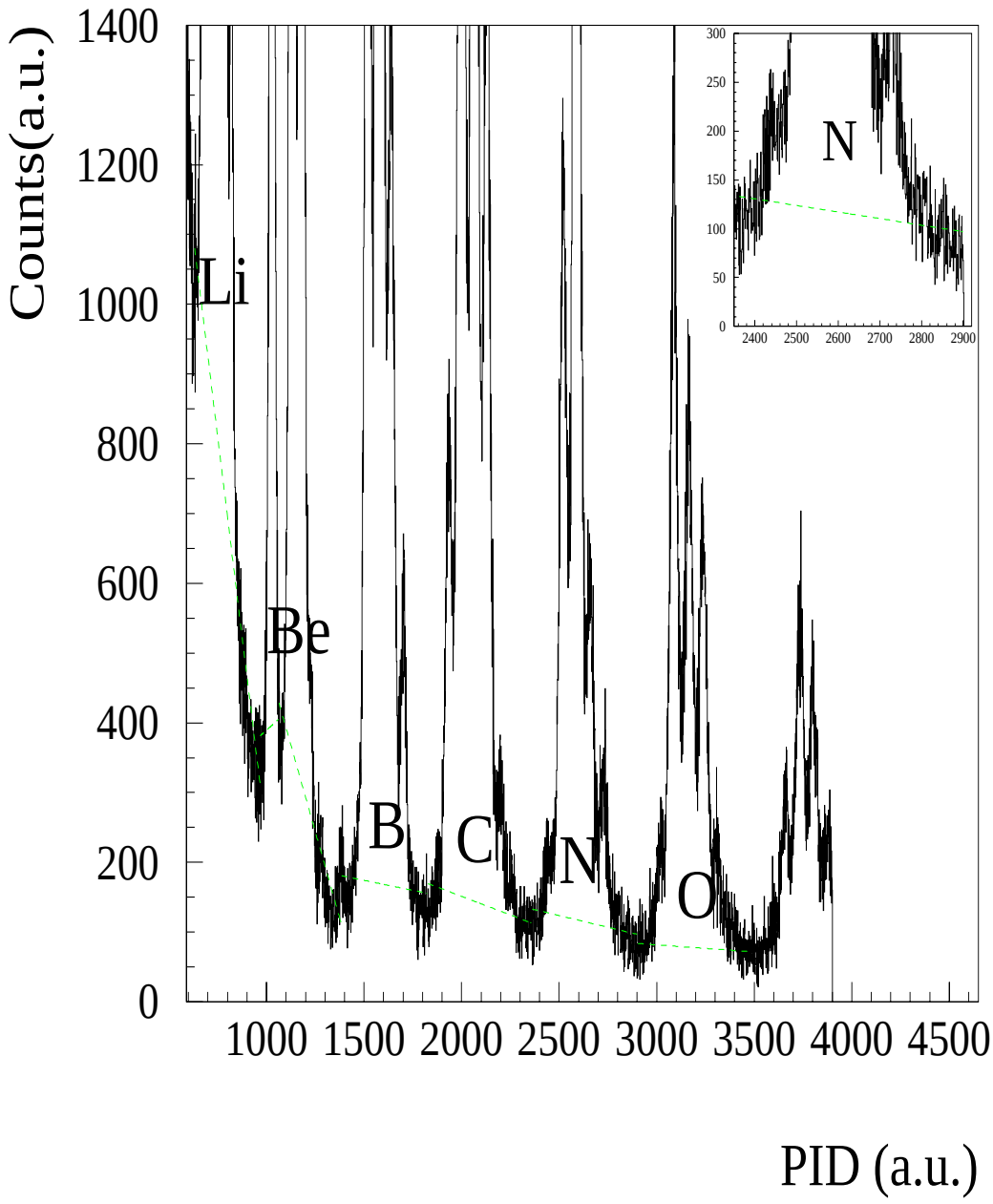

Figure 3.12: Background subtraction for the heavy fragments, the straight dashed lines are the estimated background levels.

3.2.7 Efficiency Correction

Ideally, if the detectors have perfect 4π coverage and can detect charged particles with any energies, there is no need for an efficiency correction. However, LASSA only has a limited geometric coverage and can only be placed at certain angles. For example, we can not detect those particles emitted in the direction very close to the beam line, since we can not put the detectors too close to the beam line without damaging the detector. We also cannot detect particles with energies that are below the detector thresholds or above the dynamic range of the electronics. This type of efficiency was easily noted but not easily corrected because we cannot definitely correct for data loss at angles where the efficiency is zero. Even if the particles are emitted in the directions covered by the LASSA array, they cannot be fully detected. The LASSA array can only detect and identify charged particles that stop in either the second silicon detector or the CsI crystal. The particles can not be detected and identified if they stop in other places: such as the Sn-Pb foils that covered the telescopes, the first silicon detector, the dead layers of the silicon detectors, the mylar foil that covers the crystals and the gap between Csi crystals. Multiple hits also cause losses in the charged particle detection. At polar angles where the detection-efficiency is not zero, the efficiency can be corrected for such effects.

In our analysis, efficiency functions were generated for each isotope and for different reactions. We construct the efficiency functions for central collisions and peripheral collisions in different ways for different purposes of study. For central collisions, we calculated 1D efficiency as a function of E_{cm} within each degree of θ_{cm}. For peripheral collisions, we calculated 2D efficiency as a function of $p_{\perp}/A$ and y_r. The efficiency functions are calculated as follows, isotopes were first generated from the even phase space in the center of mass frame, and then the kinetic energy and angle in the lab frame are calculated. If the isotope survives the double hits loss and

passes the detection threshold and was successfully detected by a good detector, then a weight of $1/N$ will be added to the corresponding point in either the E_{cm} space or the y_r vs. $p_\perp/A$ space for this isotope. Where, N is the number of total particles generated. The raw yields are then corrected by these efficiency functions.

On the top panel of Fig. 3.13, we show the raw yield of ^{4}He produced in the peripheral collisions of the ^{112}Sn + ^{112}Sn reaction as a function of vs. parallel relative rapidity, called y_r vs. the momentum per nucleon perpendicular to the beam direction, called $p_\perp/A$. The rapidity is defined by $\frac{1}{2}ln\frac{E+p_\parallel c}{E-p_\parallel c}$. The parallel relative rapidity is calculated by normalizing the rapidity parallel to the beam direction of ^{4}He particles by the beam rapidity. In the figure of the raw yield of ^{4}He, we see that there is an annular ring facing the origin with low counts. This discontinuity of the ^{4}He was caused by either ^{4}He particles stop in the dead layer of the second silicon or in the Mylar foils of CsI. This discontinuity was also caused by ^{4}He particles that stop in the CsI, but cause a very low light output due to the non-linear response of the CsI, which is so low that we can not detect it. This loss in the efficiencies affects the yields for central collisions at the order of 2%. We also see edges of enhanced yields for certain polar angles θ. On the bottom panel of Fig. 3.13, we show the efficiency function, with double hit effect taken into account, of ^{4}He for the ^{112}Sn + ^{112}Sn reaction. We see the same enhanced angles of emission because we take the solid angle coverage into account in the efficiency simulation. On the other hand, we make no attempt to simulate the loss of counts due to the discontinuity where ^{4}He punches into the CsI because this is difficult to simulate accurately enough. In the first panel of Fig. 3.14, we divided the measured yield by the efficiency function to obtain the corrected yields vs. y_r and $p_\perp/A$ for ^{4}He produced in the peripheral collisions of the ^{112}Sn + ^{112}Sn reaction. We see that the angle dependent of the efficiency is well corrected. In the other 3 panels of Fig. 3.14, we show the corrected yields for all the other reactions.

We see from this figure that after correction, the yield is smoother comparing with the raw yield. The "Coulomb ring", which centered at $y_r \sim 0.95$ is more prominent in the corrected yield comparing with the raw yield. In Fig. 3.15, we reflected the corrected yield of ^{4}He with respect to the line of $y_r = 0.5$ and the line of $p_\perp = 0$, since the yields should be symmetric with respect to these lines for symmetric reactions. The corrected y_r vs. $p_\perp/A$ plot provides our best global picture for ^4He emission in this reaction.

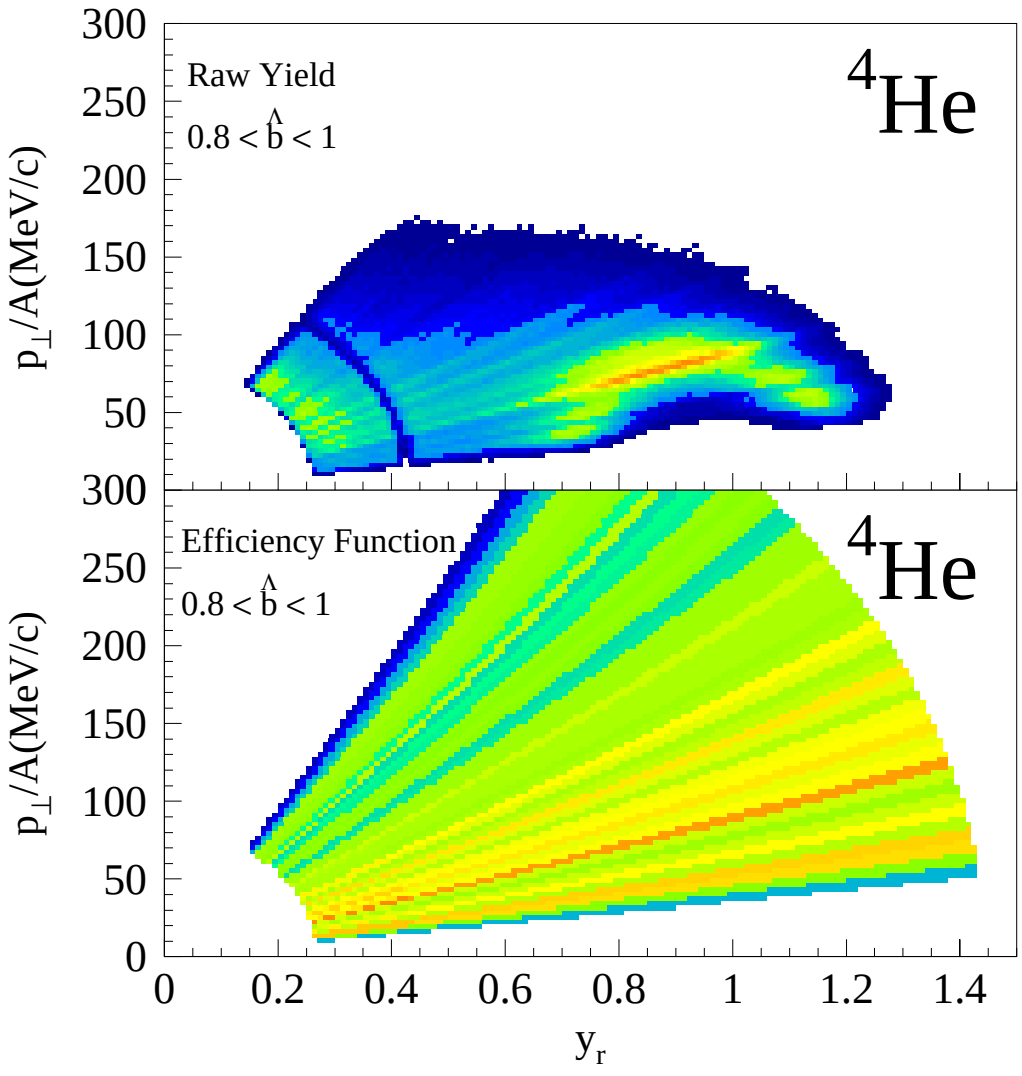

Figure 3.13: The raw yield and the efficiency function for ^{4}He produced in the peripheral collision for the ^{112}Sn + ^{112}Sn reaction

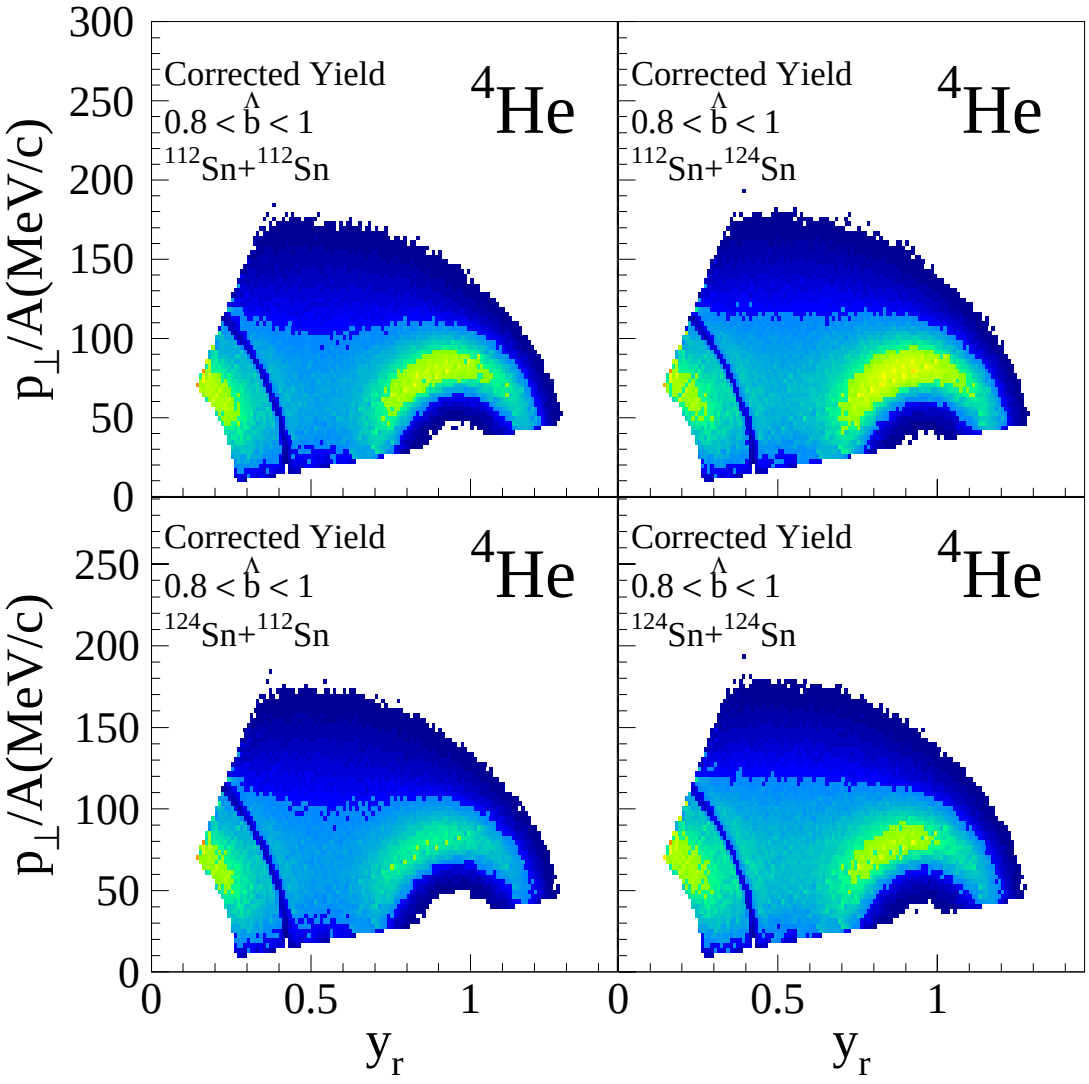

Figure 3.14: The corrected yields of ^{4}He produced in the peripheral collisions for different reactions.

3.3 Data Analysis of the Ring Counter

The Ring Counter has similar structure to the LASSA array. The data analysis for the Ring Counter is basically the same as the LASSA array. One needs to do a similar energy calibration and generate a Si-CsI PID function as what are done for the LASSA array. We will discuss about the energy calibration and PID function

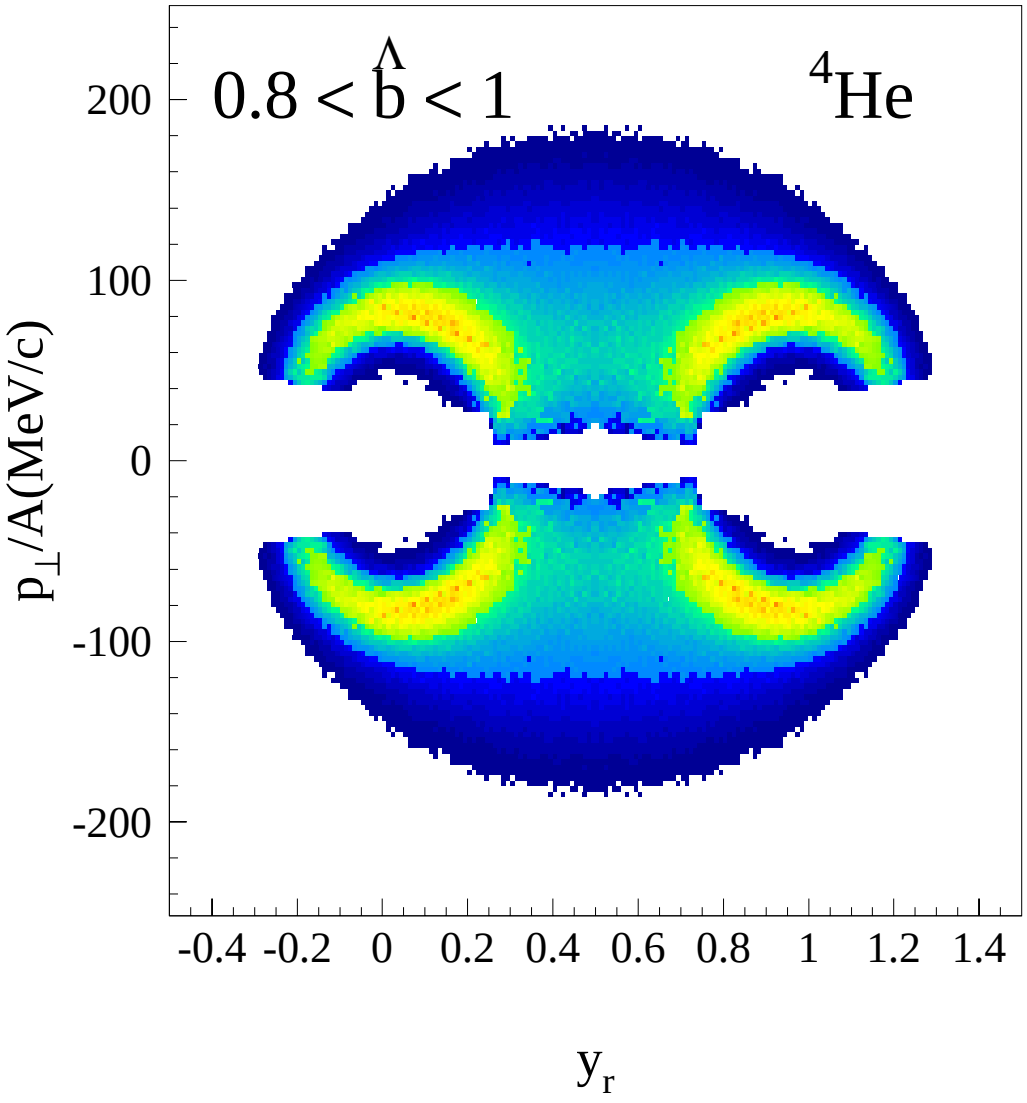

Figure 3.15: Reflected yield of ^{4}He produced in the peripheral collisions for the ^{112}Sn + ^{112}Sn reaction

of the Ring Counter in detail in the following sections. Since the Silicon detectors and the CsI crystals are not tightly mounted in a box as was LASSA, there could be a misalignment between the Silicon detectors and the CsI crystals. We found that the misalignment effects were not the same for all of the 16 Pie sectors. The overall effect of the misalignment caused a loss at the order of 7% of the total projectile-like fragments detected. Fig. 3.16 gives the flow chart of the algorithm of the program used for the Ring Counter analysis.

3.3.1 Energy Calibration

The calibration of the Ring Counter is almost the same as the LASSA array, except that there is no proton recoil measurement, which is the last stage for LASSA calibration. First, we used a different charge terminator to have a pulser calibration over the dynamic range of 10GeV for the silicon calibration. Only the signals from the pie side were used for energy. In the beam calibration stage, both silicon and CsI(Tl) detectors in the Ring Counter were also calibrated with direct beams of 80MeV/A ^{17}O and 60MeV/A ^{36}Ar, and cocktail beams, consisting of a mixture of 60 MeV/A ^{48}Ti, ^{52}Cr, ^{56}Fe, ^{60}Ni, ^{64}Zn, ^{68}Zn, ^{12}C beams. The response of the annular silicon-strip DE detectors is a fairly linear function of the energy deposited and independent of the species of ions. The Si energy calibration shown in Fig. 3.17, was achieved with an accuracy of 1%. The CsI(Tl) detectors, however, display a non-linear response to the energy deposition, which is mass and charge dependent [118]. For the CsI(Tl) calibration, there was insufficient information to establish the calibration of the CsI for each species. The energy calibration of CsI(Tl) is done by matching newest beam calibration to the calibration curve obtained for the Ring Counter in a prior experiment. We found that the prior calibration [34] appears to be very consistent and we believe that it is very good. The calibration curve, shown in Fig. 3.18 which gives

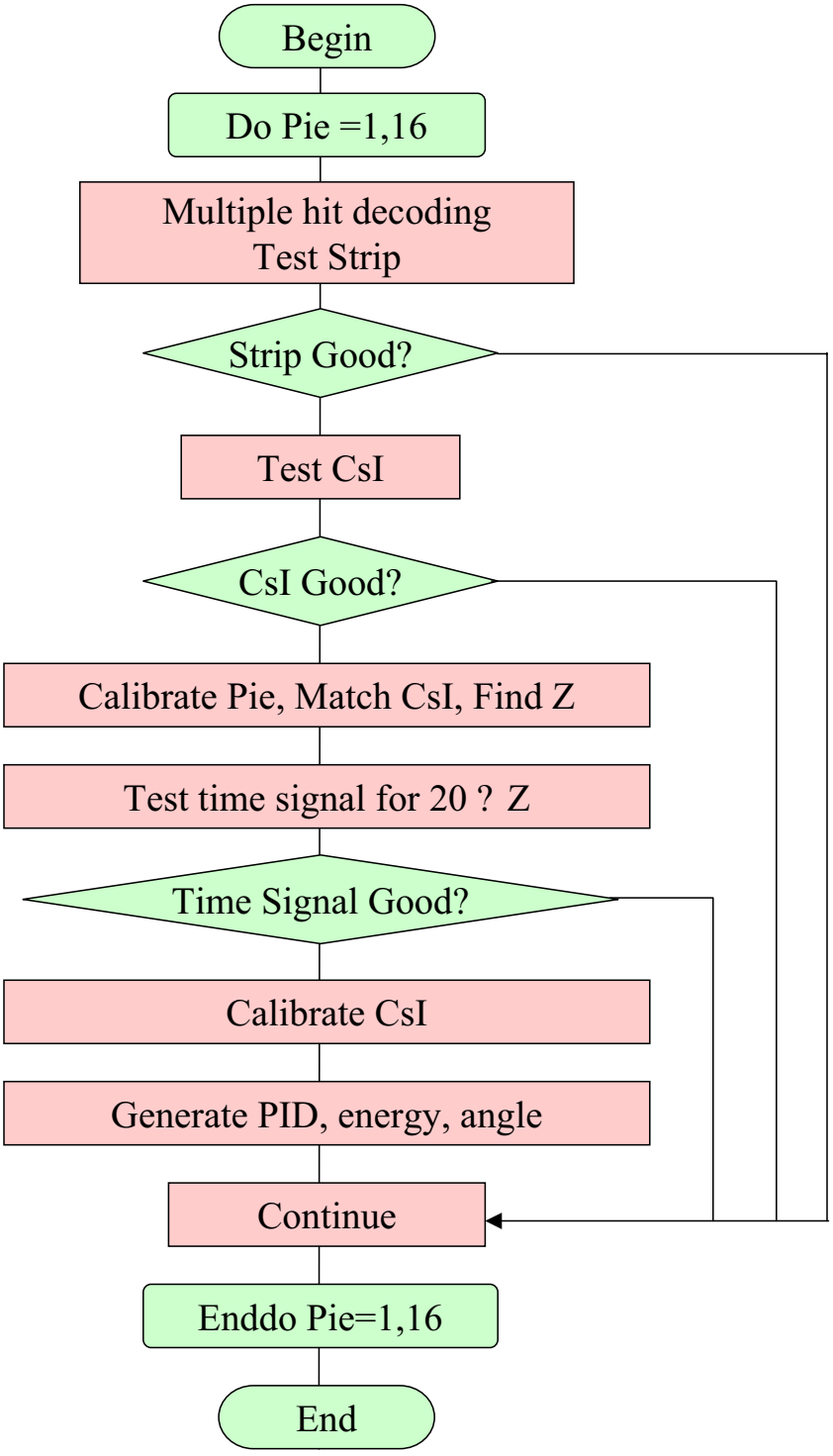

Figure 3.16: Flow chart of the algorithm of the Ring Counter analysis

the energy calibration of CsI(Tl) to an estimated accuracy of 3%. The total energy calibration of △E + E is at an accuracy of about 3%.

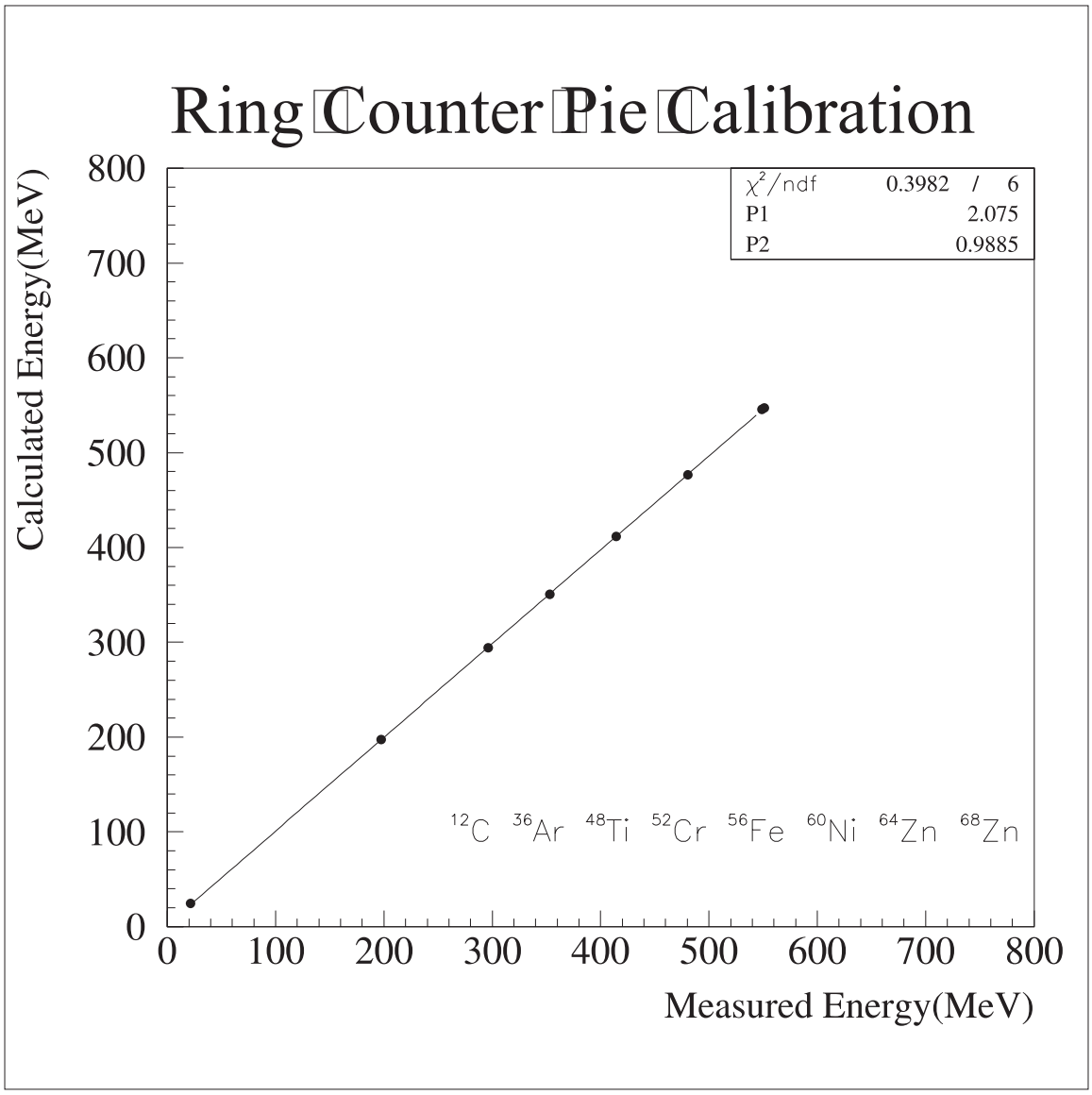

Figure 3.17: The energy calibration of the silicon detector(Pie side) of the Ring Counter

3.3.2 PID function

From the raw output of ΔE and E detectors, one can construct two-dimensional matched ΔE and E histograms to identify the detected charged particles. Since the

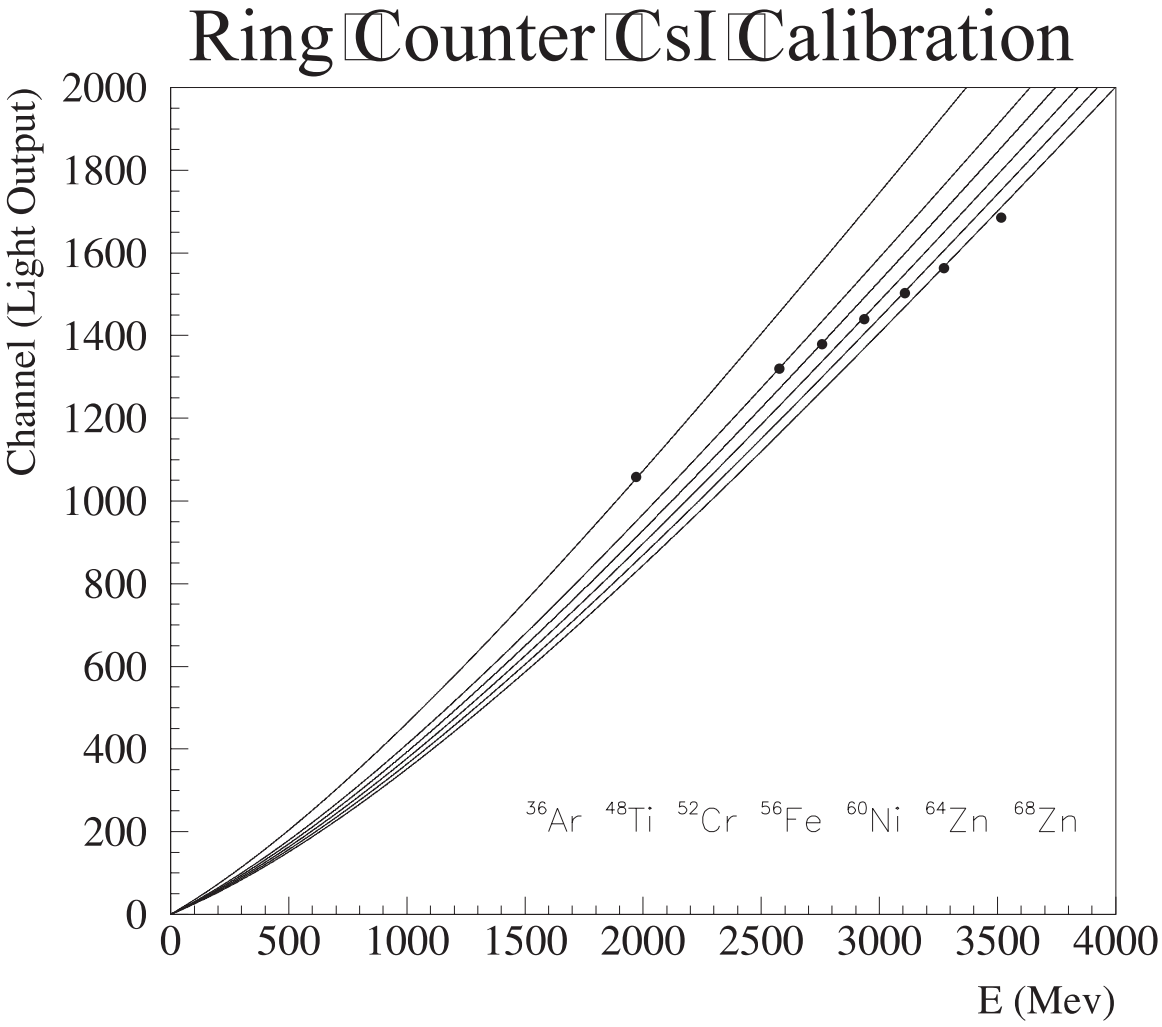

Figure 3.18: The energy calibration of the CsI detector of the Ring Counter

Silicon detector of the Ring Counter is very thick (298 μm), the thickness correction is not necessary. We simply used the calibrated energy deposited by the charged particles in the Silicon detectors as ΔE, and the matched light output from the CsI crystals as E. Fig. 3.19 shows the "stretched" PID lines of the Ring Counter. In this figure, elements from $Z = 2$ to $Z = 50$ are clearly distinguished. Fig. 3.20 shows the 1D PID function of the Ring Counter.

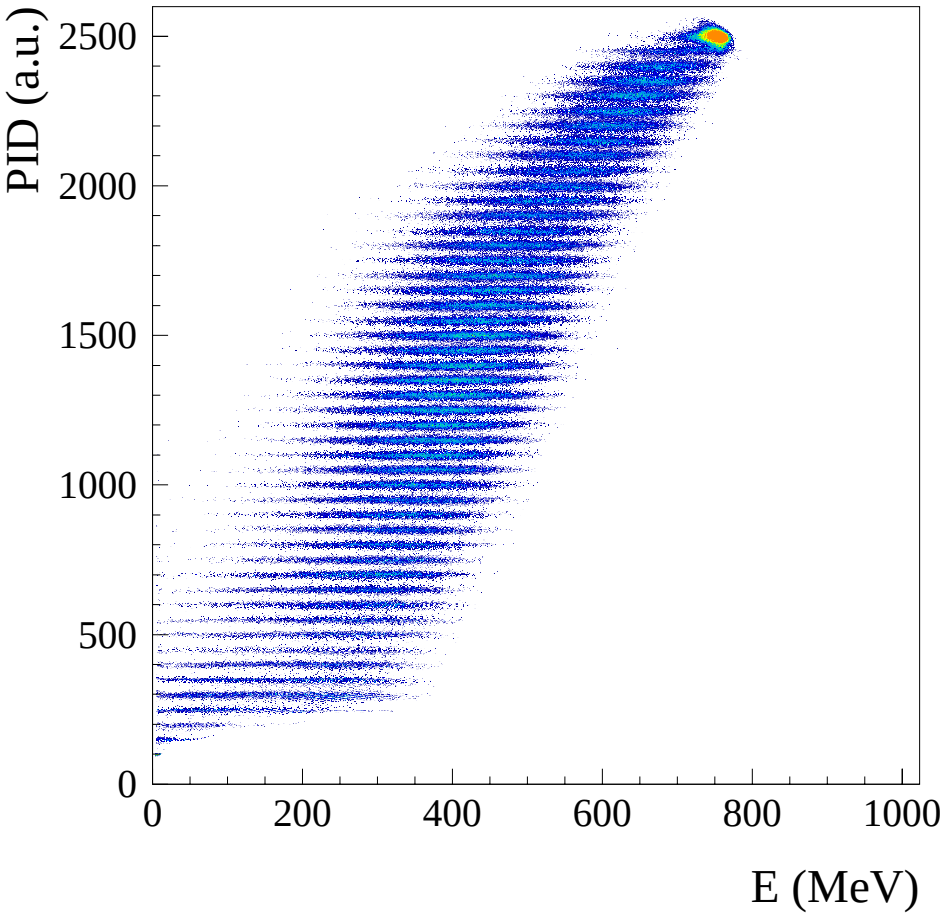

Figure 3.19: The 2D PID lines of the Ring Counter

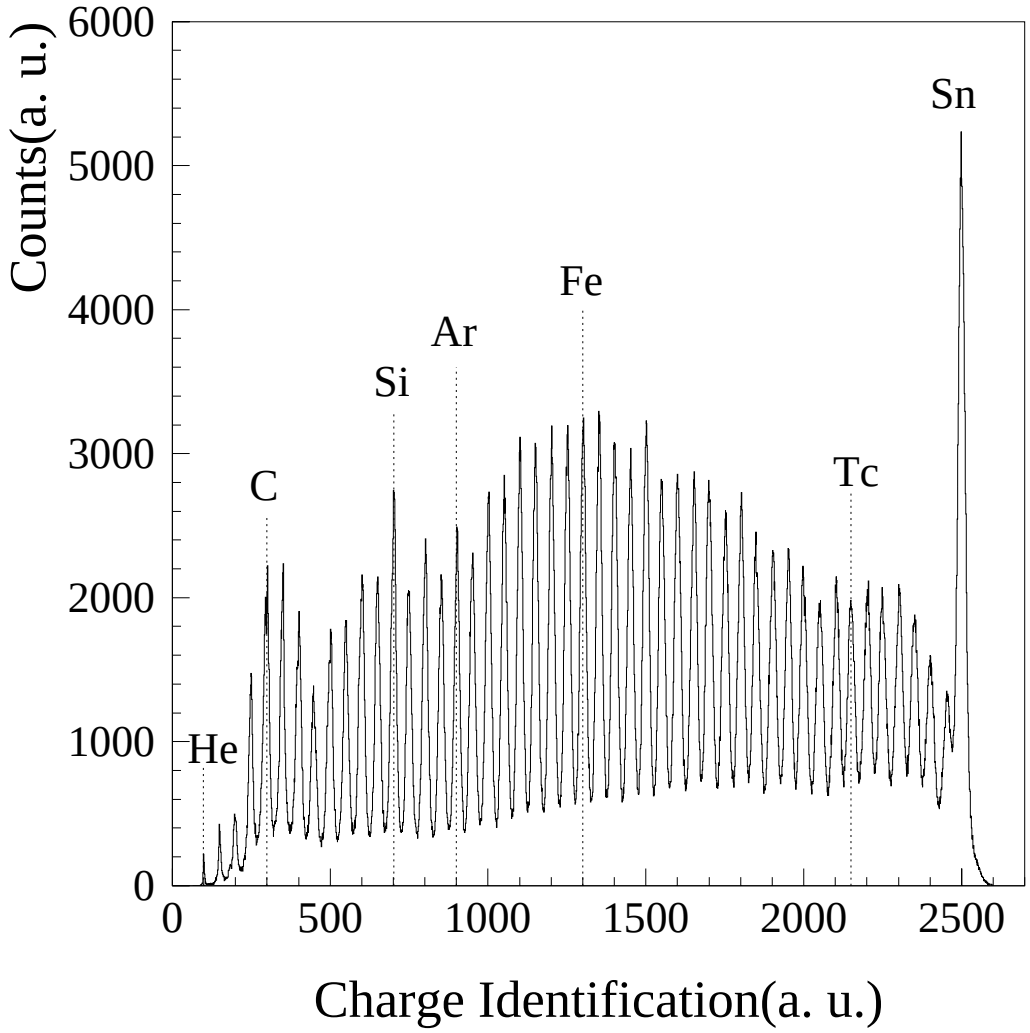

Figure 3.20: 1D PID function of the Ring Counter

Chapter 4

Experimental Data and Model Comparisons

4.1 Impact Parameter Selection

Classically, the impact parameter "b" of nucleus-nucleus collision is defined by the distance between the straight-line trajectories of the centers of the two nuclei before their interaction. In experiments, however, one can only use the experiment observables to get some information of impact parameter. Then one uses this information to construct impact parameter filter which selects range of the impact parameter. Examples of such variables are the total charge particle multiplicity, N_c, the total proton multiplicity, N_p, the total detected charge, Z_{tot}[84], or the charge of projectile-like fragment, Z_{plf}. In the present work, we use the charged particle multiplicity [84, 53]

to construct the impact parameter filter for all of the experimental results. In a rough picture, the charge particle multiplicity depends on the energy transferred from the relative nuclei motion to internal degrees of freedom in the region of the overlap between projectile and target. More charged particles will be emitted in more central collisions with a stronger overlap than in peripheral collisions where the overlap is less. Based on the assumption that charged particle decreases monotonously with impact parameter multiplicity, a reduced impact parameter or "$\hat{b}$" can be calculated from the charged particle multiplicity. The reduced impact parameter, first suggested by Cavata *et al.* [19], can be written as:

$$\hat{b}(N_c) = \frac{b(N_c)}{b_{max}} = \Big[\sum_{N_c}^{\infty} P(N_c)\Big]^{1/2} \Big/ \Big[\sum_{N_c(b_{max})}^{\infty} P(N_c)\Big]^{1/2}, \quad (4.1)$$

where N_c is the charged particle multiplicity corresponding to b, $P(N_c)$ is the relative frequency of events being detected with the charged particle multiplicity equals to N_c, and $N_c(b_{max})$ is the charged particle multiplicity corresponding to b_{max}, the minimum bias impact parameter. In this experiment, $N_c(b_{max}) = 4$. This relationship is rigorous only under two assumptions: First, the nucleus-nucleus cross section can be well approximated by the geometrical cross section: $\sigma_g = \pi b^2$. This is good for relativistic bombarding energies [19], but may not be strictly applicable to the intermediate-ranged bombarding energy, like what it is in this experiment. Second, there should be a monotonic correlation between multiplicity and impact parameter without dispersion. This could not be well justified either. Considerable fluctuations of the charged particle multiplicity can be expected even for collisions of well-defined

impact parameter. Nevertheless, we use this impact parameter to select the centrality of the nucleus-nucleus collision, and group the events to different bins, "central", "mid-central" and "peripheral" collisions. We then must be aware that these gates may be somewhat empirical due to fluctuations in the charged particle multiplicities.

In our analysis, the charged particle multiplicity, N_c, consists of all the charged particles detected in the Miniball/Miniwall array and LASSA telescopes. Those detected charged particles not only include the identified particles but also unidentified particles. For Miniball/Miniwall array, such unidentified particles includes heavy fragments that stop in the fast plastic and light particles that punch through the CsI(Tl) crystals. For LASSA telescopes, the unidentified particles includes heavy particles that stop in the first silicon, the light particles that punch through the CsI(Tl) and the particles that hits at inter-CsI gaps.

In Fig. 4.1, the probability distribution of the charged particle multiplicity as well as the impact parameters are shown for all four reactions. A threshold of $N_c = 4$ is chosen from the setting of the hardware trigger during the experiment. In Fig. 4.1, we can see that the probability distribution of N_c is rather flat between N_c=4 and N_c=25, then there is an exponentially decrease above N_c=25.

The impact parameter b is derived from $\hat{b}$ and b_{max}. $\hat{b}$ is calculated from the procedure described in Eq. 4.1 and b_{max} is calculated by measuring the cross section $\sigma = \pi b_{max}^2$ for events with $N_c \geq 4$. We obtained values of b_{max} =7.50fm for reaction ^{112}Sn+^{112}Sn; b_{max} =7.20fm for reaction ^{112}Sn+^{124}Sn; b_{max} =7.38fm for reaction ^{124}Sn+^{112}Sn; b_{max} =7.02fm for reaction ^{124}Sn+^{124}Sn. While there is a difference in the b_{max} of the four reactions, it is within the systematic errors in the procedure. We take b_{max} =7.5fm for all four reactions. In the following discussions, central collision corresponds to the gate of $0 < b < 1.65fm$ $(0 < \hat{b} < 0.2)$; peripheral collision corresponds to the gate of $6fm < b < 7.5fm$ $(0.8 < \hat{b} < 1)$.

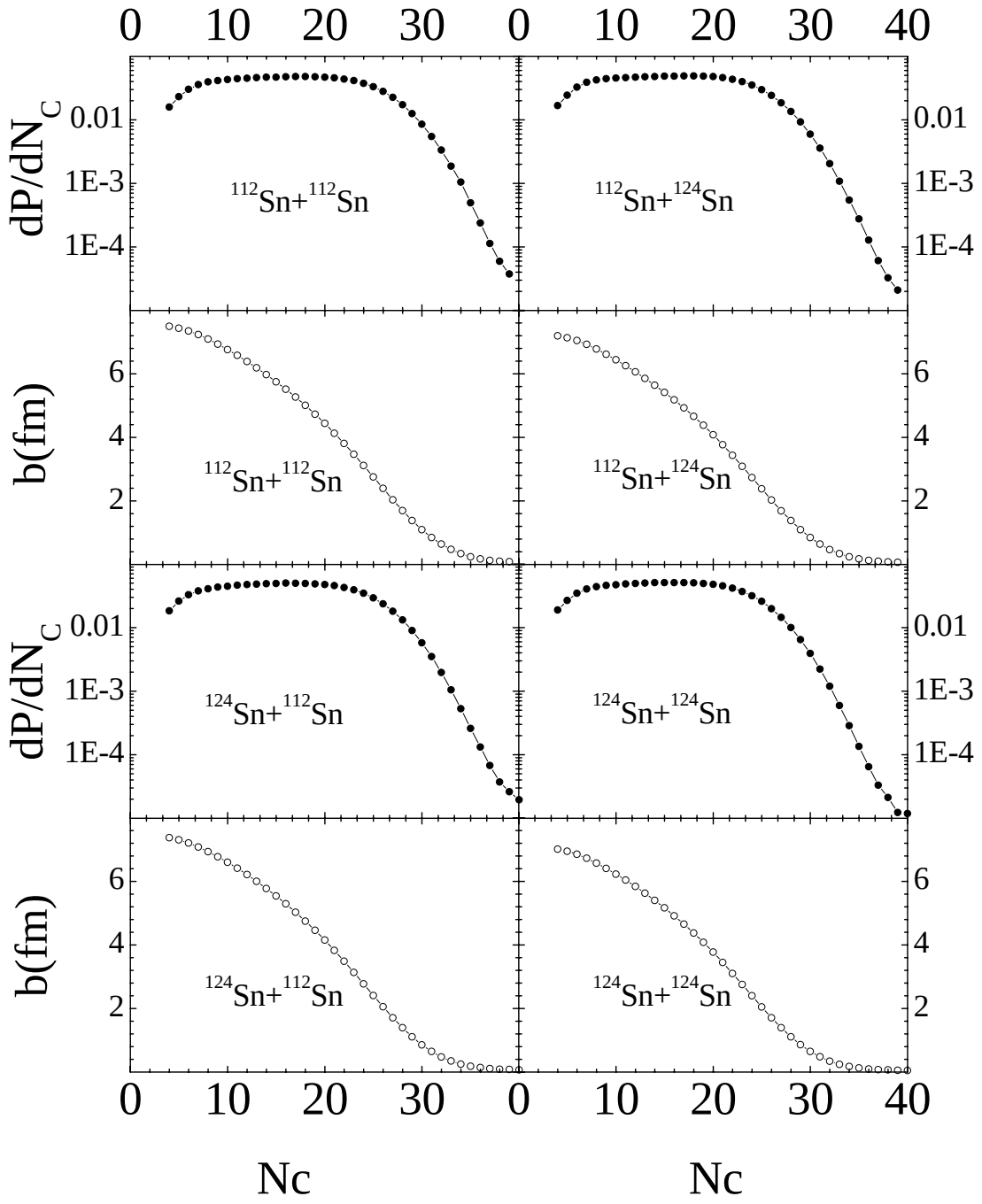

Figure 4.1: The probability distribution of the charged particle multiplicity, N_c, and the derived impact parameter as a function of the charged particle multiplicity.

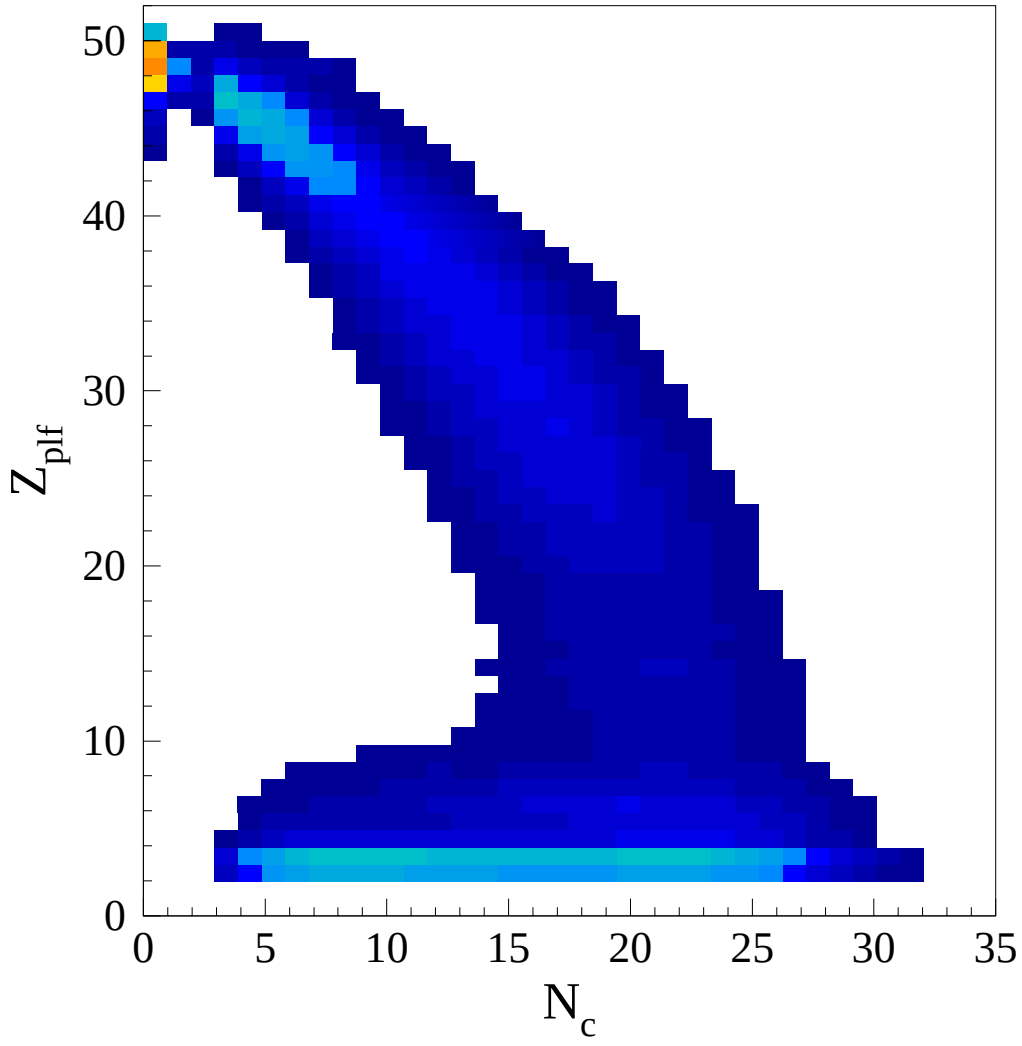

Figure 4.2: The charge of project-like fragments, Z_{plf}, as a function of the charge multiplicity N_c

Other observables can also be used to construct impact parameter filter. Since there is a strong correlation between charged particle multiplicity and impact parameter. We can test the correlations between other observables and charged particle multiplicity to check their correlations with impact parameter. We explored the correlation between the charge of PLF(Project-Like Fragments), detected in the Ring Counter, and charged particle multiplicity for example. In Fig. 4.2, we see that there is a strong correlation between the Z_{plf}, the charge of PLF detected in the Ring Counter, and N_c. In the region of Z_{plf} larger than 20, Z_{plf} decreases monotonously with N_c. This can be understood since the more charge left in the PLF, the less charge left for the overlap regions of the reactions thus less charge particles were detected by Miniball/Miniwall and LASSA. In the region of Z_{plf} smaller than 20, Z_{plf} smears out, suggesting that the correlation does not exist anymore. We do not always detect the PLF because it sometimes goes to smaller angles outside of our coverage. Thus, we chose the reduced impact parameter constructed from N_c as the primary impact parameter filter for this study and not the PLF charges. A two-dimensional cut on two different impact parameter gates has not been used to place more restrictive gates on the event selection, even though that might lead to greater precision in the impact parameter selection for some studies.

4.2 Isotope Multiplicities, Energy Spectra from Central Collisions and Model Calculation

4.2.1 Experimental Data

The differential multiplicities of different isotopes were obtained by first selecting the central collision events with $\hat{b} < 0.2$, as explained in the section 4.1, then within each event selecting the fragments emitted at center of mass angles of $70^\circ \leq \theta_{cm} \leq 110^\circ$.

The acceptance of LASSA and the impact of this acceptance cut on the data are illustrated in Fig. 4.3. In this figure, we show the corrected yield in the center of mass frame as a function of E_{cm} and polar angle θ_{cm} for ^{4}He produced in the central collisions of the ^{112}Sn + ^{112}Sn reaction. The cut $70^\circ \leq \theta_{cm} \leq 110^\circ$ is indicated by the dashed lines in the figure. At these angles, the coverage of the LASSA array is excellent and the efficiency is well behaved. The only losses occurred for particles emitted at very low energies $E/A < 0.2$ MeV in the center of mass, corresponding to small laboratory angles of $\theta_{lab} < 7^\circ$, as well as at high energies, corresponding to laboratory angles of $\theta_{lab} > 58^\circ$. These losses (total $< 2\%$) were estimated by fitting the energy spectra for each isotope and corrected by the efficiency function. The acceptance of LASSA is also shown in Fig. 4.4. In this figure, the efficiency corrected differential multiplicity $dM/dydp_\perp$ for ^{12}C fragments is shown. The angle cut is indicated by the dashed lines in the figure as well. The measured differential multiplicities smoothly depend on the transverse momentum $p_\perp$ and rapidity y and are centered about the rapidity of the center of mass, consistent with emission from the participant source. They display no characteristic "Coulomb holes" near the projectile rapidity, expected from the Coulomb repulsion of ^{12}C fragments from projectile-like residues moving with velocities somewhat less than that of the projectile.

The final differential multiplicities were obtained after background subtraction and efficiency correction. Background level was approximated by fitting each element on the 1D PID histogram with different energy bins cut, then subtract the background corresponding to each energy bin. Totally ten bins were chosen according to the statistics of the yields of the fragments. The efficiency correction was done for each degree from 70° to 110° in the center of mass frame. Fig. 4.3 shows the 2D E_{cm}-θ_{cm} histogram for ^{4}He after the background subtraction and efficiency correction. The 2D E_{cm}-θ_{cm} histograms are then projected to 1D to generate the energy spectra and the

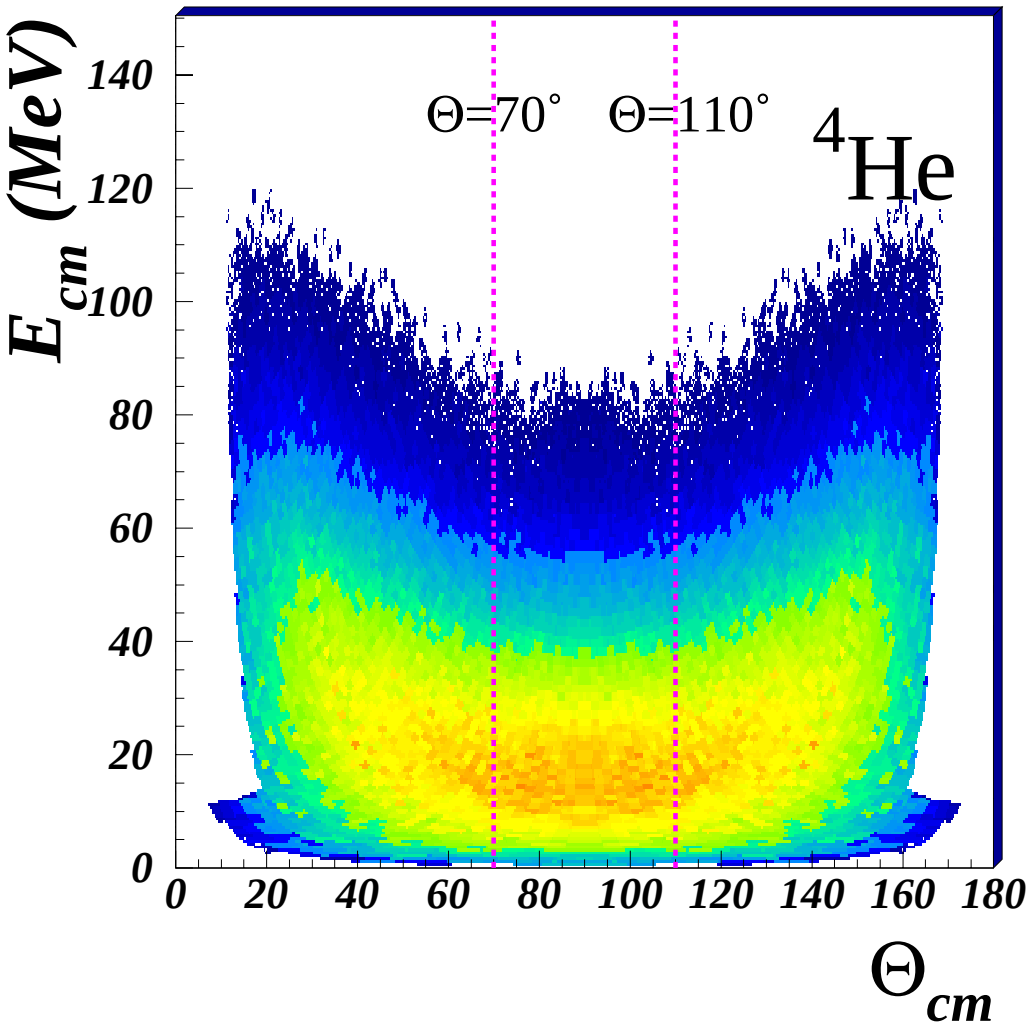

Figure 4.3: Corrected yield of ^{4}He produced in the central collisions for the ^{112}Sn + ^{112}Sn reaction

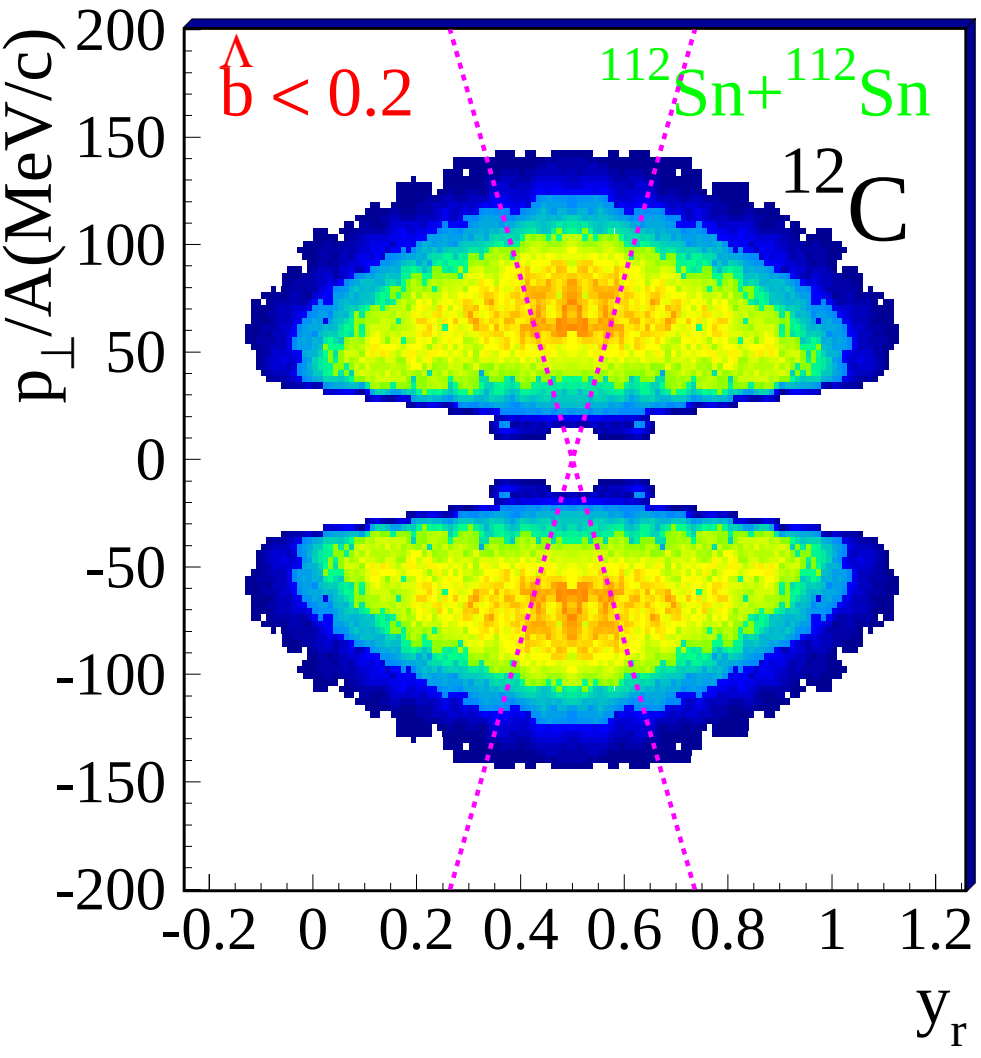

Figure 4.4: Efficiency corrected differential multiplicity $dM/dydp_\perp$ for ^{12}C fragments. The cut $70^\circ \leq \theta_{cm} \leq 110^\circ$ is indicated by the dashed lines in the figure.

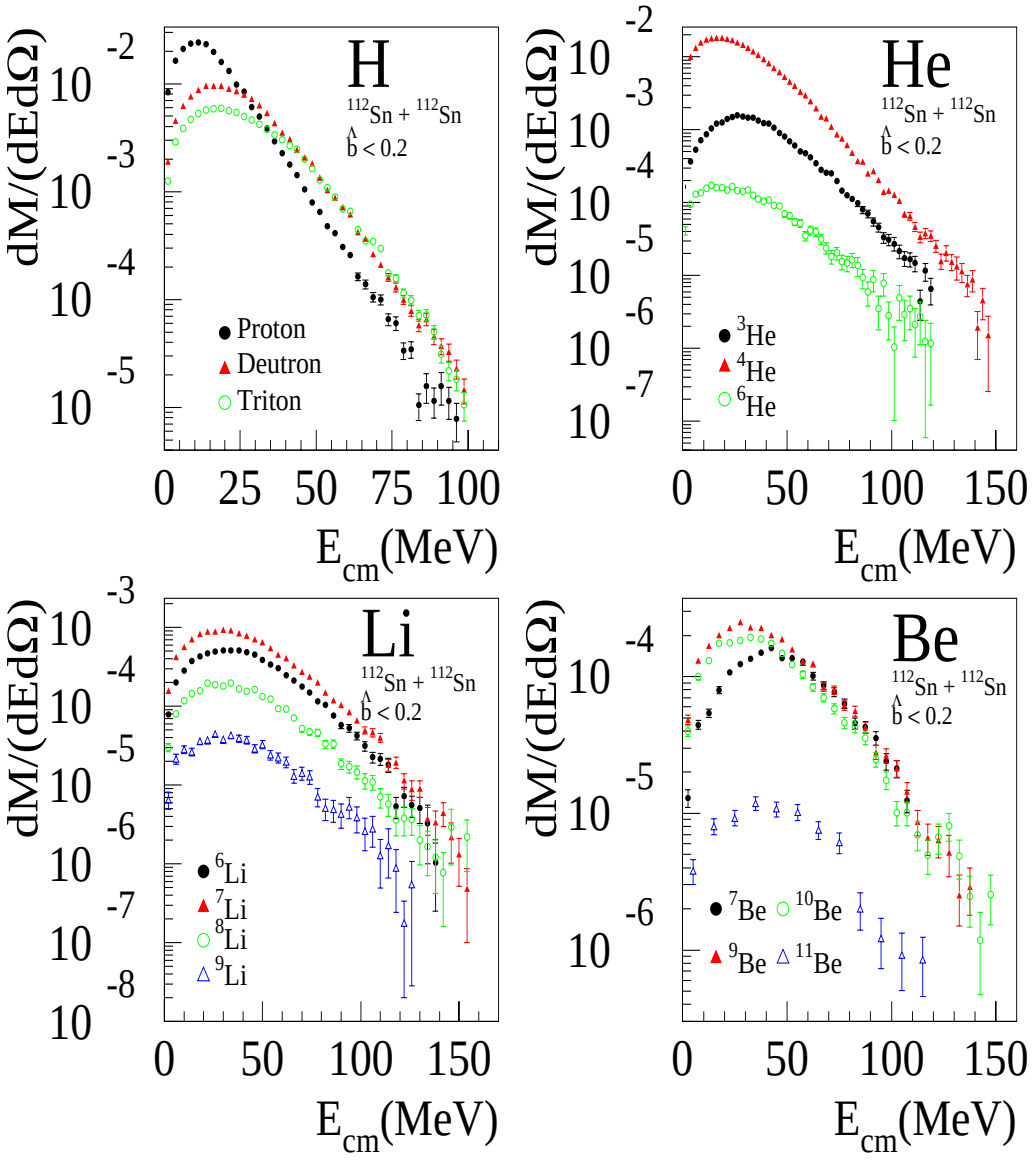

Figure 4.5: Energy spectra of H, He, Li, Be from the central collisions of the reaction ^{112}Sn+^{112}Sn. The energy spectra are obtained after the background subtraction and efficiency correction.

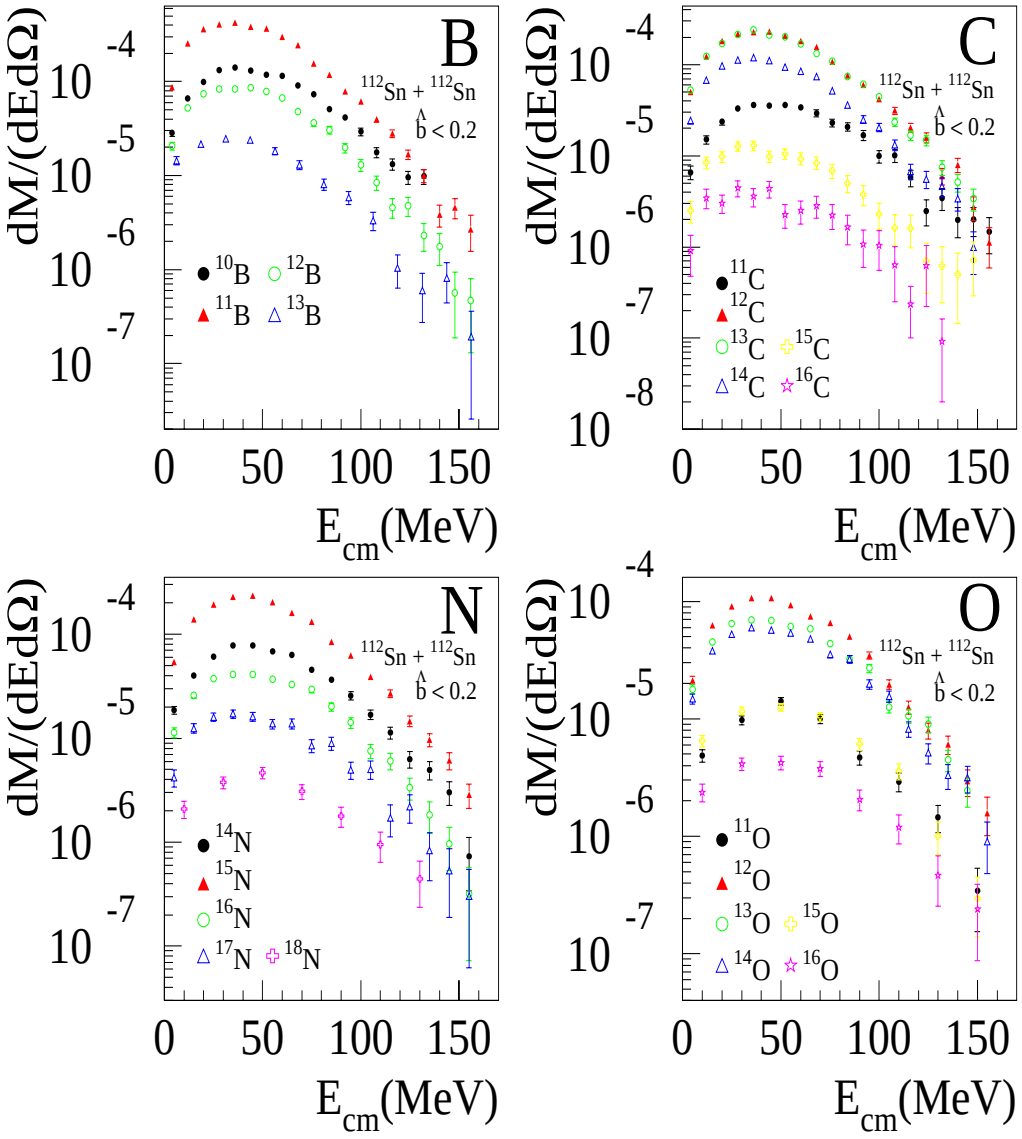

Figure 4.6: Energy spectra of B, C, N, O from the central collisions of the reaction ^{112}Sn+^{112}Sn. The energy spectra are obtained after the background subtraction and efficiency correction.

differential multiplicity. Fig. 4.5 and Fig. 4.6 present the differential multiplicities for the 35 isotopes we studied, from proton to ^{20}O, as a function of energy. We see that those energy spectra are very smooth within the energy and angular range selected. We can also see that the loss of the low energy and high energy particles is almost negligible.

Fig. 4.7 shows the measured average differential multiplicities of Li, Be, B, C, N and O isotopes at $70^\circ \leq \theta \leq 110^\circ$ as a function of $N - Z$, corresponds to the neutron excess of the nuclides. In this figure, the ^{112}Sn+^{112}Sn and ^{124}Sn+^{124}Sn data are shown by the solid squares and circles, respectively. The ^{112}Sn+^{124}Sn and ^{124}Sn+^{112}Sn are essentially equal: they have been averaged and are shown by the open diamonds. To show the isotopes in one figure, the yields of the B, C isotopes are offset by a factor of 10 and the yields of the N and O isotopes are offset by a factor of 100 in the figure. As expected, more neutron rich nuclides are produced by the neutron rich system, ^{124}Sn+^{124}Sn, while more proton rich nuclides are produced by the proton rich system, ^{112}Sn+^{112}Sn. The experimental results indicate that the multiplicities of IMF's are $\approx 10 - 20\%$ larger for the ^{124}Sn+^{124}Sn entrance channel than for the ^{112}Sn+^{112}Sn entrance channel, consistent with previous observations at an incident energy of 40MeV per nucleon [54]. The peaks of the distributions are always located at isotopes with $N = Z + 1$ for elements with odd values for Z, for all reactions. But for elements with even values for Z, the peak of the distribution located at $N > Z$ for ^{124}Sn+^{124}Sn and located at $N = Z$ for ^{112}Sn+^{112}Sn.

In general, the drop from the peak toward more proton-rich isotopes is rather steep especially for elements with even values for Z. The main differences between the isotope yields for the four different systems are observed in the tails of the isotope distributions, where it is greater than a factor of 4 for ^{20}O. Larger differences may be expected for even more exotic isotopes, but the background in the present

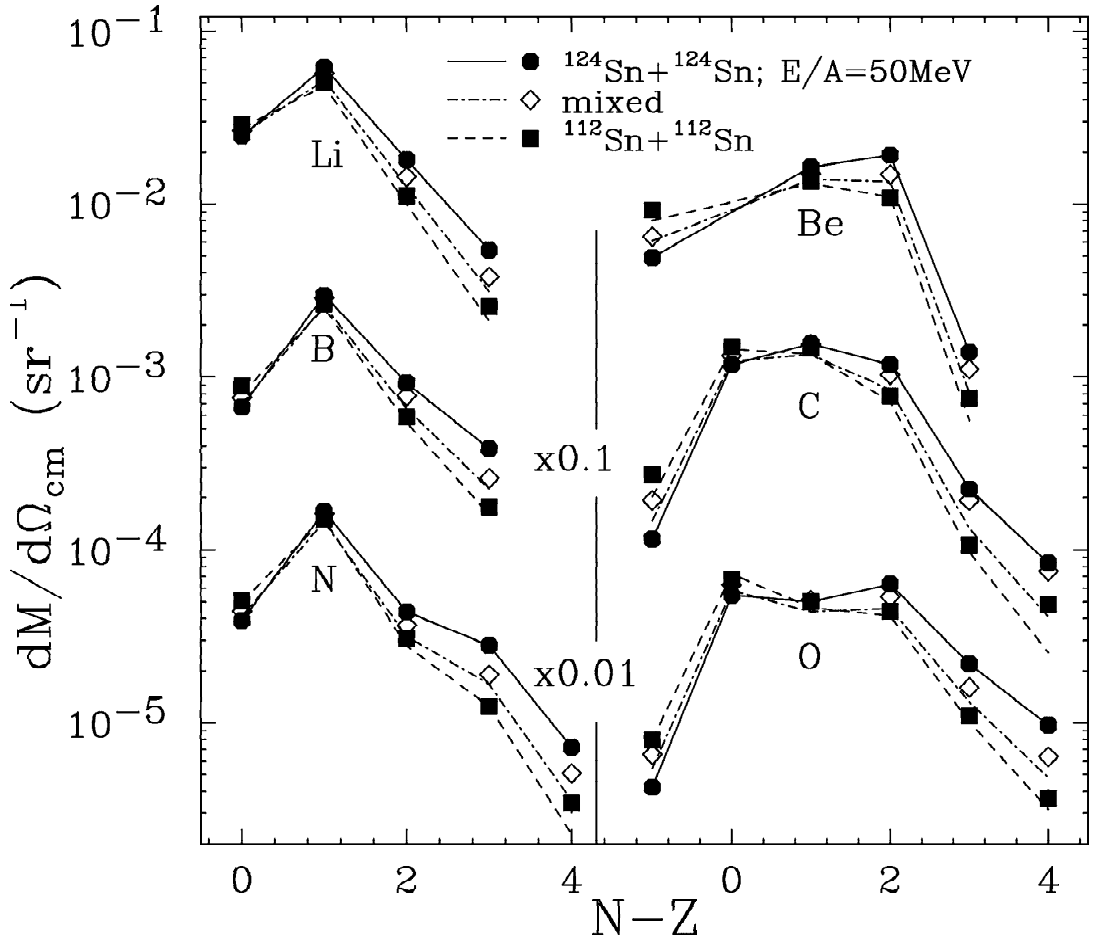

Figure 4.7: Average differential multiplicities at $70^\circ \leq \theta_{CM} \leq 110^\circ$ for Li, Be, B, C, N and O isotopes as a function of neutron excess $(N - Z)$ of the isotope. The solid points drawn by solid lines to guide the eyes are data for the ^{124}Sn+^{124}Sn system with N/Z=1.48. The open circles are data for the lightest system ^{124}Sn+^{124}Sn with N/Z=1.24. The open diamonds are the averaged values from the two mixed systems, ^{124}Sn+^{112}Sn and ^{112}Sn+^{124}Sn. The dashed and dot-dashed lines are predictions from Eq. 4.2. See text for more details.

measurement due to multiple hits in the LASSA telescopes does not allow for their accurate determination.

For multi-fragmentation which can be described by statistical fragment emission mechanisms, it was found that ratios of isotopic yields $R_{21}(N,Z)$=$Y_2(N,Z)/Y_1(N,Z)$ for a specific pair of reactions with different total isotopic composition, follow an isoscaling relationship [123, 110, 112]

$$R_{21}(N,Z) = \frac{Y_2(N,Z)}{Y_1(N,Z)} = Ce^{(\alpha N+\beta Z)} \ . \tag{4.2}$$

Here, C is an overall normalization factor, α and β are the isoscaling parameters for the chosen pair of reactions. This parameterization is discussed in greater detail within the isosaling section below. If we adopt the convention that reaction 2 is more neutron-rich than reaction 1, one expects α to be positive and β to be negative. We have adopted that convention here and have fitted the ratios of the isotopic yields for these four systems to extract the corresponding values for α and β. These values for α and β are given in Table 4.1.

Reaction 2	Reaction 1	α	β
^{112}Sn+^{124}Sn	^{112}Sn+^{112}Sn	0.18±0.01	-0.19±0.01
^{124}Sn+^{124}Sn	^{112}Sn+^{112}Sn	0.36±0.02	-0.39±0.01

Table 4.1: Values for α and β obtained from fitting the isotope ratios R_{21}.

Eq. 4.2, with only three parameters, C, α and β can be used to predict the isotope yields of ^{112}Sn + ^{112}Sn as well as the mixed system, ^{112}Sn + ^{124}Sn or ^{124}Sn + ^{112}Sn systems using the measured yields of one system. To illustrate how well this parameterization relates the yields of these four systems, we take the yields of the ^{124}Sn + ^{124}Sn system as a reference and use those yields and the fitted values of α

and β to predict the yields for the other four systems. The dash and dot-dashed lines in Fig. 4.7 are the calculated yields for ^{112}Sn + ^{112}Sn and ^{112}Sn + ^{124}Sn, respectively. These isoscaling parameters can, for this limited range of asymmetry, be described by a linear dependence on either the initial N/Z or the asymmetry parameter, $\delta = \frac{N-Z}{N+Z}$ of the reactions [112]. The excellent agreement between the predicted yields and the data suggests that such scaling law extrapolations may have useful predictive power. For example, we expect that these scaling predictions can be accurately extrapolated to other mass-symmetric systems of A=200-250 nucleons at the same incident energy per nucleon but with very different isospin asymmetry.

4.2.2 Models for the Multiplicity Calculation

Now we turn to the theoretical interpretation of the central collision data. To study the density dependence of the asymmetry term of the EOS, we adopt the viewpoint of the Stochastic Mean Field (SMF) approach described in refs. [2, 23]. In this approach, the time evolution of the nuclear density is calculated by taking into account both the average phase-space trajectory predicted by the Boltzmann-Northeim-Vlasov equation and the fluctuations of the individual collision trajectories about this average that can be predicted by equations of the Boltzmann-Langevin type. Both the introduction of fluctuating forces and the inclusion of numerical noise have alternatively been utilized in modeling the fluctuations in practical solutions to such equations; the simulations presented here utilize the latter technique.

The virtue of such a dynamical approach for the study of isotopic effects lies in its self-consistency. The flow of neutrons and protons is calculated under the influence of Coulomb and asymmetry terms, which reflect self-consistently the motion of these nucleons. Several different density dependences of the asymmetry term were explored. Here, we present results for two different asymmetry terms. In both cases,

the asymmetry term is approximated by the form

$$E_{sym}\left(\rho,\delta\right)=S\left(\rho\right)\delta^{2}\ , \tag{4.3}$$

where for the asymmetry term with a stronger density dependence

$$S(\rho)=a(\frac{\rho}{\rho_0})^{2/3}+b\frac{2(\rho/\rho_0)^2}{1+(\rho/\rho_0)}\ . \tag{4.4}$$

Here, ρ is the physical and ρ_0 is the saturation density, a=13.4 MeV, b=19 MeV [58, 64, 85]. In the following, we refer to this as the "super stiff" asymmetry term. For the asymmetry term with the weaker density dependence,

$$S(\rho)=a(\frac{\rho}{\rho_0})^{2/3}+240.9\rho-819.1\rho^2\ , \tag{4.5}$$

where a=12.7 MeV [23]. In the following, we refer to this as the "soft" asymmetry term. In Fig. 4.8, it can be seen that the two expressions are nearly equal at saturation density but differ at densities that are either much larger or smaller that ρ_0. In addition to the asymmetry term, the nuclear mean field has a Skyrme type isoscaler mean field with a soft equation of state for symmetric matter characterized by an incompressibility constant K=201 MeV. The isoscaler mean field and the asymmetry term of these equations of state are used for the construction of the initial ground state and for the time evolution of the collision. The nucleon-nucleon collisions by the residual interaction are calculated from an energy and angle dependent parameterization of the free nucleon-nucleon interactions and the isospin dependence of the Pauli-blocking is considered during these collisions.

The calculation solves the transport equations by evolving test particles of finite width. As mentioned above, we use a reduced number of test particles (50 test particles per nucleon) in the present calculations to inject numerical noise into the evolution. In test calculations, we alternatively employed the fluctuation mechanism discussed in ref. [23], which involves damping the numerical noise by utilizing a large

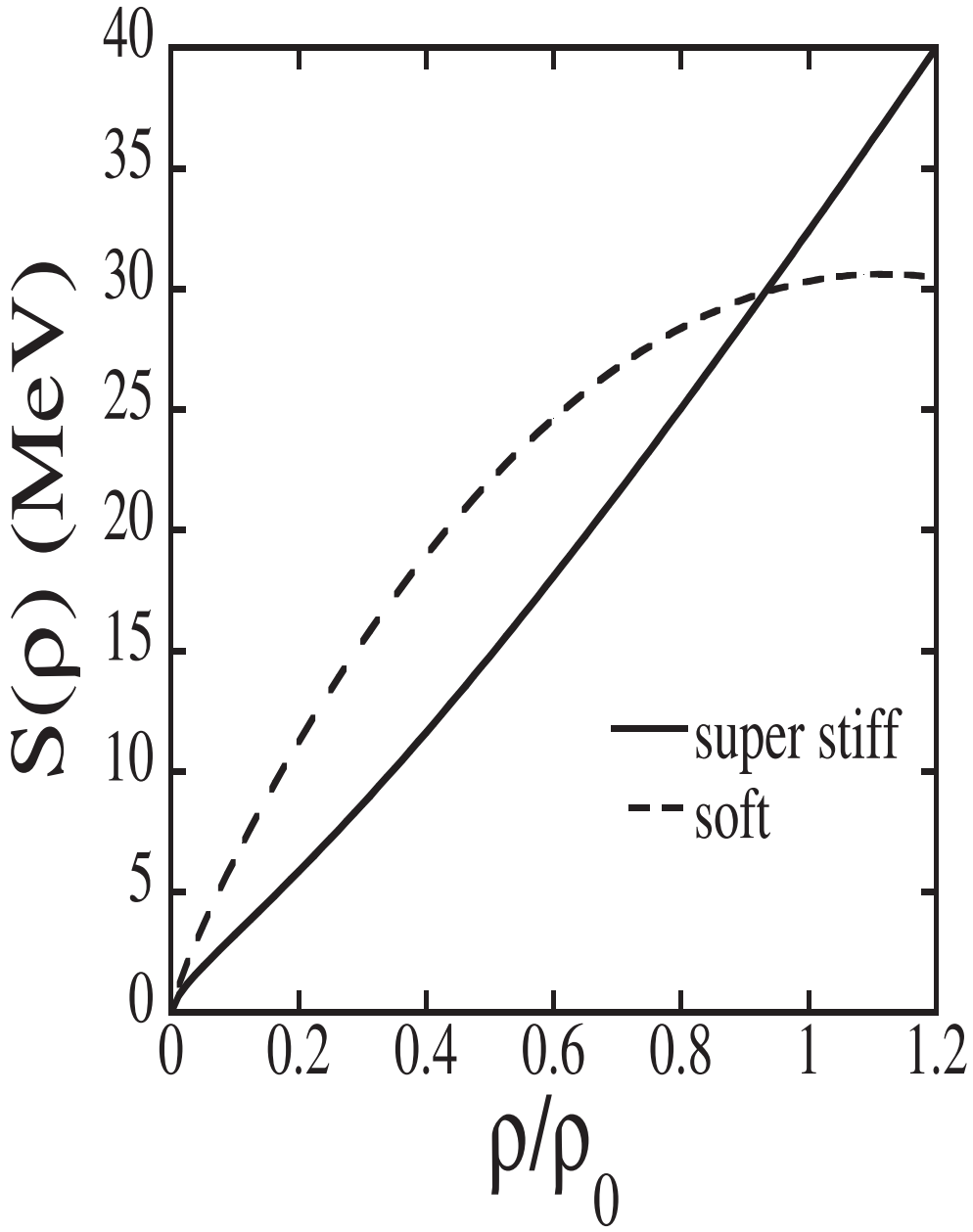

Figure 4.8: The solid curve and dashed curves indicate the density dependencies for the super stiff and soft asymmetry terms, respectively.

number of test particles and introducing explicitly physical noise according to thermal fluctuations. It was checked that both methods lead to similar results. In contrast to the Brownian one-body (BOB) method of ref. [44], these methods of inserting fluctuations are well suited to reactions at finite impact parameter because they do not presuppose knowledge of the most unstable modes.

When the system expands and reaches the spinodal instability (after about 110-120 fm/c), the most unstable modes are amplified and initiate the formation of fragments via spinodal decomposition. The evolution of the system is continued after spinodal decomposition until freeze-out where the number of dynamically produced fragments and their properties are finally determined. The system is decomposed into fragments using essentially a coalescence mechanism in coordinate space; specifically, fragments are defined by regions of density in the final distributions that are above a "cut-off" density of $1/8\rho_0$. By definition, the freeze-out time occurs when the average calculated number of fragments saturates. This occurs about 260 fm/c after initial contact of projectile and target nuclei in the present simulations. The excitation energy of the fragments is determined by calculating the thermal excitation energy in a local density approximation. The procedure is rather rough and will overestimate the excitation energy particularly for light fragments.

Some of the important features of these calculations and of the prior BUU-SMM [101] and EES [110] calculations can be understood simply by considering the influence of the density dependence of the asymmetry term on the relative emission rates of neutrons and protons. In all Sn+Sn collisions, the symmetry energy in the liquid drop model is positive, i.e. repulsive. The interaction contribution to the symmetry energy gives rise to a repulsive contribution to the mean field potential for neutrons and an attractive contribution to the mean field potential for protons. The mean field potential for an asymmetry term with stronger density dependence is larger at

high density and weaker at low density than that for an asymmetry term with weaker density dependence.

It is the low-density behavior that dominates the predictions for the isoscaling parameter. As the system expands and eventually multi-fragments, the prefragment remains at subnuclear densities for a long time while it is emitting nucleons. The asymmetry term with weaker density dependence around ρ_0 increases the difference between the neutron and proton emission rates leading to a more symmetric prefragment than is produced by calculations with the asymmetry term which has a stronger density dependence.

The SMF calculations are interesting because they are free, in principle, of arbitrary assumptions about whether the fragments are formed at the surfaces or from the bulk disintegration of the system. Comparisons between the fragmentation dynamics for different asymmetry terms were reported in ref. [107]. The trends of these calculations are consistent with the prefragment isospin dependences discussed above. In particular, fragments produced in calculations with an asymmetry term with strong density dependence tend to be more neutron-rich than the fragments produced in calculations with an asymmetry term with weak density dependence. In this respect, these predictions are similar to the results of the BUU-SMM calculations of ref. [101] and opposite to the results of the EES calculations of ref. [110].

However, the SMF fully dynamical formation of fragments should actually be more sensitive than the hybrid BUU-SMM to the interplay of the EOS, i.e. to the density dependence of the asymmetry term, with the fragmentation process. In the hybrid BUU-SMM calculations, the EOS is entering only in the "pre-equilibrium" nucleon emission described above. In the SMF approach, we have not only this isospin effect on fast particle emission but also the full dynamics of the isospin fractionation/distillation mechanism during the cluster formation. In a neutron-rich system,

this leads to a different N/Z "concentration" in the liquid phase (the fragments are more symmetric) and in the gas phase (nucleons and light ions, are more neutron-rich) [75, 3]. This effect is associated to the unstable behavior of dilute asymmetric nuclear matter and so in this way we have the chance of testing the EOS also at very low density.

Asymmetry terms with weaker density dependence around ρ_0 must show a faster increase at low densities and so a larger isospin fractionation/distillation during the fragment formation [4]. Therefore in a fully dynamical picture of fragmentation events a "soft" behavior of the asymmetry term around saturation density will enhance the formation of more symmetric fragments for two converging reasons: i) A larger "preequilibrium" neutron emission rate as discussed before; ii) A stronger isospin fractionation/distillation during the bulk disintegration. Opposite effects are of course predicted for a rapidly increasing ("stiff") asymmetry term around ρ_0. In this sense we can expect the SMF results to be more sensitive to the isospin dependences of the EOS at sub-saturation density.

At freezeout, the fragments are highly excited. For simplicity, we assume that the de-excitation of these fragments can be calculated as if the fragments are isolated. For this de-excitation stage, we have tabulated the known masses, states, spins, isospins and branching ratios for nuclei with $Z \leq 15$. Where experimental information is complete, it is used. Alternatively, empirical level density expressions are used for the discrete levels. These discrete levels are matched to continuum level density expressions as described in ref. [103]. The decay of primary fragments with $Z \geq 15$ are calculated, following ref. [103], using known branching ratios, when available, and using the Hauser-Feshbach formalism when the information is lacking. The decays of heavier nuclei are calculated using the Gemini statistical decay code [103, 20].

While the SMF calculations predict the numbers and properties of the hot frag-

ments that are produced at breakup, the predictions for the relative abundances of light clusters such as the isotopes with Z=1-2 that are emitted before the system expands to sub-nuclear density are not very realistic. This prevents a precise modeling of complete events including their detection efficiency and means that the impact parameter selection based on multiplicity cannot be imposed straightforwardly on the calculated events as on the data. This and the considerable numerical effort it requires have persuaded us to limit our comparisons to calculations composed of 600 events for each of the ^{112}Sn+^{112}Sn and ^{124}Sn+^{124}Sn reactions at a fixed impact parameter of b=2fm. We note, however, that the widths in the multiplicity distributions at fixed impact parameter are large enough that a range of impact parameters may contribute significantly to the experimental data. Future calculations are necessary to assess quantitatively the importance of this impact parameter smearing.

4.2.3 Overall Behavior Predicted by the SMF Calculations

In Fig. 4.9, the solid circles and open squares in the left panel show the measured elemental multiplicities for $2 \leq Z \leq 8$ averaged over $70^\circ \leq \theta_{cm} \leq 110^\circ$ for ^{124}Sn+^{124}Sn and ^{112}Sn +^{112}Sn collisions, respectively. The right panels show the corresponding measured multiplicities as a function of the fragment mass. These averaged multiplicities were obtained by summing the isotopic multiplicities for $2 \leq Z \leq 8$.

The dashed lines denote the corresponding distributions of hot primary fragments calculated by the SMF model using the super stiff EOS. Due to the low total number of events, we averaged these calculations over a slightly larger angular interval of $60^\circ \leq \theta_{cm} \leq 120^\circ$. The solid lines show the multiplicities of cold fragments after secondary decay. The statistical uncertainties in these calculations are shown in the figure as vertical bars. The corresponding uncertainties in the data are smaller than the data points. If the angular integration was performed over the entire solid

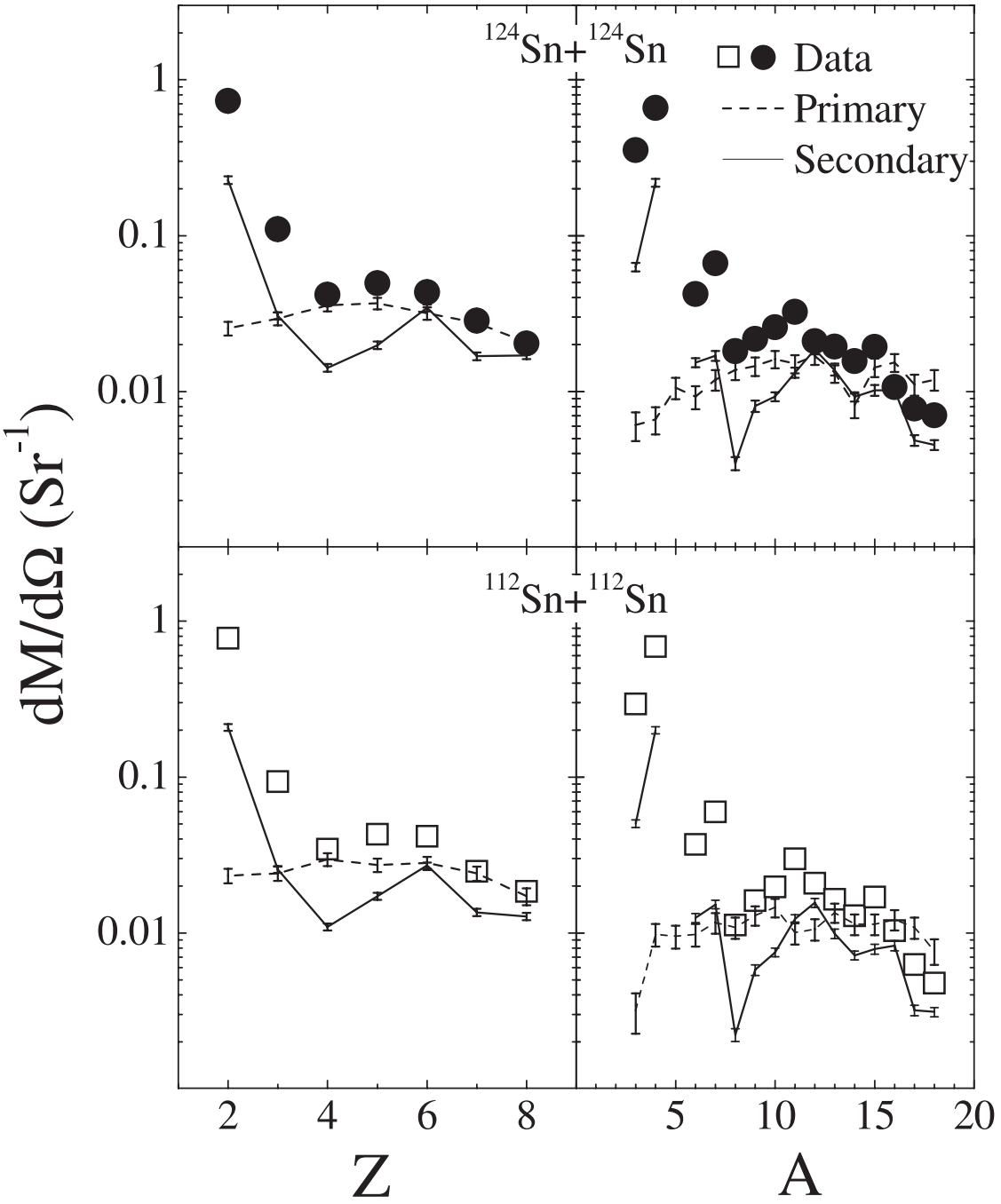

Figure 4.9: Differential multiplicities for ^{124}Sn+^{124}Sn collisions (upper panel) and ^{112}Sn+^{112}Sn collisions (lower panel) as a function of the fragment charge (left panels) and the fragment mass (right panels). The points are the data. The dashed and solid lines are the calculated primary and final fragment differential multiplicities, respectively. Statistical uncertainties are shown for the calculations; the corresponding uncertainties in the data are smaller than the data points.

angle, the averaged calculated multiplicities are about 20-30% larger. This difference reflects an anisotropy in the calculated primary angular distributions for the heavier fragments. In the present calculations, however, we do not have the capability to accurately calculate the modifications of the angular distribution due to secondary decay so we presently cannot explore this issue more quantitatively. As we will show later, this anisotropy has no impact on the shapes of the isotopic distributions for Z=3-8.

In general, the calculated primary and secondary fragment multiplicities are smaller than the measured values for the lighter fragments Z=3,4 and are somewhat closer to the measured values for Z=6-8. The lighter fragments with $Z < 4$ are mainly produced in secondary decay stage of the theoretical calculations; the primary yields of these light fragments are much smaller relative to the final yields than are the values for the heavier fragments. Because the fragment multiplicities and angular distributions depend on impact parameter, the comparison shown in Fig. 4.9 may be sensitive to the impact parameter ranges included in both calculation and data. Future calculations over a wide range of impact parameters are needed to address this issue. Concerning the greater discrepancy for Z=2-4 fragments, we have already noted that the formation of light clusters in the dynamical stage before breakup is not well described in BUU- and SMF-type simulations, because the unique structural properties of these fragments are not therein well treated. (Treatments of the emission of light clusters in coupled transport equations for nucleons and light clusters can be found in refs. [109, 29] and in the framework of FMD [35] or AMD [78] simulations.) On the other hand, there is a considerable emission of protons and neutrons during this stage; the total emission and consequently the asymmetry of the remaining source may still be realistic.

Now we turn to an examination of calculated isotopic yields. The upper left panel

of Fig. 4.10 shows the isotopes of carbon nuclei predicted by the SMF calculations over the entire angular range for ^{124}Sn+^{124}Sn (solid line) and ^{112}Sn+^{112}Sn (dashed line); the dotted-dashed and dotted lines show the corresponding calculations over the $60^\circ \leq \theta_{cm} \leq 120^\circ$ gate. Not surprisingly, the more neutron rich ^{124}Sn+^{124}Sn system preferentially produces the more neutron rich isotopes. The peak of the carbon primary distribution for the ^{124}Sn+^{124}Sn system occurs at about ^{15}C while the peak for ^{112}Sn+^{112}Sn system occurs at lower mass, i.e. somewhere between ^{13}C and ^{14}C. The differences between the angle gated and total primary yields are small, and these difference translate into negligible differences in the shape of the isotopic yield distribution after secondary decay; we therefore do not plot the gated data because the two curves are indistinguishable when normalized to each other. As the statistics of the present calculation make it difficult to perform comparisons to isotopic yields with a $60^\circ \leq \theta_{cm} \leq 120^\circ$ gate imposed on the calculation, the remaining calculated multiplicities are integrated over the entire solid angle.

After sequential decays, one obtains the secondary distributions shown in the lower left panel. No longer is there a noticeable difference between the peak locations (at ^{12}C in both systems); instead, the main differences are found in the shape of the distribution, which is higher in the neutron-rich isotopes and lower in the neutron-deficient isotopes for the ^{124}Sn+^{124}Sn system than it is for the ^{112}Sn+^{112}Sn system. Such trends are also qualitatively observed in the experimental data shown for the ^{124}Sn+^{124}Sn system by the solid circles and for the ^{112}Sn+^{112}Sn system by the open squares in the lower left panel. However, the experimental distributions are considerably wider and more neutron rich than the model predictions. This trend is replicated in the elemental distributions for all of the other measured elements.

Another way to quantify the differences in the isotope distributions is by the asymmetry parameter $\delta = (N - Z)/(N + Z)$. The average asymmetry $< \delta >$ of the

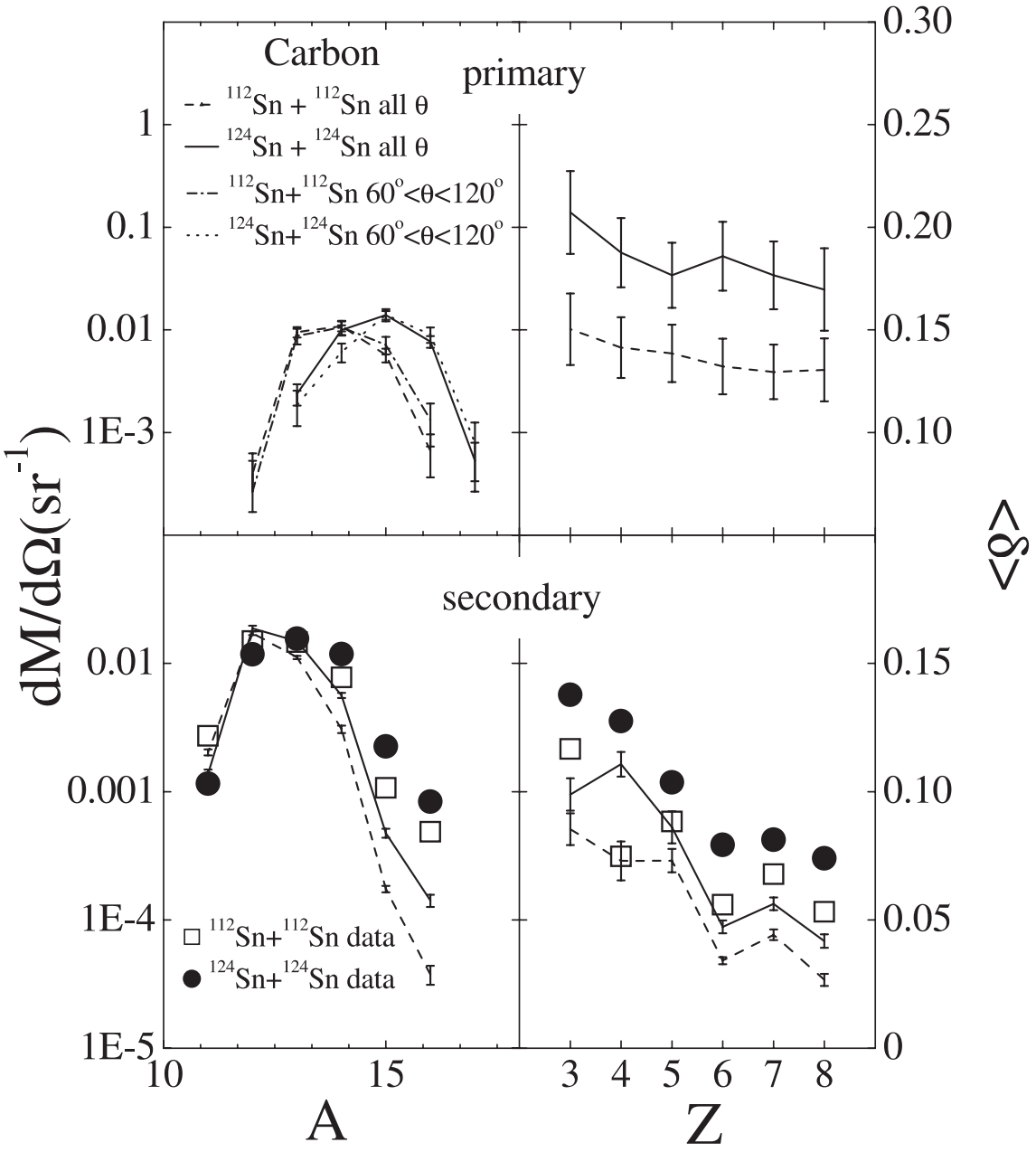

Figure 4.10: Left panels: Calculated primary (upper panel), calculated final (lower panel) and measured (lower panel) carbon isotopic yields for Sn+Sn collisions. Right panels: Calculated primary (upper panel), calculated final (lower panel) and measured (lower panel) mean isospin asymmetries as a function of the fragment charge for Sn+Sn collisions. The lines and data points are further explained in the text.

isotopic distribution for each element is shown as a function of Z in the right panels of Fig. 4.10. Following the same convention as in the left panels, the solid and dashed lines show the average asymmetries for ^{124}Sn+^{124}Sn and ^{112}Sn+^{112}Sn collisions; the upper and lower panels present results for the primary and secondary fragment distributions, respectively. The calculated differences between the two systems are more pronounced prior to secondary decay than afterwards. The corresponding data, shown for the ^{124}Sn+^{124}Sn system by the solid circles and for the ^{112}Sn+^{112}Sn system by the open squares in the lower right panel, are larger and display a stronger dependence on the asymmetry of the system than do the final calculated fragment yields after secondary decay.

4.2.4 Isoscaling Analyses

A more sensitive way to compare isotopic distributions is to construct the isotopic ratio $R_{21}(N,Z)$=$Y_2(N,Z)/Y_1(N,Z)$ from the isotope yields $Y_i(N,Z)$ with neutron number N and proton number Z from two different reactions. As discussed in the experimental section, $R_{21}(N,Z)$ obeys a simple relationship $R_{21}(N,Z) = \ C\, e^{\alpha N+\beta Z}$ where C is an overall normalization factor and α and β are isoscaling parameters [101, 110, 123, 112] . Such an isoscaling relationship can be obtained in statistical theories for two systems that are at the same temperature when they produce fragments. Binding energy factors common to the yields for the fragments in each system are cancelled by the ratio when the temperatures are equal, leaving terms related to the chemical potentials or separation energies [110]. In grand canonical models of multifragmentation, $\alpha = \Delta\mu_p/T$ and $\beta = \Delta\mu_n/T$ for example, where $\Delta\mu_n$ and $\Delta\mu_n$ are the differences in the chemical potentials for the neutrons and protons in the two systems and T is the temperature [123, 112]. In some calculations [112], the values for the isoscaling parameters extracted from equilibrium multifragmentation models are

similar before and after sequential decays, an observation that has been attributed to a partial cancellation of secondary decay effects [123, 112].

While isoscaling can be expected for many statistical processes [101, 110, 123, 112] , the question of whether it can be expected for specific dynamical calculations remains open. To investigate whether the SMF dynamical model displays isoscaling, we construct the relative isotope ratios, R_{21}, primary, using the primary fragments produced in ^{124}Sn+^{124}Sn collisions as reaction 2 (numerator) and in ^{112}Sn+^{112}Sn collisions as reaction 1 (denominator).

The results are shown in the upper panel of Fig. 4.11. The error bars reflect the statistical uncertainties. The predicted isotope ratios for these primary fragments depend very strongly on the neutron number and follow trends that appear consistent with isoscaling relationship defined by Eq. 4.2. The uncertainties are large reflecting the low statistics of the simulations, but the strong dependence on neutron number makes it possible to discern apparent isoscaling trends nonetheless. The lines are best fits using Eq. 4.2 resulting in $C = 0.96$, $\alpha = 1.07$ and $\beta = -1.43$. These values for a are much larger than values observed in the experiment. The lower panel provides the corresponding SMF predictions for the ratios, R_{21}, final, of the yields of particle stable nuclei after secondary decay. For comparison purposes, the ordinates of the top and bottom panels are chosen to be the same; this demonstrates graphically that the trends of the final isotope ratios are much flatter and the corresponding isoscaling parameters ($\alpha = 0.286$ and $\beta = -0.288$) are much smaller. Clearly, the isoscaling parameters predicted by dynamic SMF calculations are strongly modified by secondary data. This trend is very different from some equilibrium statistical models for multifragmentation where the isoscaling parameters have been predicted to be insensitive to secondary decay [123, 112].

The isoscaling behavior of the dynamically produced fragments arises not from

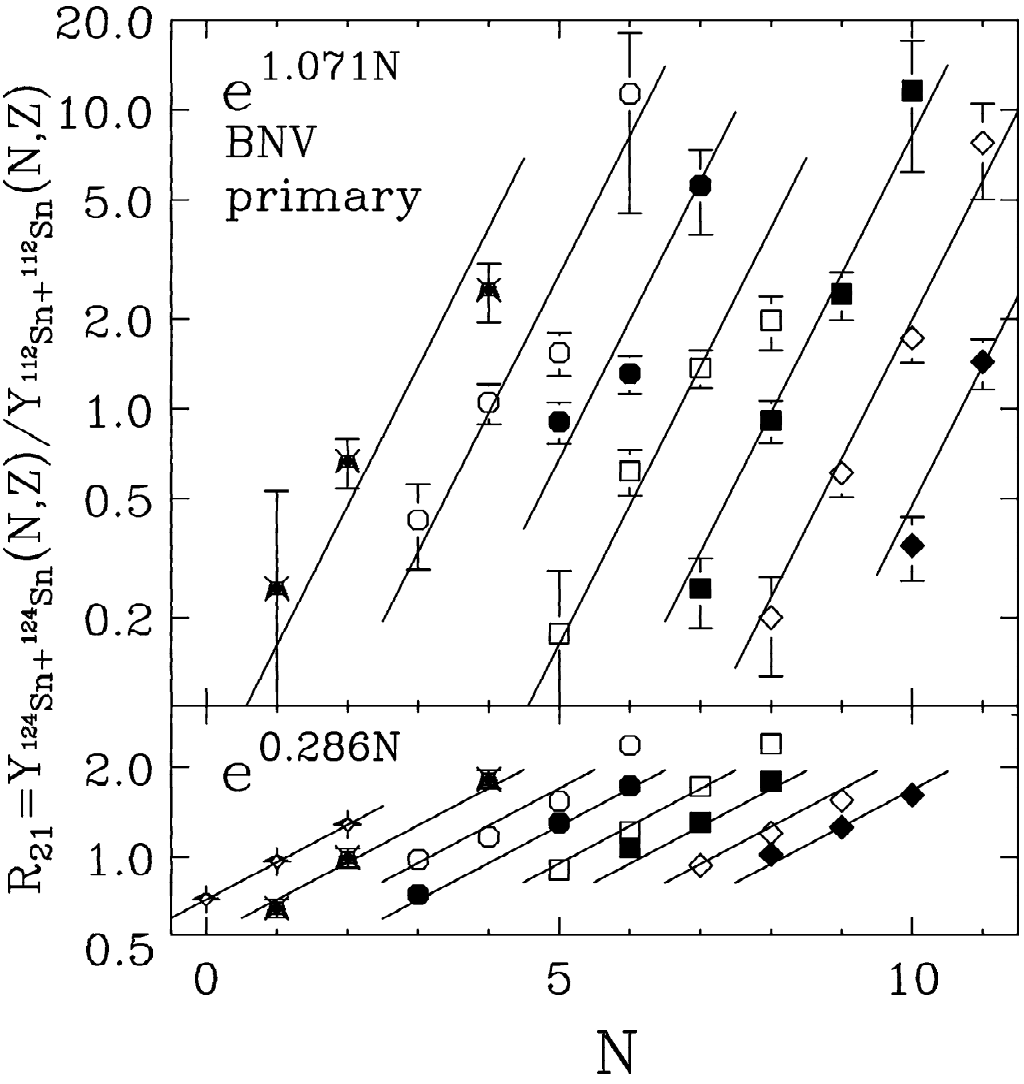

Figure 4.11: Upper panel: R_{21} values obtained from the ratios of the primary isotopic distributions for ^{124}Sn+^{124}Sn collisions divided by those for ^{112}Sn+^{112}Sn collisions. Lower panel: Corresponding R_{21} values obtained from the ratios of the final isotopic distributions. Each line in the two panels corresponds to ratios for a given element. Elements with Z=2-8 (Z=1-8) are represented from left to right in the upper (lower) panel. The lines are the result of fitting R_{21} with Eq. 4.2; the dependencies on neutron number for the best fits are given in each panel.

thermal physics but rather from some special characteristics of the SMF primary distributions predicted for these reactions. We find, for example, the SMF primary isotopic and isotonic distributions can be roughly described by Gaussians, see Fig. 4.9. Isotopic distributions, for example, can be described by

$$Y\left(N,Z\right)=f(Z)\exp\left[-\frac{\left(N-\overline{N}\left(Z\right)\right)^{2}}{2\sigma_{Z}^{2}}\right]\ , \tag{4.6}$$

where $\overline{N}\left(Z\right)$ is the centroid of the distribution and σ_{Z}^{2} describes the width of the distribution for each for each element of charge Z. This leads to an exponential behavior of the ratio R_{21}, since, neglecting quadratic terms in $\overline{N}$,

$$\ln R_{21}=\frac{1}{\sigma_{Z}^{2}}\left[\overline{N}\left(Z\right)_{2}-\overline{N}\left(Z\right)_{1}\right]N\ . \tag{4.7}$$

Note Eq. (4.7) requires the values for σ_{Z}^{2} to be approximately the same for both reactions. We have observed this to be the case for our SMF calculations of Sn+Sn collisions (to within the statistical accuracy $\sim$10%). For the ratios for every element, to be optimally described by the same parameter, the ratio $\left[\overline{N}\left(Z\right)_{2}-\overline{N}\left(Z\right)_{1}\right]/\sigma_{Z}$ must be independent of Z. The statistics of the calculation do not allow a detailed test of this assumption, but it does appear that this ratio increases somewhat with Z, as Fig. 4.11 suggests. The primary distributions therefore do not respect the isoscaling relationship as well the data do.

Now, at variance with the statistical fragmentation models, the secondary decays substantially modify the isoscaling parameter. The width σ_{Z}^{2} decreases due to secondary decay and the difference $\left[\overline{N}_{2}-\overline{N}_{1}\right]$ like ways decreases fractionally, but by a larger amount. Moreover, the final shape is no longer Gaussian, but due to secondary decay, it reflects the binding energy as a function of neutron excess more strongly (see Fig. 4.10). These changes combine to decrease the isoscaling parameter as shown in the lower panel of Fig. 4.11.

4.2.5 Sensitivity of the SMF Calculations to the Asymmetry Term

The density dependence of the asymmetry term has a significant influence on the relative emission rates of the neutrons and protons and, consequently, on the isospin asymmetry of the hot fragments prior to secondary decay. As discussed previously, an asymmetry term with weaker density dependence tends to remain more important at lower densities, driving the fragments closer to isospin symmetry, than does an asymmetry term with stronger density dependence. Consistent with this general consideration, the calculated primary isotope distributions in ^{124}Sn+^{124}Sn collisions, shown in Fig. 4.12 for carbon (upper left panel) and oxygen (upper right panel), are more neutron-rich for the super stiff asymmetry term (solid line) than they are for the soft asymmetry term (dashed line). A similar trend is also predicted for the ^{112}Sn+^{112}Sn system, but is not shown in the interest of brevity.

A similar trend is observed in the corresponding final distributions that are obtained after secondary decay and shown in the middle panel with the same convention for the solid and dashed lines as in the upper panel. Both secondary distributions calculated for super stiff and soft asymmetry terms, however, are significantly narrower and more proton-rich than the experimental distributions shown by the closed circles in the figure. (The lower panels, which display corresponding calculations when the excitation energy is reduced by 50%, will be discussed in the next section.) Similar trends are also observed for the ^{112}Sn+^{112}Sn and for the other elements with $3 \leq Z \leq 8$, though we do not for brevity's sake show those results.

In Fig. 4.13, we present the related dependence of the SMF predictions for the isotope ratios R_{21} upon the density dependence of the asymmetry term. We take advantage of the fact that the results in the Fig. 4.11 can be compactly displayed by the scaled function $S(N) = R_{21}(N,Z) \cdot e^{-\beta Z}$ which condenses the isotopic dependence

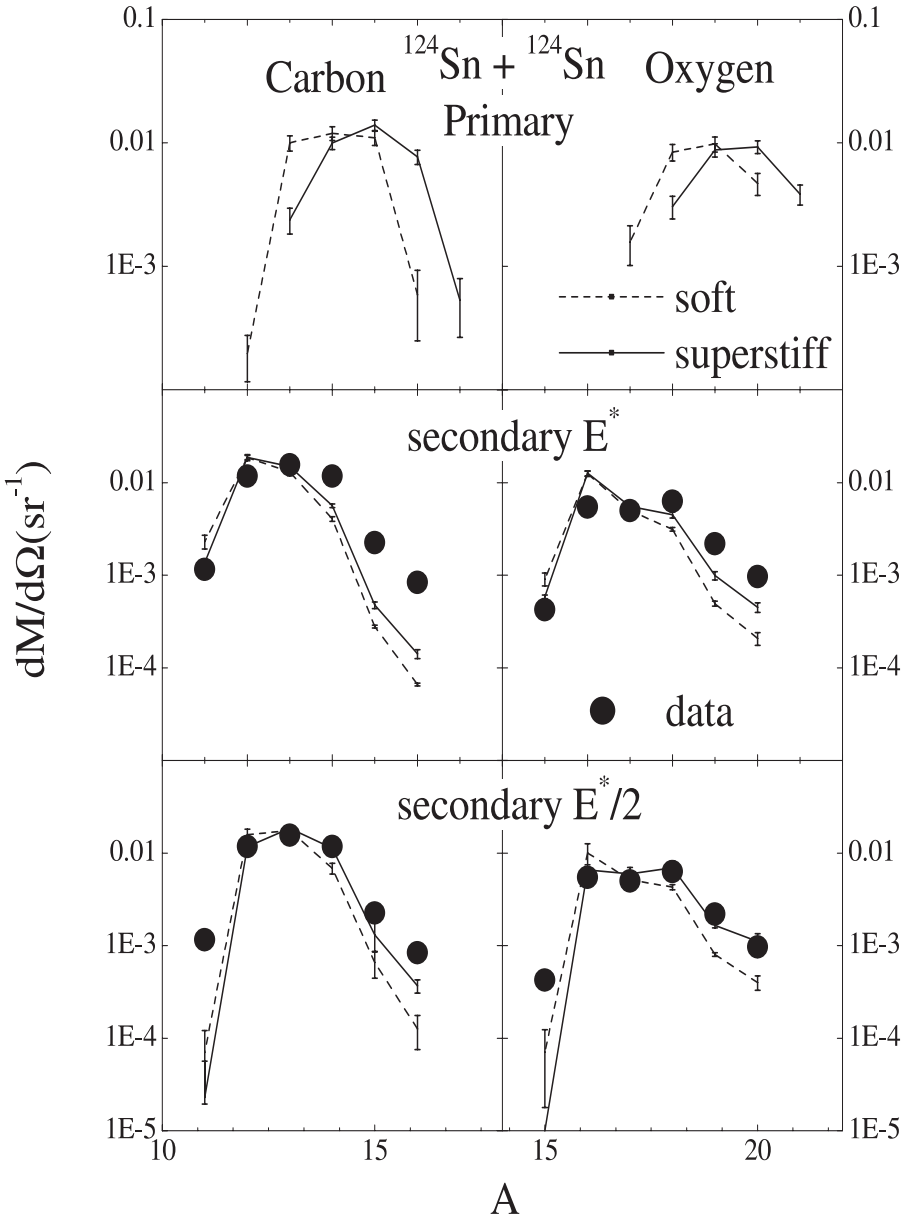

Figure 4.12: Upper panel: Dependence of the primary distributions for carbon(left panel) and oxygen (right panel) upon the density dependence of the asymmetry term. Middle panel: Dependence of the final distributions for carbon (left panel) and oxygen (right panel) upon the density dependence of the asymmetry term. The data are also shown as the solid points. The various lines in the figure are described in the text. The excitation energies for the fragments are taken directly from the SMF calculations. Lower panel: The data are the same as in the middle panels. The curves are the calculations obtained when the excitation energies of the primary fragments are reduced by a factor of two.

for the various elements onto a single line [110]. The left panel in Fig. 4.13 shows the results for the super stiff asymmetry term and the right panel shows the results for the soft asymmetry term. In each panel, the values for $S(N)$ obtained from the primary distribution are shown by the symbols clustered about the solid lines, the results obtained from the secondary distribution are shown by the symbols clustered about the dashed lines and the results from the data are shown by the dotted-dashed lines in each panel to provide a reference. Both the primary and secondary values for $S(N)$ have been fit by exponential functions to obtain corresponding values for the scaling parameter and these values are given in the figure.

Generally, the primary distributions for both equations of state display a much stronger dependence on neutron number than do the final isotopic distributions and the data. However, the influence on the isoscaling parameter is statistically not very significant. Indeed, as we pass from a "stiff" asymmetry term to a "soft" one, we do have a stronger isospin fractionation/distillation, as already discussed before. The centroid of the distribution, $\overline{N}_2$, decreases (see Fig. 4.12) but also the width σ_Z^2 decreases; the decrease in width, however, is of the order of 10% and comparable to its statistical uncertainty. The calculated final distributions display a weak sensitivity to the density dependence of the asymmetry term; the values for (α=0.286) obtained for the super stiff asymmetry term are larger than the values for (α=0.254) obtained for the soft asymmetry term. The sensitivity to the asymmetry term is considerably less than that reported for the EES model [110], and for the BUU-SMM hybrid calculations [101]. Unlike these latter two calculations, both super stiff and soft asymmetry terms yield alpha values that are significantly lower than the value extrapolated from the data (α=0.36). One should note, however, that the excitation energies of these latter calculations could be more freely varied to achieve better agreement with the experimental observations.

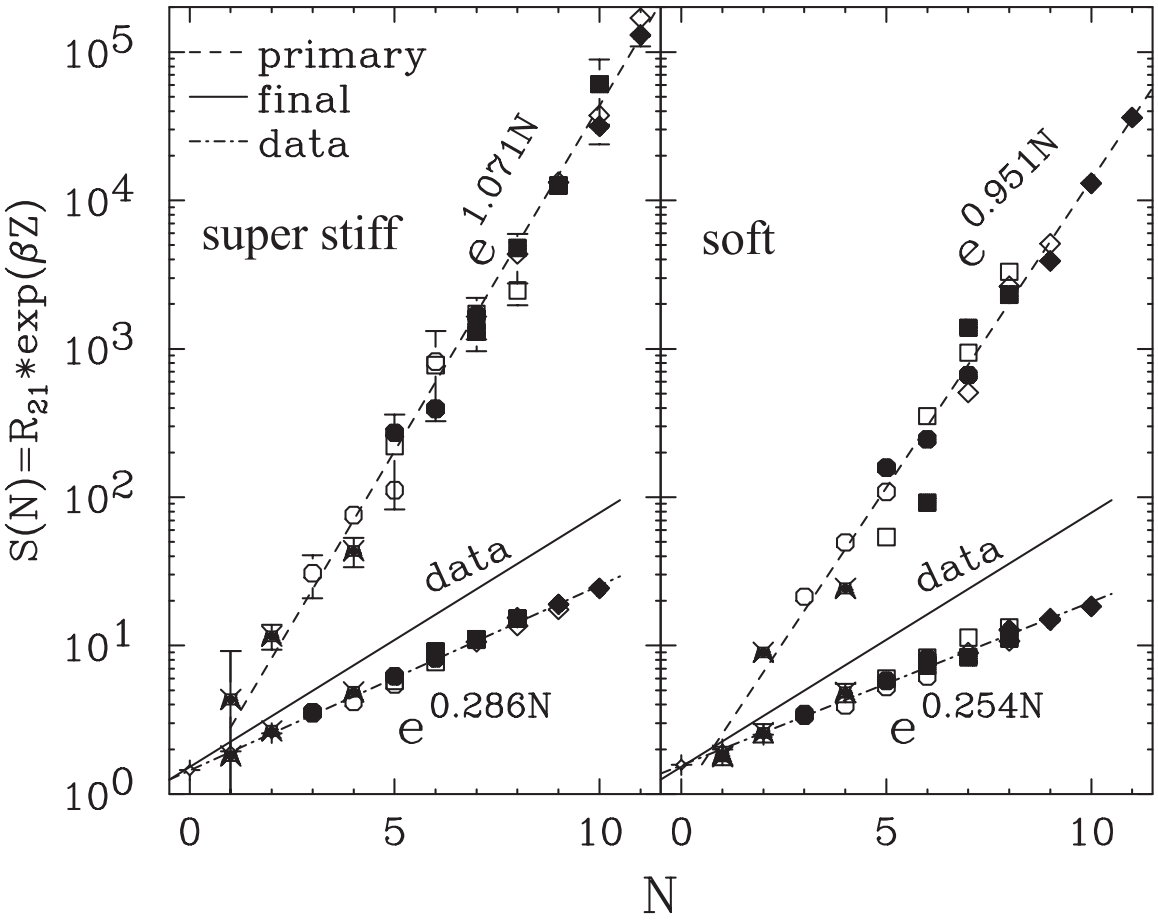

Figure 4.13: Dependence of the scaled function S(N) on the density dependence of the asymmetry term. The left panel provides a comparison between values for S(N) computed from the data (dashed line) and the calculated primary (points about solid line) and final (points about dashed-dotted line) distributions obtained for the super stiff asymmetry term. The right panel provides a comparison between values for S(N) computed from the data and the calculated primary and final distributions obtained for the soft asymmetry term.

4.2.6 Discussion of the Isotope Multiplicity and SMF Calculations

The calculated final isotopic distributions for both asymmetry terms differ from the measured ones in three respects: (1) they are narrower; (2) they are more neutron deficient; and (3) they show a weaker dependence on the isotopic asymmetry of the total system. In these respects, the calculated results for the two different asymmetry terms are more similar to each other than they are to the data. It is probably premature at this stage to focus attention on the sensitivity of the predicted final distributions to the asymmetry term. Instead, let us concentrate upon what may be required to bring the final isotopic distributions into greater concordance with the measurements.

The tendencies of the final isotopic distributions to be more neutron deficient and to display a weaker dependence on the isotopic asymmetry of the system are probably closely related. When the final isotopic distributions for both systems are too neutron deficient, there is not very much room for a strong dependence on the isotopic asymmetry of the system. The problem that the final isotopic distributions are too neutron deficient can either be that the primary distributions were too neutron deficient, that the secondary decay removed too many neutrons or that the freezeout assumption is invalid.

First let us consider whether initial isotopic distributions may be too neutron deficient. We note that the average isospin asymmetry of the initial distributions is trivially related by charge and mass conservation to the average isospin asymmetry of the nucleons emitted during the SMF calculations before the freezeout (t=260 fm/c) chosen for these calculations. Clearly, it is important that complimentary measurements of the yields and energy spectra of light particles be performed to provide guidance as to whether these missing neutrons are carried away primary

during fast pre-equilibrium emission or slower evaporative emission. However, the present simulations neglect the emission of light clusters (d, t, ^{3}He, ^{4}He, ^{6}Li, ^{7}Li, etc.) during the dynamical evolution prior to the freezeout. Previous studies [29, 94, 92] have noted that the neglect of the emission of ^{4}He emission is particularly problematic because it is abundant and because each ^{4}He particle enhances the isospin asymmetry of the remaining system by removing four nucleons without changing the neutron excess. Indeed, it has been speculated that that ^{4}He emission may have an influence on the isospin asymmetry of the other clusters and fragments that is of the order magnitude of the influence of the mean field [29, 94, 92]. The treatment of light cluster emission clearly needs additional theoretical attention.

The number of neutrons removed by secondary decay depends primarily on the fragment excitation energies and the relative branching ratios for neutron and charged particle emission. There are significant uncertainties in the calculation of the excitation energies of the fragments, which are related to the difficulty to establishing precise their ground state binding energies. To explore the sensitivity of the results to the excitation energy, we have reduced the excitation energy of each fragment by a multiplicative factor f where $0.5 \leq f \leq 1$ and recalculated the final fragment isotopic distributions.

The solid and dashed lines in Fig. 4.12 for carbon fragments (lower left panel) and oxygen fragments (lower right panel) show the calculated final distributions for f=0.5 using super stiff and soft asymmetry terms, respectively. Clearly, it is possible by reducing the excitation energy to shift the isotope distribution in the direction of the more neutron-rich isotopes, so as to make the mean isospin asymmetry of the calculated final and measured distributions to be the same. However, the widths of the calculated final isotopic distributions will still be narrower than the measured ones.

This discrepancy between the theoretical and experimental widths would be reduced if the theoretical primary distributions were wider in their excitation energy distributions or their isotopic distributions or both. It is interesting that the primary distributions of equilibrium statistical model calculations that reproduce the experimental final distributions are much wider in excitation energy and neutron number than those predicted by the SMF calculations [97, 112]. Future investigations will be needed to address whether wider primary distributions in excitation energy or neutron number can be attained in the SMF model by altering some of the underlying model assumptions such as the manner in which they are defined at freezeout.

Increased widths may be achieved by performing calculations for a range of impact parameters rather than the single impact parameter b=2fm presented here. We note that the inclusion of larger impact parameter events may broaden the primary distributions at mid-rapidity because it will require the inclusion of fragments emitted from the neck joining projectile- and target-like residues. In ref. [4], it was shown that SMF calculations predict such "neck" fragments to be more neutron rich because the isospin fractionation/distillation effect is somewhat reduced in peripheral events, leaving more neutrons in the fragments, and there can also be an overall neutron enhancement in the neck region for such events due to the neutron skins of the projectile and target [4]. Moreover, the excitation energies of the primary fragments in more peripheral collisions are also somewhat reduced. Experiments also suggest that neck fragments in very-peripheral collisions are more neutron-rich [33], but there is little detailed experimental information about the impact dependence at smaller impact parameters. Combining more calculated peripheral events with the calculated central collision events presented in this thesis may result in the broader isotopic distributions that appear to be required by the data.

4.2.7 Energy Spectra and Equilibrium Models Calculation

The central events display many attributes consistent with bulk multifragmentation following expansion and spinodal decomposition at densities of $\rho \leq 1/3\rho_0$ [27, 70, 36]. The assumption of thermal equilibrium allows useful baseline predictions for the behavior of complex systems, even when equilibrium may not be fully achieved. For example, the yields of particles emitted in intermediate energy [27, 12], relativistic [120, 60] and ultra-relativistic [77] nuclear collisions have been successfully compared to equilibrium statistical ensembles. This success suggests the attainment of chemical equilibrium, allowing interpretations [76, 11, 116] of such data in terms of phase transitions in strongly interacting matter.

This interpretation assumes that systems must last long enough for the relevant degrees of freedom to equilibrate, and the observables being described reflect that equilibrium. Similar to the case for the early universe, observables related to these degrees of freedom may reflect a freezeout time after which these observable cease their evolution. Indeed, many observables in the central collisions of heavy ions have been successfully described by equilibrium calculations for an expanding system with an initial mass, charge, excitation energy and a freezeout density of $\rho \approx 1/6\rho_0 - 1/3\rho_0$ [27, 60, 11]. Unlike the early universe, however, the small size of these systems may allow particles to be emitted and decoupled from the surfaces of the system before the rest of the system has its freezeout. In this section, we show that the energy spectra of isotopically resolved fragments allow one to observe such effects and quantify the breakdown of the freezeout approximation.

The expected properties for the energy sprectra of fragments from the disassembly of thermalized freezeout configuration are straightforward. Because nuclear interactions between particles are assumed to be negligible after freezeout, the observed mean kinetic energies of particles $< E_k >$ reflect the thermal kinetic energy $3/2T$,

the collective velocity v_{coll} at freezeout and the energy $< E_{Coul} >$ gained due to the accelerations of these particles by the Coulomb field of the remaining system [70, 50, 48]:

$$< E_k > \approx \frac{3}{2}T + \frac{1}{2}Am_N < v_{coll}^2 > + < E_{Coul} > , \tag{4.8}$$

where Am_N is the mass of the fragment with A nucleons and m_N is the nucleon mass. As the Coulomb energy depends nearly linearly on the fragment charge and for light fragments, $Z/2$, Eq. 4.8 suggests a roughly monotonic dependence of $< E_k >$ upon A; this has been used previously to extract values for the collective expansion velocity v_{coll} after constraining $< E_{Coul} >$ with assumptions about the breakup density [70, 50, 48].

Because E_{Coul} depends on Z while the collective motion term depends on A, Eq. 4.8 may permit experimental distinctions between the two terms. To minimize sensitivity to the Coulomb effects, for example, one can compare the isotope mean energy for each element. Such studies have been performed for light charge particles $Z \leq 2$. These studies show mean energies for ^{3}He that are higher than those for ^{4}He, contrary to Eq. 4.8 [122, 115], suggesting the emission of ^{3}He particles from the surface of the emitting source rather than from an equilibrated freezeout. Since many of the light charged particles such as ^{3}He are strongly emitted before the fragments, the question of whether fragments originate in a thermalized freezeout remains open. To answer this question, one must measure the isotope energy spectra for fragments heavier than He.

In Fig. 4.14, we show the energy spectra for ^{11}C (open circles) and ^{12}C (closed circles). The yield of ^{12}C yield is nearly a factor of 10 higher than that for ^{11}C due to its higher binding energy. The peak in the energy spectrum occurs at higher energies for ^{11}C than for ^{12}C and is broader. These two factors dictate a higher mean energy for ^{11}C than for ^{12}C.

The measured mean energies of all the isotopes as a function of the mass number

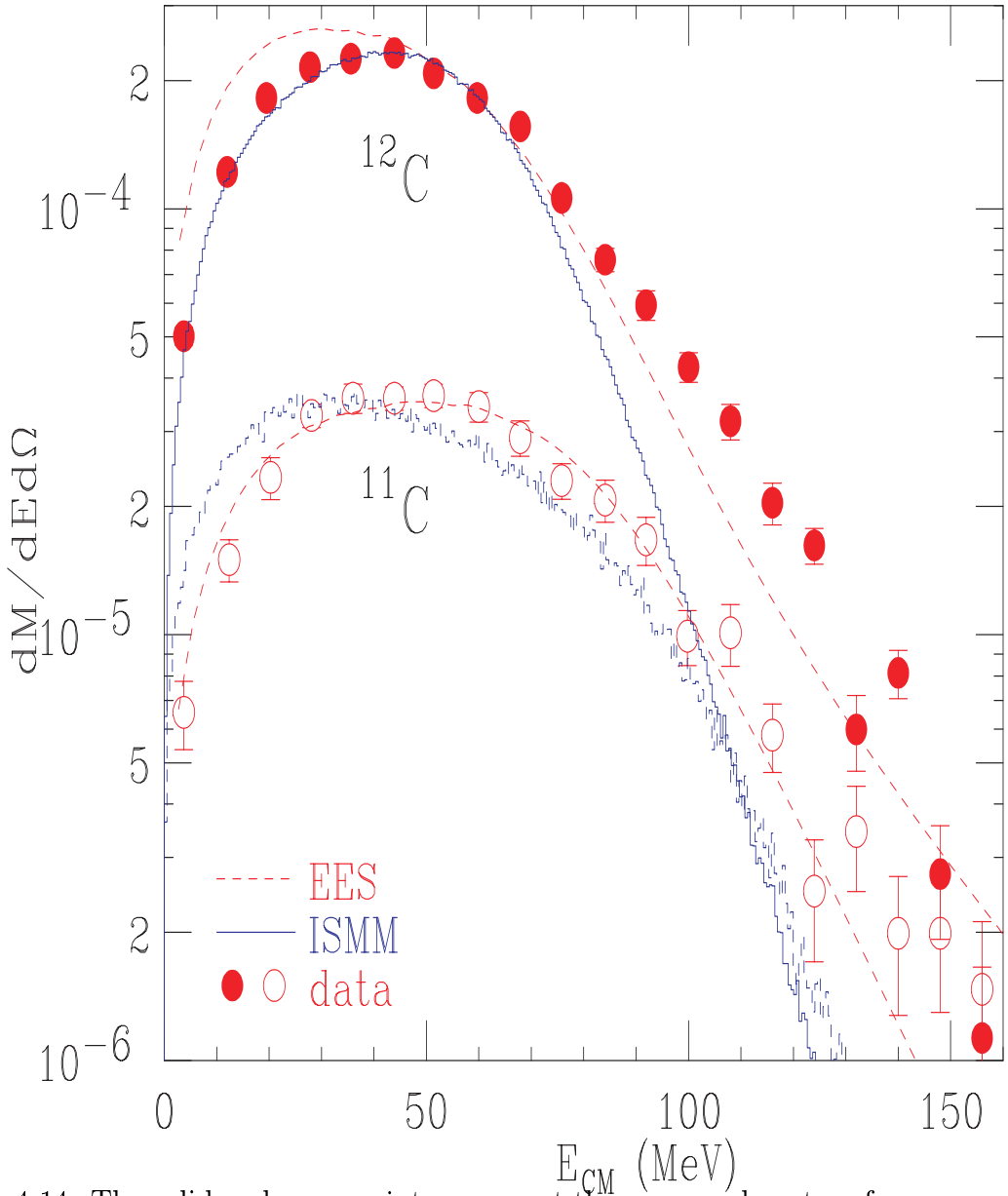

Figure 4.14: The solid and open points represent the measured center of mass energy spectra for ^{11}C and ^{12}C fragments, respectively. The solid lines represent the corresponding ISMM calculations. The dashed lines represent the corresponding EES model calculations.

A are plotted in the left panel of Fig. 4.15. In this figure, the isotopes of each element have the same symbols. The even Z (Z=2, 4, 6, 8) elements are represented by closed symbols and the odd Z (Z=1, 3, 5, 7) elements by the open symbols. Generally, $< E_{CM} >$ increases with A; however, the lightest isotopes in each element (^{3}He, ^{6}Li, ^{7}Be, ^{10}B, ^{11}C, ^{13}N) display a significantly larger mean energies than the neutron rich isotopes. (Due to insufficient statistics, the uncertainties in the measured mean energy of the neutron deficient oxygen isotope, ^{15}O is very large and not usable.) This striking trend is contrary to the behavior described by Eq. 4.8 for fragment emission from a single equilibrated source.

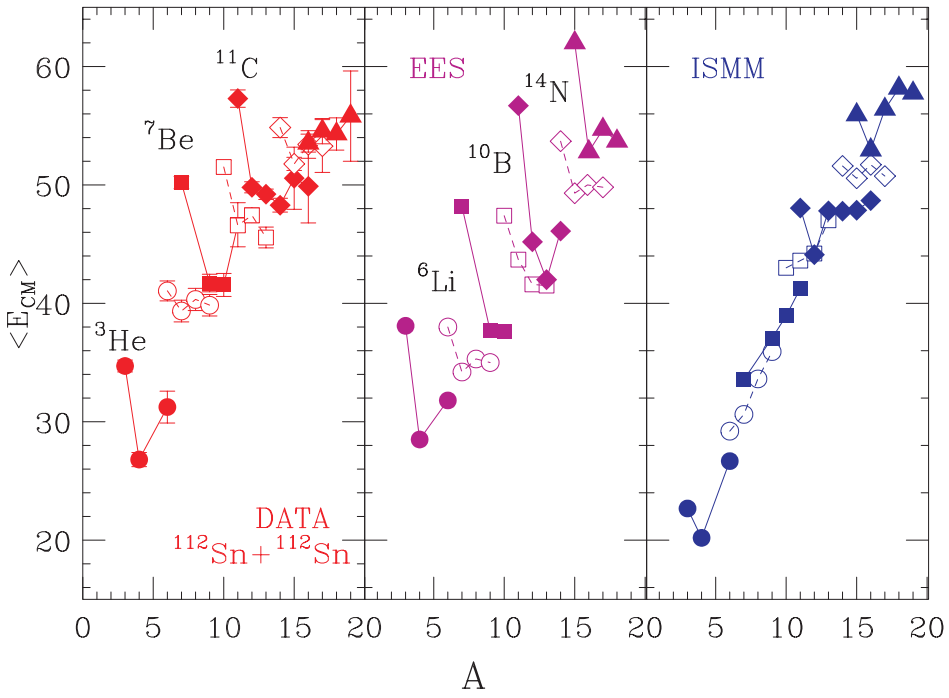

Figure 4.15: Left panel: experimental fragment mean kinetic energies. Middle panel: mean kinetic energies calculated with the EES model. Right panel: mean kinetic energies calculated with the ISSM model.

While Eq. 4.8 describes the trend expected for an equilibrated system of excited

fragments, sequential decay of the excited fragments emitted from a single equilibrated source can change this trend. To estimate such effects, we use the improved Statistical Multi-fragmentation Model (ISMM) of ref. [103] to model equilibrium breakup configurations composed of excited fragments and light particles and calculated the sequential decay of the excited fragments with a Monte-Carlo Weisskopf model [119].

To compare with experimental results, we calculated the energy spectra from the decay of an initial source with A_0=168, Z_0=75 and E^*/A= 6 MeV (roughly 75% of the total mass, charge and energy of the combined projectile and target [106]). Initially, we assign randomly a thermal velocity to each fragment and light particle according to a Boltzmann distribution characterized by a breakup temperature of T= 5.24 MeV [103] and we position each particle or fragment randomly within a volume of 8.3 fm. We add a collective velocity $\mathbf{v} = \frac{\mathbf{r}}{R} v_{coll,max}$ to the thermal velocity, and vary $v_{coll,max} = \sqrt{2(E_{coll}/A)/m_N}$ (i.e. E_{coll}/A) to describe the mass dependence of the experimental mean energies. We solve the classical equations of motion these particles interacting via Coulomb forces.

The optimal choice of collective velocity depends on details of the placement of fragments within the volume. If one excludes initial configuration that place any part of a fragment outside R, the accepted configurations fragments will be more concentrated in the interior than if one excludes configurations that place the center of mass of any fragment outside R. In the former case, the fragments experience larger Coulomb forces on average and the collective energy per nucleon needed to reproduce the $< E_k >$ data, $E_{Coll}/A \approx 0$, is less than that for the latter case, $E_{Coll}/A \approx 2$MeV. Regardless of the details of the spatial distribution of fragments at breakup, however, these equilibrium calculations do not reproduce the measured enhancements of the mean energies of the most neutron deficient fragments.

To demonstrate this, we show results for a calculation in which the centers of mass of fragments are randomly distributed over a spherical volume of radius R. Predicted ^{11}C and ^{12}C spectra (normalized to the data) are shown as blue lines in Fig. 4.14. The calculation reproduces the peak of the ^{12}C spectrum better than it does the peak of the ^{11}C spectrum; neither the ^{11}C nor the ^{12}C calculation reproduces well the high-energy tails of the corresponding experimental spectrum. The right panel in Fig. 4.15 shows that the predicted mean energies does not reproduce enhanced values observed experimentally for the $N < Z$ neutron deficient fragments. The slightly depressed values for $< E_k >$ calculated for symmetric $N = Z$ fragments reflect strong secondary decay contributions to these $N = Z$ nuclei from the secondary decay of heavy particle unbound nuclei that have somewhat smaller initial velocities. The strength of these secondary decay contributions reflect the Q-value for secondary decay, which favor decays to well bound $N = Z$ nuclei and suppresses decay to their $N < Z$ neighbors, but the calculated change in $< E_k >$ is very much smaller than that observed experimentally. Changing the assumptions about the spatial distribution of fragments or the collective velocity at breakup will not change this conclusion.

This failure and the aforementioned evidence for surface emission of helium isotopes suggest that fragments may also be emitted from the surfaces of the system while it is expanding and cooling. Because the binding energies of the neutron deficient isotopes are significantly less than those of their neutron rich neighbors, their surface emission rates will decrease relative to their neutron rich neighbors as the system cools. The Expanding Emitting Source (EES) model [39] provides a means to test this scenario. First the model predicts a sequence of source conditions that reflect the cooling of system, rather than a single one. Second it provides a self-consistent calculation of unique sequences of emission rates for each isotope.

To illustrate these ideas, we have performed an EES calculation, which assumes

that particles can be radiated from the surface of the expanding system prior to bulk disintegration. Unlike equilibrium models, which assume the system to have already expanded, this time dependent model calculates the expansion and emission of the system beginning at an earlier time as it expands through saturation density. Specifically, the model assumes surface emission for $\rho \geq 0.4\rho_0$, bulk emission for $\rho \leq 0.3\rho_0$ and a gradual transition from surface to the bulk emission for densities, $0.4\rho_0 > \rho > 0.3\rho_0$. For our EES calculations, we take saturation density, E^*/A=9.5 MeV, A_0=224 and Z_0=100 as the specific starting conditions.

As one example of the EES model results, we show the time evolution of ^{11}C and ^{12}C yields. At the time of emission, the primary fragment of each isotope acquires an average kinetic energy dictated by the instantaneous Coulomb barrier, expansion velocity and temperature of the expanding system. (The early surface emission contributions increase the value of the Coulomb and collective contributions above those obtained from the bulk emission alone.) Taking this time dependence into account, we plot the $< E_k >$ values for ^{11}C (blue dashed line) and ^{12}C (red solid line) as a function of the time of emission in the left panel of Fig. 4.16. Over the evolution of the source the carbon isotopes are emitted with a range of kinetic energies but there is very little difference between the values for the two carbon isotopes at any given time.

We next examine the emission rates as a function of time for the two isotopes. This is shown in the lower right panel of Fig. 4.16 where the instantaneous rates for each isotope are plotted and in the upper right panel of Fig. 4.16 where the ratio of the rates is plotted. Here we find that the rate for the emission of ^{11}C relative to that of ^{12}C changes drastically with time. The emission of the former is enhanced at earlier time and the latter at later time. Within the EES model, the rates are determined primarily by three factors: the spin degeneracy factors of each channel,

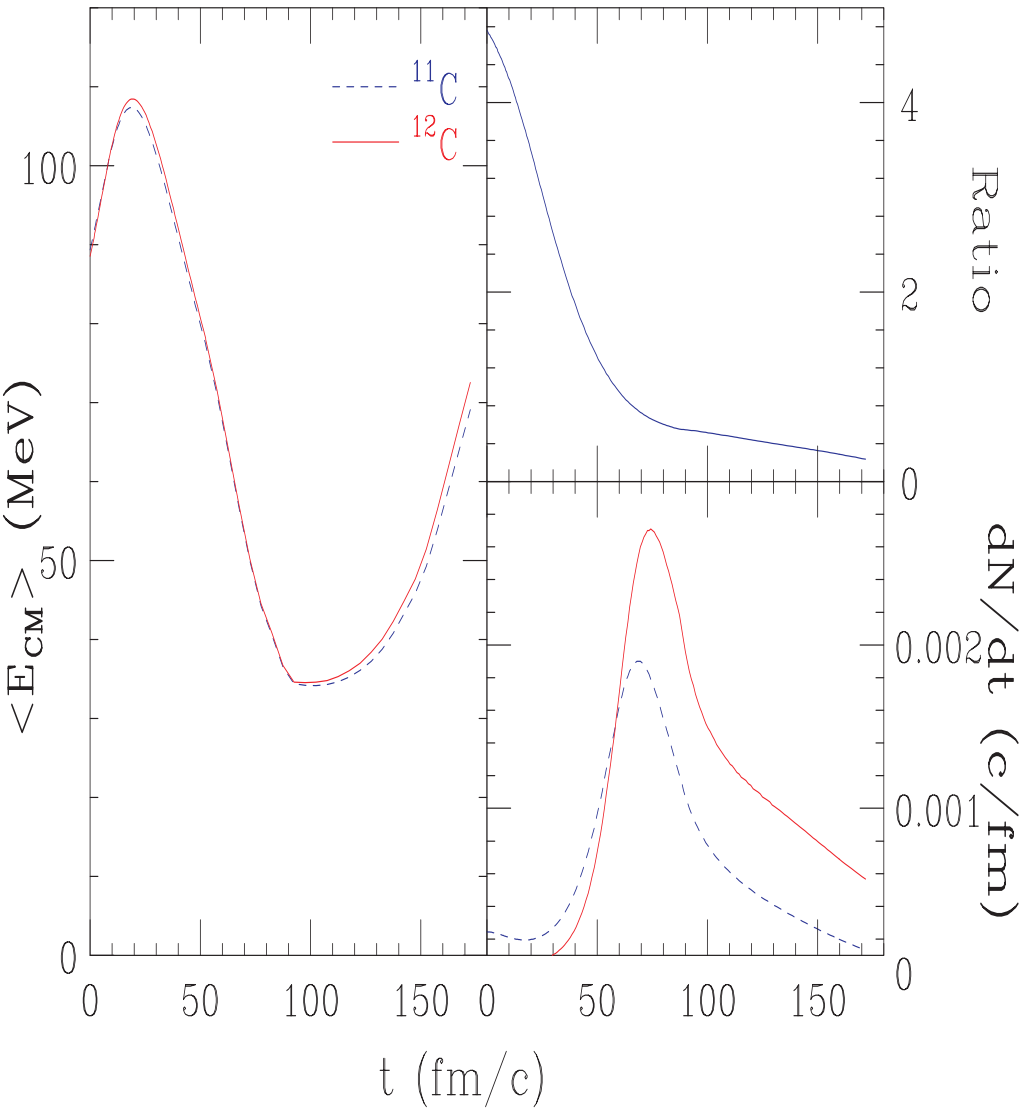

Figure 4.16: Left panel: Mean center of mass kinetic energies for ^{12}C(^{11}C) calculated as a function of time with the EES model. Lower right panel: Emission rates for ^{12}C (^{11}C) calculated as a function of time with the EES model. Upper right panel: Ratio of the emission rate for ^{11}C divided by the emission rate for ^{12}C calculated with the EES model.

free energy, $exp((N f_n^*(T) + Z f_p^*(T))/T)$, and binding energy, $exp(-Q/T)$. Here, $f_{n(p)}^*(T)$ are the excited free energy per neutron (proton) of the source, and Q is the Q-value associated with the emission. The degeneracy factors favor ^{11}C. The values for f^* are negative and hence the isotope with fewer nucleons is also favored by this factor. The magnitude of f^*, however, goes to zero like T^2 so the relative advantage for ^{11}C arising from this factor deceases as the temperature goes down. The Q values are greatly influenced by the respective binding energy factor, which strongly favors the $N = Z$ isotopes; this preference strengthens at reduced temperature. The net effect is that the preference for the ^{11}C at the highest temperatures shifts to ^{12}C as the temperature falls with the emission and expansion. We tested whether the binding energy is the dominant consideration by forcing the binding energies for ^{11}C and ^{12}C to be equal. In this test calculation, the relative emission rates for the two isotopes changed little with time.

In the EES model, ^{11}C is preferentially emitted earlier than ^{12}C, and the shapes of the energy spectra are consequently not the same. In Fig.4.16, we show the calculated energy spectra for ^{11}C and ^{12}C (red dashed lines) by taking a convolution of spectra each arising from the instantaneous conditions of the source. The EES model reproduces the shift in the peak of the energy spectra, but somewhat underpredicts the slope of the spectra for both isotopes. We note that it is necessary to multiply the EES model predictions for both ^{11}C and ^{12}C by a factor of 0.3 to match them to the data. We attribute this reduction to the fact that the emission of elements with $Z > 10$ are not considered in these EES model calculations.

The total yield of ^{12}C contains contributions from the neutron decay of excited ^{13}C and the α decay of excited ^{16}O. The yields of ^{11}C are not affected significantly by sequential decays. Integrating over the energy spectra, we find an average kinetic energy of about 56.7 MeV for ^{11}C and 45.2 MeV for ^{12}C. The difference of about 11

MeV is in qualitative agreement with the data. This same scenario applies to the other elements, each of which shows similar patterns for relative emission. We show the EES calculations for the mean energies of all isotopes in the middle panel of Fig. 4.15. The EES model reproduces the basic trends of the data.

Besides the success of these schematic calculations, other considerations support the hypothesis of an early surface emission of fragments prior to bulk emission from an expanded system. We note that surface evaporation and fission are the basic decay modes of equilibrated compound nuclei formed at lower incident energies. Transport theory, which describes preequilibrium emission in collisions at Fermi energies and above, predicts the abundant emission of nucleons and clusters as the system expands to low density. The early emission of fragments should not be surprising. Indeed, the preequilibrium emission of fragments have been previously reported in for proton induced reactions [87], and similar isotopic effects were observed. Here we have shown that such effects are relevant even for the multifragmentation process that have been heretofore interpreted widely as an equilibrium process. Now, the task before us is to understand how this early emission and other non-equilibrium effects impact the utilization of multifragmentation as a probe of the liquid-gas phase transition of nuclear matter.

4.3 Isospin Diffusion in the Peripheral Collisions and Model Calculation

4.3.1 Data from the Peripheral Collision

We used peripheral collisions for our isospin dynamics study. As experimental observables, we focus on features of isotopic yields $Y_i(N, Z)$ of particles measured for reaction "i". Here, N and Z are the neutron and proton numbers for the detected

fragments. The differential multiplicities of different isotopes were obtained by first selecting the peripheral collision events with $\hat{b} > 0.8$, then the background level was approximated by fitting each element on the 1D PID histogram. Since the statistics is not high enough to allow us to do the background level approximation with many different energy bins, only two bins are used, for particles stop in the second silicon detector or stop in the CsI crystals, respectively. The efficiency correction was done by dividing the measured 2D y_r-$p_\perp$ histogram by the corresponding efficiency function to get a corrected 2D y_r-$p_\perp$ histogram. A histogram of corrected yield of ^{12}C after reflection can be found in Fig. 4.17. A "Coulomb hole" can be seen clearly at the rapidity region near that of the projectile. These 2D y_r-$p_\perp$ histograms can be used to get the isotopic yields in different rapidity bins.

To study the isospin diffusion, projectile rapidity fragments were selected by a rapidity gate of $y_r = y/y_{beam} > 0.7$, where y and y_{beam} are the rapidities of the analyzed particle and the beam, respectively. The contributions from the neck fragments are minimized in this rapidity region. Fig. 4.18 shows the measured average differential multiplicities of Li, Be, B, C, N and O isotopes at $y_r > 0.7$ which can be compared with the corresponding data from central collisions. One can see that the yields from ^{112}Sn+^{124}Sn and ^{124}Sn + 112Sn are not the same, especially in the tails of the isotope distributions. This property can be used to study the isospin diffusion.

We analyzed the ratios of isotopic yields $R_{21}(N,Z) = Y_2(N,Z)/Y_1(N,Z)$ for a specific pair of reactions with different total isotopic composition and found that they follow the same isoscaling relationship as described in Eq. 4.2 [110]. It suggested this may be a compact and accurate way to quantify the isotopic asymmetry effects caused by isospin diffusion.

The left panel of Fig. 4.19 shows measured values for $R_{21}(N,Z)$ assuming ^{124}Sn + ^{124}Sn collisions as reaction 2 and ^{112}Sn + ^{112}Sn collisions as reaction 1 in Eq. 4.2. The

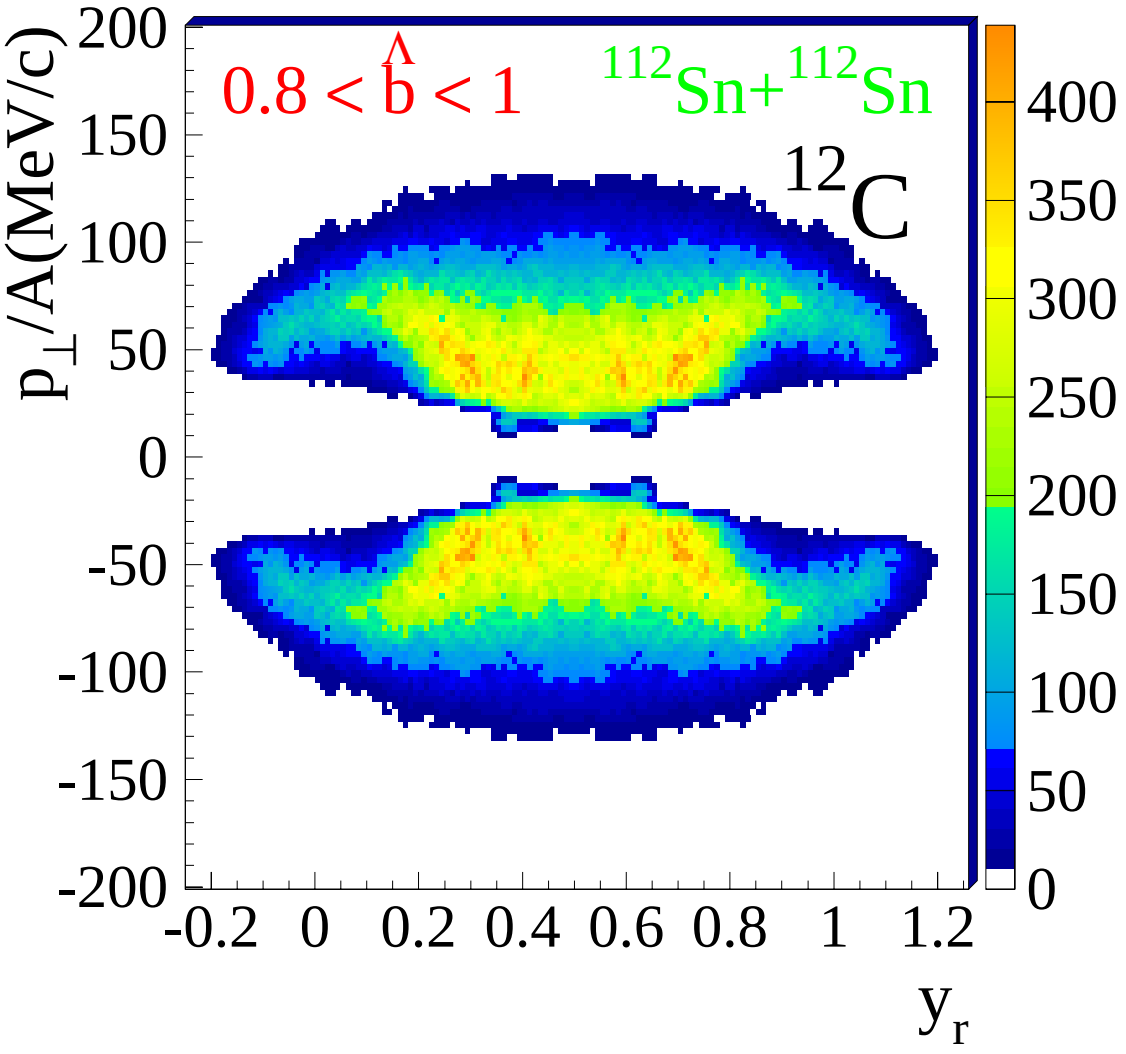

Figure 4.17: Efficiency corrected differential multiplicity $dM/dydp_\perp$ for ^{12}C fragments in peripheral collisions. A "Coulomb hole" can be clearly seen at $y_r \sim 0.05$ and $y_r \sim 0.95$.

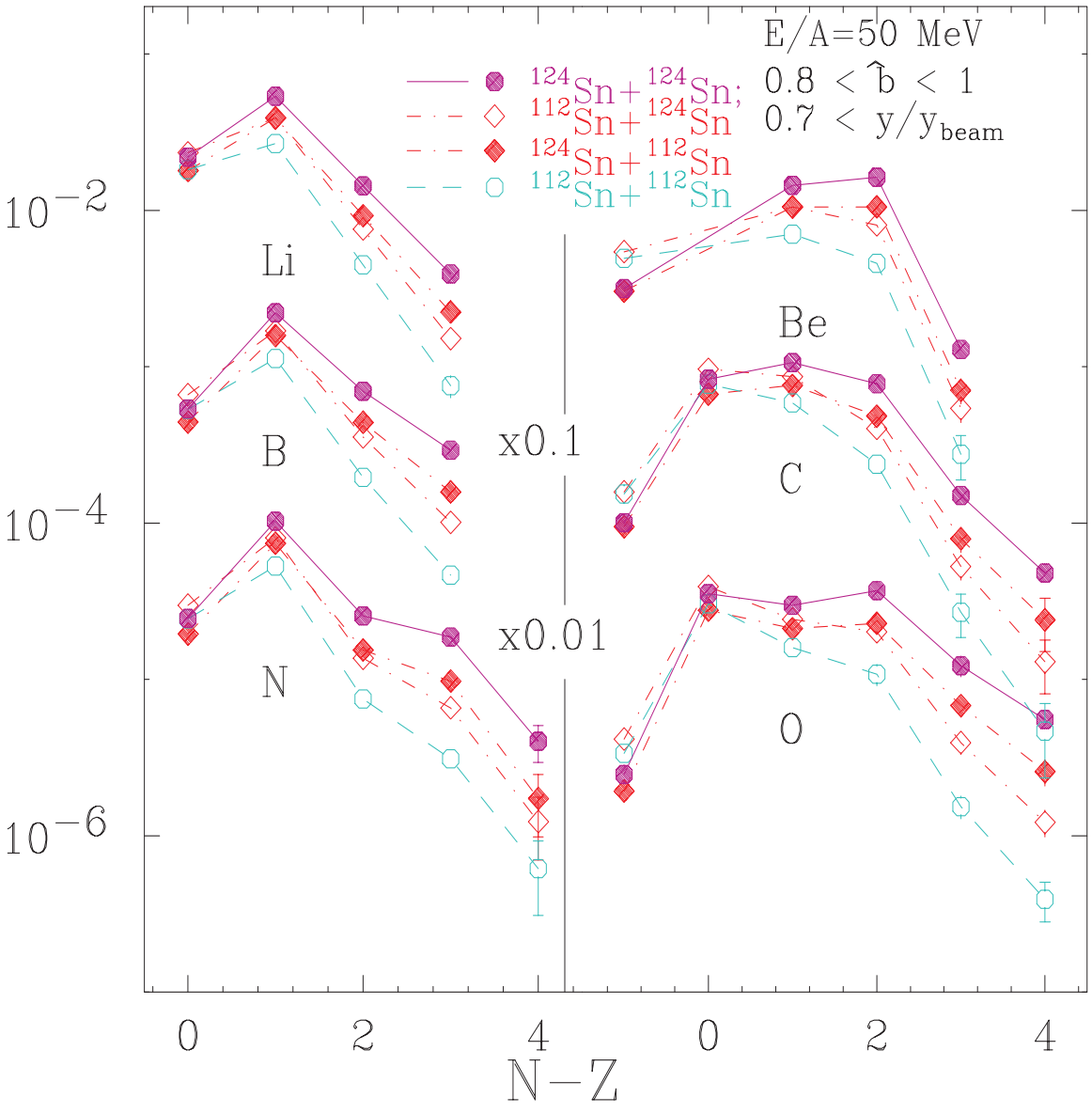

Figure 4.18: Average differential multiplicities as a function of neutron excess ($N-Z$) of the isotope for peripheral collisions, $\hat{b} > 0.8$, for Li, Be, B, C, N and O isotopes with rapidity near that of the projectile. The solid circles are data for the ^{124}Sn+^{124}Sn system with N/Z=1.48. The open circles are data for the lightest system ^{112}Sn+^{112}Sn with N/Z=1.24. The solid diamonds are data for system ^{124}Sn+^{112}Sn. The open diamonds are data for system ^{112}Sn+^{124}Sn. The solid, dashed and dot-dashed lines are drawn to guide eyes.

fit to Eq. 4.2 are shown as the solid and dashed lines. Fits to the other systems (not shown) are of similar quality. In the right panel of Fig. 4.19, we plot the best fit values for the isoscaling parameter, α, versus the overall isospin asymmetry of the colliding system: $\delta_0 = (N_0 - Z_0)/(N_0 + Z_0)$, where N_0 and Z_0 are the corresponding total neutron and proton numbers. The solid and open points denote data for ^{124}Sn and ^{112}Sn projectiles, respectively. In general, the isoscaling parameter α increases with the overall isospin asymmetry δ_0. Statistcal calculations, both from multifragmentation and evaporation predict that the isoscaling parameter should depend approximately linearly on the isospin asymmetry δ_0 of the entire system. If the linear correlation between α and δ_0 [123] is assumed, the mixed systems at $\delta_0 = 0.153$ should assume an α value midway between that of ^{124}Sn + ^{124}Sn ($\delta_0 = 0.193$, α=0.57$\pm$0.02) and ^{112}Sn + ^{112}Sn ($\delta_0 = 0.107$, α=0). However, the measured value for the ^{124}Sn projectile (solid point) is much larger than the value for the ^{112}Sn projectile (open point) at $\delta_0 = 0.153$ indicating that the emitting source is not consistent with the achievement of isospin equilibrium is not achieved in the asymmetric reaction systems [33]. The upper value of α=0.42$\pm$0.02, obtained for ^{124}Sn + ^{112}Sn, represents an effective asymmetry of about 0.17. This value corresponds to roughly half way from the projectile value of 0.193 to the "equilibrium" value of 0.153. The lower value of 0.16$\pm$0.02, obtained for ^{112}Sn + ^{124}Sn, has the same interpretation; except here the projectile is ^{112}Sn and the change in asymmetry is in the opposite direction. The consistency of these results extracted from two independent measurements adds credibility to the approach.

Because there are no isospin differences between identical projectiles and targets, we use symmetric ^{112}Sn + ^{112}Sn and ^{124}Sn + ^{124}Sn collisions in the following analyses to establish diffusion-free baseline values for the measured and predicted observables. The asymmetric ^{124}Sn + ^{112}Sn and ^{112}Sn + ^{124}Sn collisions, on the other hand, have the large isospin differences needed to explore isospin diffusion. Following ref. [86],

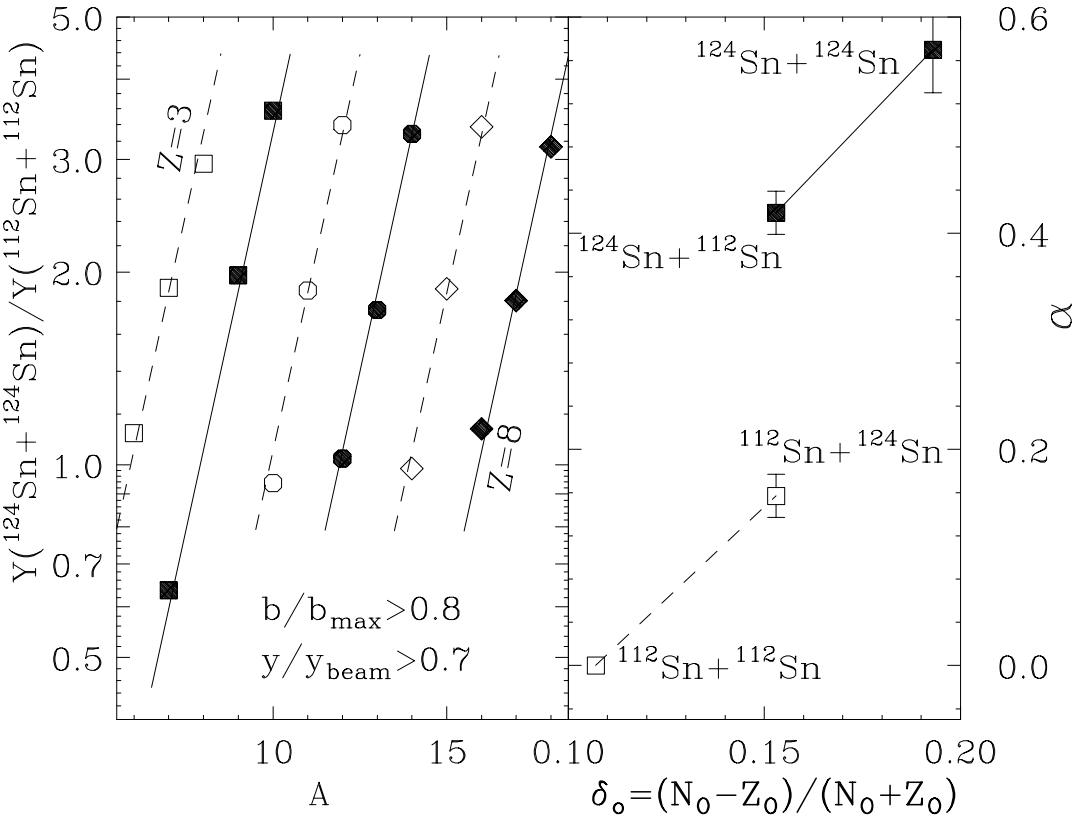

Figure 4.19: Left panel: Measured values for $R_{21}(N,Z) = Y_{124+124}(N,Z)/Y_{112+112}(N,Z)$ (points) and fits with Eq. 4.2 (solid lines). The solid line and points represent even Z=4,6,8 isotopes while the dash lines and open points represent odd Z=3,5,6 isotopes. Right panel: Best fit values for α as function of δ_0. The lines serve to guide the eye. The reactions are labeled next to the data points. $\delta_0 = 0.107$ and 0.194 for the symmetric systems of ^{124}Sn+^{124}Sn and ^{112}Sn+^{112}Sn respectively. The two mixed systems have the same $\delta_0 = 0.153$. Solid points denote ^{124}Sn as the projectile and open points denote ^{112}Sn as the projectile.

we define the isospin transport ratio, R_i as

$$R_i = \frac{2x - x_{124+124} - x_{112+112}}{x_{124+124} - x_{112+112}} \ , \tag{4.9}$$

where x is an isospin sensitive observable. For the two symmetric systems ^{124}Sn + ^{124}Sn and ^{112}Sn + ^{112}Sn, R_i is automatically normalized to $+1$ and -1, respectively, allowing quantitative comparison of the measured and predicted R_i values even if the model calculations use isospin observables that are different from the experimental ones. The only requirement is that both the experimental and theoretical observables depend linearly upon the isospin asymmetry δ_0 of the emitting source. To represent the experimental data, we chose the neutron isoscaling parameter α because the projectiles and targets for the asymmetric systems differ only in their neutron numbers. Using α for x in Eq. 4.9, we obtain the isospin transport ratios of the two asymmetric systems shown as the shaded bands in Fig. 4.21. The observed values, $|R_i(\alpha)| \approx 0.5$, are consistent with previous discussion that the isospin asymmetry of the projectile remnant is half way between that of the projectile and the "equilibration value".

Changes in α may result from both isospin diffusion and preequilibrium emission. In the absence of isospin diffusion, preequilibrium emission from the projectile should be approximately equal for asymmetric ^{124}Sn + ^{112}Sn (^{112}Sn + ^{124}Sn) collisions as for symmetric ^{124}Sn + ^{124}Sn (^{112}Sn + ^{112}Sn) collisions. By focusing on differences between mixed and symmetric systems, $R_i(\alpha)$ largely removes the sensitivity to preequilibrium emission and enhances the sensitivity to diffusion.

We can use other physical observables to construct R_i. Since mirror nuclei have similar secondary decay modes, we can reduce the effects of the secondary decay and enhance the effects of diffusion if we take the ratio of the mirror nuclei. Fig. 4.20 shows R_{i7}, constructed from $\ln[Yield(^7\mathrm{Be})/Yield(^7\mathrm{Li})]$, as a function of relative rapidity in the center of mass, $(y - y_{cm})/y_{beam}$. The R_{i7} from reaction ^{112}Sn + ^{124}Sn is reflected about 0 to give an overall trend. Note, we use $\ln[Yield(^7\mathrm{Be})/Yield(^7\mathrm{Li})]$ instead of

the ratio $Yield(^7\mathrm{Be})/Yield(^7\mathrm{Li})$ because $\ln[Yield(^7\mathrm{Be})/Yield(^7\mathrm{Li})] \propto (\mu_p - \mu_n)/T$ just as $\alpha \propto \Delta\mu_n/T$. We expect this to give a corrected ratio R_i which is closer to linear dependence on the isospin asymmetry δ_0 of the emitting source than does $Yield(^7\mathrm{Be})/Yield(^7\mathrm{Li})$. We see that R_{i7} agrees with $R_i(\alpha)$ for $|(y - y_{cm})/y_{beam}| \geq 0.2$. In addition, R_{i7} give us the ability to explore isospin diffusion as a function of y and $p_\perp$.

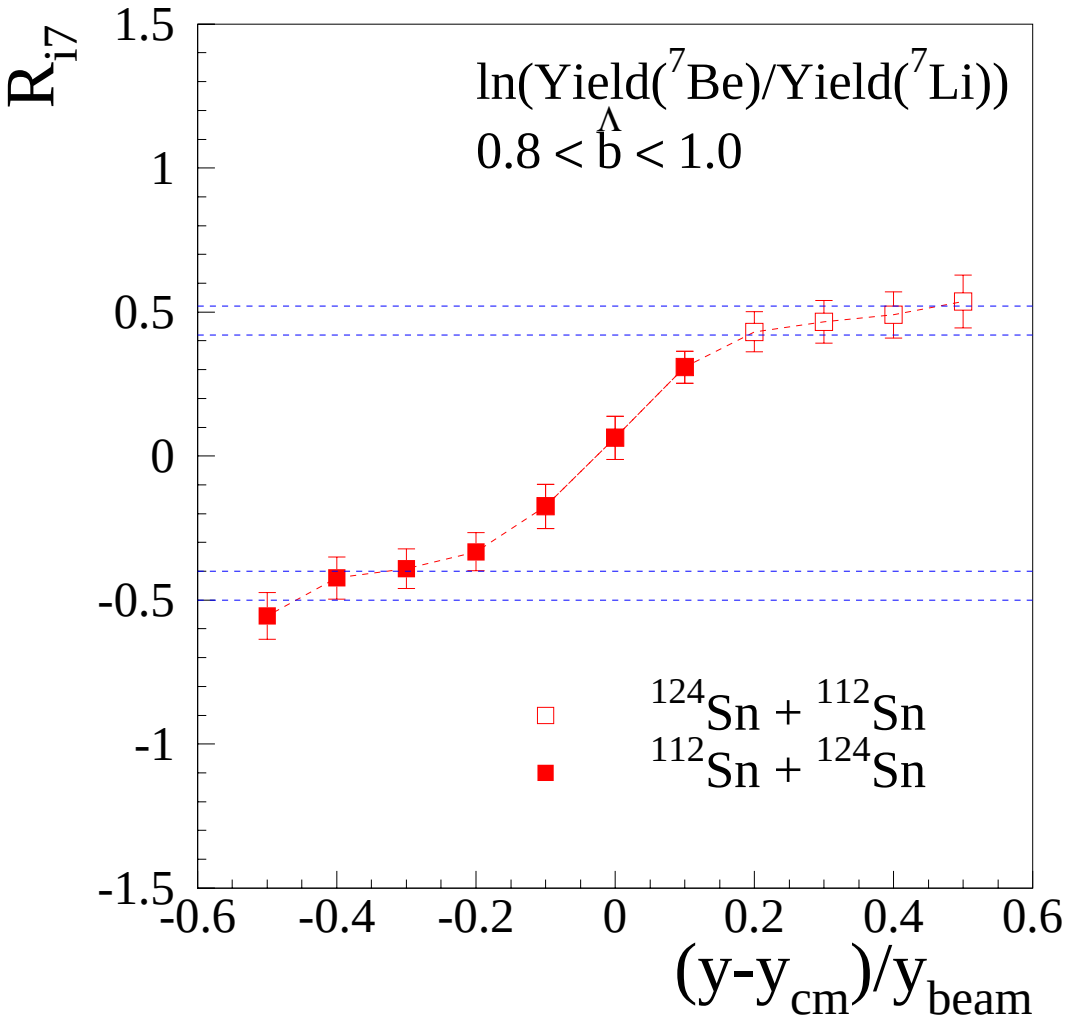

Figure 4.20: R_{i7}, constructed using $\ln[Yield(^7\mathrm{Be})/Yield(^7\mathrm{Li})]$, as a function of $(y - y_{cm})/y_{beam}$.

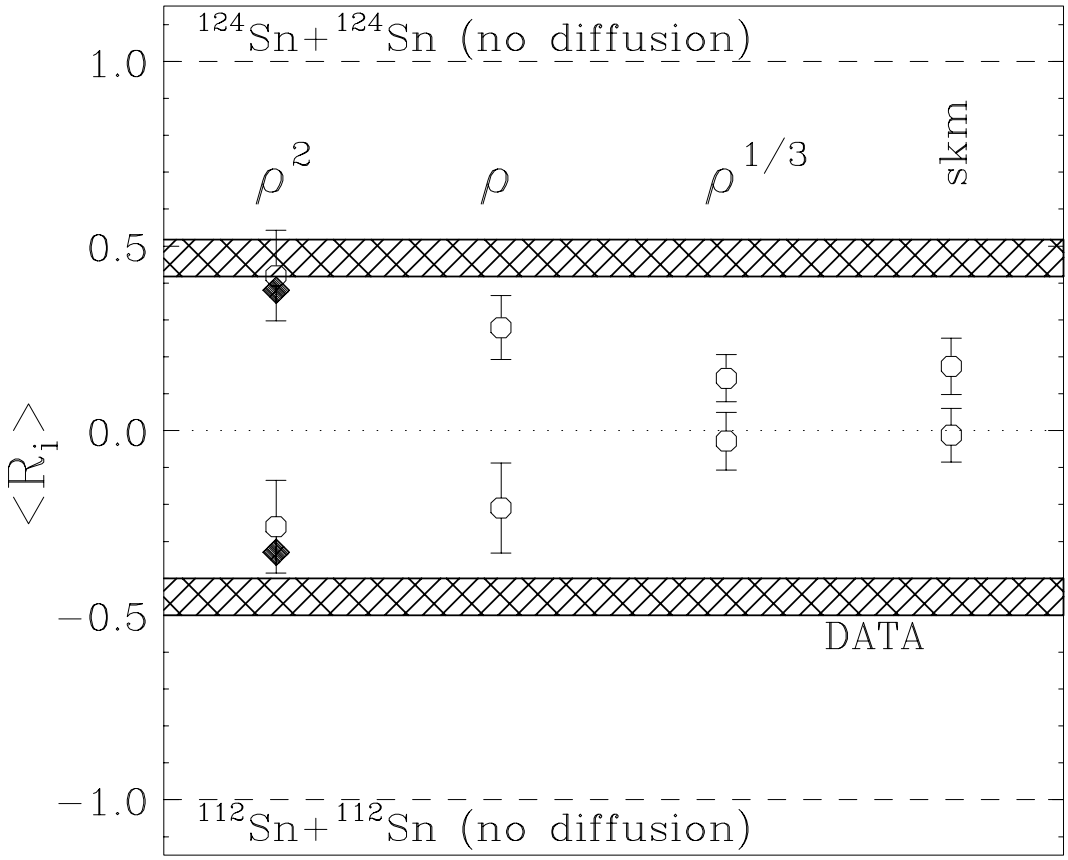

Figure 4.21: Average measured (shaded bars) and calculated (open points) values for R_i . The labels on the calculated values represent the density dependence of $E_{sym,int}/A$ with decreasing stiffness from left to right.

4.3.2 BUU Calculations

We now explore the relationship between isospin diffusion, and the asymmetry term of the EOS within the context of the Boltzmann-Uehling-Uhlenbeck (BUU) [6, 62] formalism, which calculates the time evolution of the colliding system using a self-consistent mean field. The isospin independent part of the mean field in these calculations is momentum independent and described by an incompressibility coefficient of K=210 MeV [93]. The interaction component of asymmetry term in three sets of calculations provides a contribution to the symmetry energy per nucleon of the form $E_{sym,int}$/A=C$_{sym}(\rho/\rho_0)^{\gamma}$ where C_{sym} is set to 12.125 MeV and γ=2, γ=1 and γ=1/3 . Here, smaller values for γ dictate weaker density dependence for E$_{sym,int}$. The fourth set of calculations, referred to as SKM, uses an interaction asymmetry term providing $E_{sym,int}/A$ =38.5 (ρ/ρ_0) − 21.0$(\rho/\rho_0)^2$ [2] and has the weakest density dependence.

Calculations were performed for the ^{124}Sn + ^{124}Sn, ^{124}Sn + ^{112}Sn, ^{112}Sn + ^{124}Sn and ^{112}Sn + ^{112}Sn systems at an impact parameter of b=6 fm [93]. We employed ensembles of 800 test particles per calculation and followed each calculation for an elapsed time of 216 fm/c. At this late time, the projectile and residues can be cleanly separated. Nonetheless, we require that all nucleons in the assigned regions to have density less than $0.05\rho_0$ and velocities above half the beam velocity in the center of mass to be consistent with the experimental gates. To reduce statistical fluctuations in the results, we averaged 20 calculations for each system.

Using the average asymmetry of the projectile-like residue $< \delta >$ in the calculation, as the isospin observable, x, in Eq. 4.9, we plot predictions for $R_i(\delta)$ as a function of time as bands in Fig. 4.22 for the stiffest asymmetry term, (ρ^2 , top panel) and the softest asymmetry term, (SKM, bottom panel). By construction, $R_i(\delta)$ describes the evolution of isospin asymmetry for the projectiles (^{112}Sn or ^{124}Sn) in the mixed reactions relative to that for the symmetric ^{124}Sn + ^{124}Sn (with $R_i = 1$) and ^{112}Sn +

^{112}Sn ($R_i = -1$) systems. The widths of the bands reflect the statistical uncertainties of the calculated values for $R_i(\delta)$. Initially, these predictions for $R_i(\delta)$ represent the isospin of the projectile ($\mathrm{R}_i(\delta) = 1$ for ^{124}Sn and $R_i(\delta) = -1$ for ^{112}Sn) nuclei. Subsequent isospin diffusion drives the $R_i(\delta)$ values towards zero. Even though pre-equilibrium emission from the projectile remnants influences $< \delta >$, $R_i(\delta)$ is not strongly modified because such pre-equilibrium emission is largely target independent and therefore cancelled in $R_i(\delta)$ by construction.

The influence of the asymmetry term depends on its magnitude at sub-saturation density [62, 93]. For the top panel, the energy is $E_{sym,int}/A = C_{sym}(\rho/\rho_0)^2$, which decreases rapidly at low density and becomes very small, leading to little isospin diffusion. For the bottom panel, $E_{sym,int}/A = 38.5\ (\rho/\rho_0) - 21.0(\rho/\rho_0)^2$ remains larger at low density, leading to stronger isospin diffusion and bringing the residues to approximately the same isospin asymmetry. In both cases, the asymptotic value for $R_i(\delta)$ is first reached at around 100 fm/c when the two residues separate and cease exchanging nucleons. This timescale is comparable to the collision timescale τ_{coll}, which can be roughly ($\sim$20%) estimated by

$$\tau_{coll} \approx (4R_N + d)/v_{beam} \approx 80 fm/c\ , \tag{4.10}$$

where R_N, v_{beam} and d are the nuclear radius, incident velocity, and the separation d between the two nuclear surfaces at breakup as illustrated by the time evolution images of the collisions for the ^{124}Sn + ^{124}Sn system in Fig. 4.22.

Assuming that the experimental isoscaling relationships, shown in Fig. 4.19, reflect particle emission from the projectile remnants after 100 fm/c and that such emission can be described statistically, the calculated values for $R_i(\delta)$ may be easily related to the measured ones. In doing so, we take advantage of the nearly linear relationship between α and the δ values that has been shown valid for evaporation and for statistical multi-fragmentation of the remnants that emit the observed particles

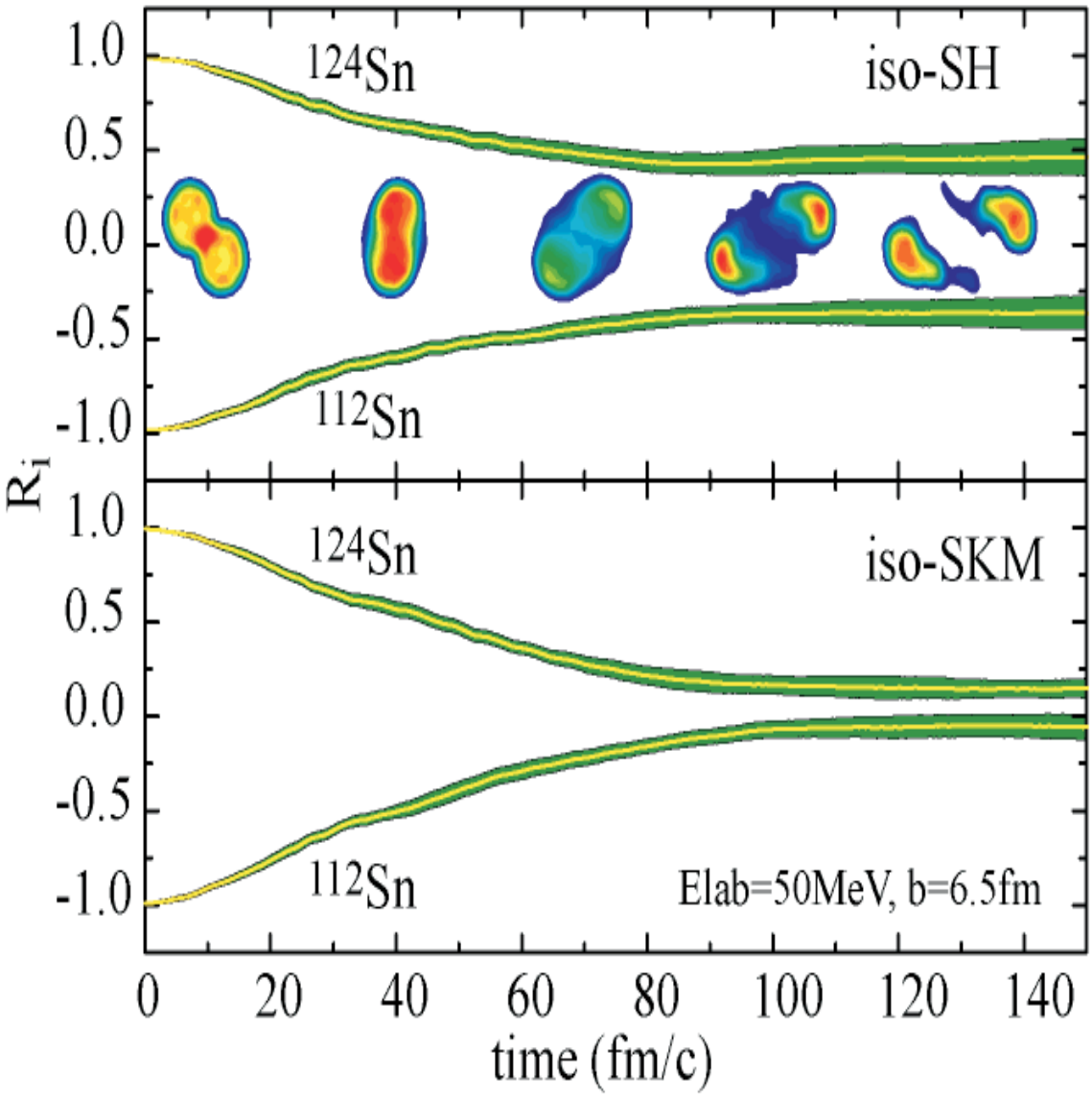

Figure 4.22: $R_i(\delta)$ from BUU calculations are plotted as a function of time for the mixed systems. The symmetric systems are calibrated to $+1$ and -1 automatically by Eq. 4.9. The top and bottom panels show the calculated results with $E_{sym,int}/A$ $=C_{sym}(\rho/\rho_0)^2$ and $E_{sym,int}/A$ $=38.5(\rho/\rho_0)^2$ - $21.0(\rho/\rho_0)^2$, respectively. The bands above (below) the dashed line represent the system with ^{124}Sn (^{112}Sn) as the projectile. The time evolution images of the collisions for the ^{124}Sn + ^{124}Sn systems are superimposed on the upper panel suggesting that the projectile and targets separates around 100 fm/c.

[112]:

$$\alpha \propto (\delta_2 - \delta_1)(1 - \frac{\delta_2 + \delta_1}{2}) \ , \tag{4.11}$$

where δ_1 and δ_2 are the asymmetries for the two systems involved in the isoscaling ratio. Inserting Eq. 4.11 into the expression for $R_i(\alpha)$, one can show

$$R_i(\alpha) = R_i(\delta) - \frac{(\delta_i - \delta_{112+112})(\delta_i - \delta_{124+124})}{(\delta_{124+124} - \delta_{112+112}) - (1 - (\delta_{124+124} + \delta_{112+112})/2)} \ . \tag{4.12}$$

Since the second term is negligible ($< 4\%$), we can obtain $< \delta >$ from the flat region at 216 fm/c, use it as x in Eq. 4.9 to obtain $R_i(\delta)$ values for these two systems and we can compare them to the experimental values of $R_i(\alpha)$. The calculated values, shown as open points in Fig. 4.21 in the order of an increasing "softness" from left to right indicate an increased isospin equilibrium for successively softer asymmetry terms. The diamond shaped points indicate the $R_i(\alpha)$ values obtained as in the experiment by decaying the residues simulated in BUU to fragments using the statistical model of ref. [112]. As expected, there is close agreement between the diamonds and the corresponding open points according to Eq. 4.12.

Fig. 4.21 demonstrates the sensitivity of such data to the asymmetry term of the EOS. The experimental $R_i(\alpha)$ values are closest to the predicted $R_i(\delta)$ values derived from the theoretical predictions for $< \delta >$ using the stiffest asymmetry term, (ρ^2, top panel) with $E_{sym,int}/A = C_{sym}(\rho/\rho_0)^2$. This conclusion depends, however, on the assumption that the measured particles are produced after 100 fm/c when $< \delta >$ attains its asymptotic values. If the data include emission from earlier stages when δ is larger, a favorable comparison with calculations using softer asymmetry terms may be possible. Relevant determinations of the emission timescales for the detected particles are being explored [93] and may serve to make the present conclusions regarding the density dependent asymmetry term more definitive.

Chapter 5

Summary

In this dissertation, we studied the asymmetry term in the EOS and isosipin diffusion using heavy-ion collisions at the intermediate energy. Calculations have shown that experiment observables such as the energy spectra, intermediate mass fragment (IMF) multiplicities, isoscaling parameters and various nuclei yield ratios are sensitive to the asymmetry term in EOS. We show for the first time in this dissertation that isospin diffusion rates measured in our experiment can also provide constraints on the symmetry term in the EOS.

We have measured the isotope energy and yields of Z=2-8 particles emitted in four different Sn+Sn reactions with different isospin asymmetry at 50MeV/A. To make the measurement, nine telescopes of the Large Area Silicon-Strip/CsI detector Array (LASSA) were developed and used in the experiment. The LASSA telescopes provided a high isotopic, energy and angular resolution which are not available in the previous experiments. Impact parameters were selected by the multiplicity of charged particles, measured with LASSA and the Miniball/Miniwall phoswich array.

Techniques were developed to enable the subtraction of background in the experimental data and the correction for the experimental detection efficiency. The background levels were mainly estimated at the elemental levels while for those weak

isotopes are estimated at the isotopic level. The efficiency correction was done using efficiency functions obtained from Monte Carlo simulations of the experiment. These efficiency simulations take care of the multiple hits, the inefficiencies in the solid angle and loss at low $p_\perp$. We examined the accuracy of the efficiency correction by comparing forward angle data and backward angle data obtained in symmetry collisions. From this comparison, we extract a systematic error bar for our data. For the part which can not be corrected by efficiency function, i.e. the inconsistence of the detection in silicon and CsI, a systematic error bar is given.

The total charged particle multiplicity detected in Miniball/Miniwall and LASSA was used for impact parameter determination. We selected central collision events, corresponding to a reduced impact parameter of $\hat{b} \leq 0.2$ and the top 4% of the charged-particle multiplicity distribution. The impact parameter is estimated to be less than 1.5 fm according to total cross section measurements. The peripheral collisions are selected corresponding to a reduced impact parameter of $\hat{b} > 0.8$ and bottom 40% of the charged-particle multiplicity distribution. The parameter is estimated to be greater than 6.0 fm in this case.

We used the isotope distributions for Z=2-8 from the central collision to compare with the results from dynamic model calculations which include fluctuations that give rise to fragment production. The experimental data display a strong dependence on the isospin asymmetry that can be accurately described by an isoscaling parameterization. The theoretical calculation reproduces the yields for the heavier fragments with Z=6-8, but underpredict the yields of the lighter ones which are not strongly produced by the calculation as primary fragments. The calculated final isotopic distributions display isoscaling, but the calculated isotopic distributions are narrower, more neutron deficient; and show a weaker dependence on the isotopic asymmetry of the system than do the data. The density dependence of the asymmetry term

of the EOS has an effect on the calculated final isotopic distributions. The distributions calculated using the asymmetry term with stronger density dependence are more neutron-rich and are closer to the measured values. These trends are similar to prior results obtained for a BUU-SMM hybrid model, but different from the trends for evaporated fragments predicted by EES rate equation calculations. The present level of agreement between theory and experiment precludes definitive statements about the density dependence of the asymmetry term of the EOS. A number of theoretical issues, such as the pre-equilibrium of bound clusters, the calculations of fragment excitation energies, and the importance of the extreme tails of the primary fragment distributions, may influence the calculated results. Additional theoretical work is required to explore these issues and to determine the role they may play in the resolution of these discrepancies. Complimentary measurements of the yields and energy spectra of light particles can help to determine whether the missing neutrons in the calculations are carried away primarily by pre-equilibrium emission during the compression-expansion stage or during the later evaporative decay of the hot fragments.

We compared the isotope energy spectra from central collisions with the data. We found that calculations from the bulk multi-fragmentation models, i.e. the improved Statistical Multi-fragmentation Model(ISMM), can not reproduces well the high-energy tails of the corresponding experimental spectra for heavy fragments like ^{11}C and ^{12}C. Neither can the bulk multi-fragmentation models reproduce enhanced mean energy values observed experimentally for the $N < Z$ neutron deficient fragments. The Expanding Emitting Source(EES) model provides a better description of the measured energy spectra of the IMF isotopes produced in multifragmentation and mean energies of all isotopes. This success and other evidence for surface emissions reveal the dynamics of the emission process. The more energetic neutron deficient

isotopes are consistent with the picture that they are emitted earlier from the surface of the system while the source is expanding and cooling.

We have observed the influence of isospin diffusion with comparable diffusion and collision timescales. Simulations using the BUU transport model predict that isospin diffusion reflects driving forces arising from the asymmetry term of the EOS. The comparisons of experimental data and results of calculation suggest better agreement with stiff aymmetry term. This result agrees with what we have found by comparing the isotope distributions from the central collisions with SMF calculations. However, more stringent constraints on the emission timescales for the measured particles in the BUU calculations are needed. The version of the BUU used in our comparison does not have the momentum dependence of the mean field symmetry term. Recently new calculations by other groups indicate that the momentum dependence of the asymmetry needs to be carefully addressed. This issue as well as other issues such as the dependence of isospin diffusion on the impact parameter and the influence of the in-medium neutron-proton cross section by the residual interaction should be explored in more detailed future work.

LIST OF REFERENCES

[1] S. Albergo *et al.*, Nuovo Cimento **89**, 1 (1985).

[2] V. Baran *et al.*, Nucl. Phys. **A632**, 287 (1998)

[3] V. Baran *et al.*, Phys. Rev. Lett. **86**, 4492 (2001)

[4] V. Baran *et al.*, Nucl. Phys. **A703**, 603 (2002)

[5] G.F. Bertsch *et al.*, Phys. Rev. **C29**, 673 (1984).

[6] G. Bertsch *et al.*, Phys. Rep. **160**, 189 (1988)

[7] H.A.Bethe, Rev. Mod. Phys. **62**, 801 (1990)

[8] I. Bombaci, "Equation of State for Dense Isospin Asymmetric Nuclear Matter for Astrophysical Applications", "Isospin Physics in Heavy-IonCollisions at Intermediate Energies", Eds. Bao-An Li and W. Udo Schroeder, NOVA Science Publishers, Inc. (New York), p. 35 (2001)

[9] I. Bombaci, in Perspectives in Theoretical Nuclear Physics, edited by S. Rosati *et al.*, (Edizioni ETS, Pisa, 1996), p. 233

[10] J.P. Bondorf *et al.*, Nucl. Phys. **A443**, 321 (1985).

[11] J.P. Bondorf *et al.*, Phys. Rep. **257**, 133 (1995) and refs. therein

[12] B. Borderie *et al.*, Phys. Lett. **B388**, 224 (1996)

[13] B. Borderie *et al.*, Phys. Rev. Lett. **86**, 3252 (2001)

[14] J.P. Bondorf *et al.*, Nucl. Phys. **A475**, 663 (1987).

[15] D.R. Bowman *et al.*, Phys. Rev. Lett. **67**, 1527 (1991). edited by S. Rosati *et al.* (Edizioni ETS, Pisa, 1996), p. 233

[16] D.R. Bowman *et al.*, Phys. Rev. Lett. **70**, 3534 (1993)

[17] B.A. Brown, Phys. Rev. Lett. **85**, 5296 (2000).

[18] B.A. Brown, Phys. Rev. Lett. **85**, 5296 (2001)

[19] C. Cavata *et al.*, Phys. Rev. **C42**, 1760 (1990).

[20] R.J. Charity *et al.*, Nucl. Phys. **A483**, 371 (1988)

[21] C.B. Chitwood *et al.*, Phys Lett. **B172** , 27 (1986)

[22] N. Colonna *et al.*, Nucl. Instr. and Meth. **A321** 529 (1992)

[23] M. Colonna *et al.*, Phys. Rev. **C57**, 1410 (1998).

[24] M. Colonna *et al.*, Nucl. Phys. **A642**, 449 (1998)

[25] E. Cornell *et al.*, Phys. Rev. Lett. **75**, 1475 (1995)

[26] C. Csoto and G. M. Hale, Phys. Rev. **C55**, 2366 (1997).

[27] M. D'Agostino *et al.*, Phys. Lett. **B371**, 175 (1996)

[28] P. Danielewicz *et al.*, Phys. Rev. **C38**, 120 (1988).

[29] P. Danielewicz *et al.*, Nucl. Phys. **A533**, 712 (1991)

[30] P. Danielewicz, Nucl. Phys. **A673**, 375 (2000).

[31] P. Danielewicz *et al.*, Science **298**, 1592 (2002)

[32] B. Davin *et al.*, Nucl. Instr. and Meth., **A473**, 301 (2001)

[33] J.F. Dempsey *et al.*, Phys. Rev, **C54**, 1710 (1996) and refs. therein

[34] J.F. Dempsey, Ph.D. Thesis (Washington University, 1997)

[35] H. Feldmeier *et al.*, Nucl. Phys. **A586**, 493 (1995)

[36] J.D. Frankland *et al.*, Nucl. Phys. **A689**, 940 (2001)

[37] W.A. Friedman and W.G. Lynch, Phys. Rev. **C28**, 16 (1983).

[38] W.A. Friedman and W.G. Lynch, Phys. Rev. **C28**, 950 (1983).

[39] W.A. Friedman *et al.*, Phys. Rev. **C42**, 667 (1990).

[40] B. Gatty *et al.*, Nuc. Phys. **A253**, 511 (1975)

[41] A.L. Goodman *et al.*, Phys. Rev. **C30**, 851 (1984).

[42] D.H.E. Gross *et al.*, Z. Phys. **A309**, 41 (1982).

[43] D.H.E. Gross, Phys. Rep. **279**, 119 (1997)

[44] A. Guarnera *et al.*, Phys. Lett. **B373**, 373 (1996); A. Guarnera, Thesis U. Caen (1996)

[45] D.O. Handzy, Ph.D. Thesis (Michigan State University, 1995)

[46] P.E. Haustein *et al.*, At. Data Nucl. Data Tables **39**, 185-395(1988)

[47] D. Horn *et al.*, Nucl. Instr. and Meth. **A320** 273 (1992)

[48] W.C. Hsi *et al.*, Phys. Rev. Lett. **73**, 3367 (1994)

[49] M.J. Huang *et al.*, Phys. Rev. Lett. **78**, 1648 (1997).

[50] S.C. Jeong *et al.*, Phys. Rev. Lett. **72**, 3468 (1994)

[51] L.P. Kandanoff and G.Baym, Quantum Statistical Mechanics (Benjamin, New York, 1962)

[52] Y.D. Kim, *et al.*, Phys Rev. **C67**, 14(1991)

[53] Y.D. Kim, *et al.*, Phys Rev. **C45**, 338(1992)

[54] G.J. Kunde *et al.*, Phys. Rev. Lett. **77**, 2897 (1996)

[55] A.B. Larionov *et al.*, Nucl. Phys. **A658**, 375 (1999)

[56] Y. Larochelle *et al.*, Nucl. Instr. and Meth. **A384**, 167 (1994)

[57] J.M. Lattimer *et al.*, Phys. Rev. Lett. **66**, 2701 (1991)

[58] J.M. Lattimer and M. Prakash, Astrophys. **J550**, 426 (2001); Phys. Rep. **333**, 121 (2000)

[59] J.M. Lattimer and M. Prakash Science **304**, 536 (2004)

[60] B.A. Li *et al.*, Phys. Lett. **B303**, 225 (1993)

[61] B.A. Li *et al.*, Phys. Rev. **C52**, R1746 (1995).

[62] B.A. Li, *et al.*, Int. J. Mod. Phys. **E7** (1998) 147, and refs. therein

[63] B.A. Li *et al.*, Phys. Rev. Lett. **78**, 1644 (1997).

[64] B.A. Li, Phys. Rev. Lett. **85**, 4221 (2000)

[65] B.A. Li, Phys. Rev. Lett. **88**, 192701 (2002) and refs. therein

[66] W.G. Lynch, *et al.*, Phys Lett. **168B** , 274 (1982)

[67] W.G. Lynch, *et al.*, Phys Rev. Lett. **51** , 1850 (1983)

[68] W.G. Lynch, *et al.*, Phys Rev. Lett. **52** , 2302 (1984)

[69] W.G. Lynch, Ann. Rev. Nucl. Part. Sci. **37**, 493 (1987), and refs. therein

[70] N. Marie *et al.*, Phys. Lett. **B391**, 15 (1997)

[71] N. Marie *et al.*, Phys. Rev. **C58**, 256 (1998)

[72] P.F. Mastinu *et al.*, Nucl. Instr. and Meth. **A338** 419 (1994)

[73] L.G. Moretto and G.J. Wozniak, Annu. Rev. Nucl. Part. Sci. **43**, 379 (1993).

[74] H. Mori, Prog. Theor. Phys. **8**, 327(1952)

[75] H. Müller and B. D. Serot, Phys. Rev. **C52**, 2072 (1995)

[76] P. Braun-Munzinger etal, Phys. Lett. **B465**, 15 (1999)

[77] P. Braun-Munzinger etal, Phys. Lett. **B596**, 61 (2004)

[78] A. Ono *et al.*, Phys. Rev. Lett. **68** 2898 (1992); A. Ono *et al.* Phys. Rev. **C53**, 2958 (1996)

[79] A. Ono *et al.* Phys. Rev. **C53**, 2958 (1996)

[80] One might imagine that the fragment isobaric distributions might display a Gaussian dependence on asymmetry, i.e. $Y(N,Z) = f(A)\exp\left[-\frac{\left(\delta-\bar{\delta}\right)^2}{2\sigma^2}\right]$ where δ=(N-Z)/A and $\bar{\delta} = \langle\delta\rangle$ but we lack the statistics in our simulations to test this hypothesis

[81] C.J. Pethick and D.G. Ravenhall Annu. Rev. Nucl. Part. Sci. **45**, 429(1995)

[82] R. Planeta *et al.*, Phys. Rev. **C38**, 195 (1988), R. Planeta *et al.*, Phys. Rev. **C41**, 942 (1990).

[83] R. Popescu *et al.*, Phys. Rev. **58**, 270 (1998)

[84] L. Phair *et al.*, Nucl. Phys. **A548**, 489 (1992) and references therein

[85] M. Prakash *et al.*, Phys. Rev. Lett. **61**, 2518(1988)

[86] F. Rami *et al.*, Phys. Rev. Lett. **84**, 1120 (2000)

[87] E. Renshaw *et al.*, Phys. Rev. **C44**, 2618 (1991)

[88] L. Scalone *et al.*, Physics Letters **B461**, 9 (1999)

[89] W.U. Schröder and J.R. Huizenga, in *Treatise in Heavy-Ion Science*, edited by D.A. Bromley (Plenum Press, New York and London, 1984), Vol. 2, p. 113 and references therein

[90] B.M. Sherrill *et al.*, Nucl. Instr. and Meth. **B56/57** 1106 (1991)

[91] D.V. Shetty *et al.*, Phys. Rev. **C68**, 021602 (2003)

[92] L. Shi *et al.*, Europhysics Lett. **51**, 34 (2000)

[93] L. Shi *et al.*, Phys. Rev. **C68**, 064604 (2003).

[94] L.G. Sobotka *et al.*, Phys. Rev. **C55**, 2109 (1997)

[95] G.A. Souliotis, *et al.*, Phys. Rev. **C68**, 024605 (2003)

[96] R.T. de Souza *et al.*, Nucl. Inst. Meth. **A295**, 109 (1990); D.W. Stracener *et al.*, Nucl. Instr. Meth. **A294**, (1990) 485

[97] S.R. Souza *et al.*, Phys. Rev. **C62**, 064607 (2000)

[98] R. Stöcker *et al.*, W.Z. Phys. **A203**,259 (1981)

[99] C. Sturm *et al.*, Phys. Rev. Lett. **86**, 39 (2001)

[100] K. Sumiyoshi *et al.*, Nucl. Phys. **A552**, 437 (1993)

[101] W. P. Tan *et al.*, Phys. Rev. **C64**, 051901 (2001).

[102] W.P. Tan, Ph.D. Thesis (Michigan State University, 2002)

[103] W.P. Tan *et al.*, Phys. Rev. **C68**, 034609 (2003)

[104] W.P. Tan *et al.*, in preparation

[105] I. Tanihata, Report No. RIKEN-AF-NP-229 (1996)

[106] These values are consistent estimated that take cooling by preequilibrium emission and expansion prior to breakup into account, e.g. P. Desesquelles *et al.*, Nucl. Phys. **A633**, 547 (1998) for example

[107] M. Di Toro *et al.*, Nucl. Phys. **A681**, 426 (2001)

[108] M. Di Toro *et al.*, Eur. Phys. Jour. **A13**, 155 (2002) and refs. therein

[109] M.B. Tsang *et al.*, Lett. **B297**, 243 (1992)

[110] M.B. Tsang *et al.*, Phys. Rev. Lett. **86**, 5023 (2001)

[111] M.B. Tsang *et al.*, Phys. Rev. **C64**, 041603 (2001)

[112] M.B. Tsang *et al.*, Phys. Rev. **C64**, 054615 (2001)

[113] E.A. Uehling and G.E. Uhlenbeck, Phys. Rev. **43**, 552 (1933)

[114] A.M. Vander Molen *et al.*, Users Guide to the MSU 4π Array 3'rd ed. (1996)

[115] V.E. Viola *et al.*, Phys. Rev. **C59**, 2660-2669 (1999)

[116] V.E. Viola, Nucl. Phys. **A734**, 487 (2004)

[117] R. Wada *et al.*, Phys. Rev. **C62**, 034601 (2000)

[118] A. Wagner *et al.*, Nucl. Inst. Meth. **A456**, 290 (2001)

[119] V.F. Weisskopf, Phys. Rev. **52**, 295 (1937)

[120] G.D. Westfall *et al.*, Phys. Rev. Lett. **37**, 1202 (1977)

[121] C.F. Williams, Ph.D. Thesis (Michigan State University, 1996)

[122] H.Xi *et al.*, Phys. Rev. **C67**, R462 (1998)

[123] H.S. Xu *et al.*, Phys. Rev. Lett. **85**, 716 (2000)

[124] H.M. Xu *et al.*, Phys. Rev. **C40**, 186 (1989)

[125] S.J. Yennello *et al.*, Phys. Lett. **B321**, 15 (1994)